

Oxidation Behavior of
Zirconium Diboride Silicon Carbide Based Materials
at Ultra-High Temperatures

A Dissertation
Presented to
the faculty of the School of Engineering and Applied Science
University of Virginia

in partial fulfillment
of the requirements for the degree

Doctor of Philosophy
by

Kathleen N. Shugart

May
2014

APPROVAL SHEET

The dissertation
is submitted in partial fulfillment of the requirements
for the degree of
Doctor of Philosophy

Kathleen N. Shugart

AUTHOR

The dissertation has been read and approved by the examining committee:

Elizabeth Opila

Advisor

William Johnson

Chair

Robert Kelly

Matthew Neurock

Triplicane Parthasarathy

Accepted for the School of Engineering and Applied Science:

James H. Ayres

Dean, School of Engineering and Applied Science

May
2014

Abstract

ZrB₂-SiC is of high interest for Thermal Protection Systems (TPS) for future hypersonic vehicles. Both ZrB₂ and its oxidation product, ZrO₂, possess high melting temperatures ($T_m=3245^{\circ}\text{C}$ and 2715°C respectively) needed for this application. SiC is added to improve the oxidation resistance. However, the oxidation resistance of ZrB₂-SiC at ultra-high temperatures is poor and the oxidation mechanisms are not well understood. The aim of this work was to perform a quantitative study of the oxidation behavior in order to improve life prediction.

The oxidation behavior of ZrB₂-30 vol% SiC was studied using two oxidation procedures. A box furnace was used to oxidize specimens for times between 30 seconds and 100 hours at temperatures of 1300°C - 1550°C in stagnant air. For ultra-high temperature testing, a resistive heating system was designed and built, which allowed oxidation at temperatures of 1300°C - 1800°C for times between 5 and 70 minutes in controlled oxygen atmospheres. Oxidation was quantified by measuring mass change and oxidation product layer thicknesses. A combination of scanning electron microscopy, energy dispersive spectroscopy, x-ray diffraction, x-ray photoelectron spectroscopy, inductively coupled plasma optical emission spectrometry, and time of flight secondary ion mass spectrometry was used to characterize the oxidation products.

Two oxidation regimes were identified; 1) low temperature oxidation below 1627°C and 2) high temperature oxidation at and above 1627°C . Low temperature oxidation exhibited a two-layer oxide, which consisted of a borosilicate glass layer above a ZrO₂+C layer. Key findings indicate that oxygen transport in both zirconia and borosilicate glass must be considered in modeling the low temperature oxidation behavior of ZrB₂-30 vol% SiC. In addition composition and thickness variations of the borosilicate glass layer must also be considered.

The transition between the low and high temperature oxidation regimes is attributed to a change in the thermodynamically favored oxidation products, considering a locally SiC-rich microstructure. High temperature oxidation, $T \geq 1627^{\circ}\text{C}$, resulted in formation of three oxidation product layers. A borosilicate glass layer was found above a layer with ZrO_2 and borosilicate glass. Beneath these was a porous layer of ZrB_2 resulting from SiC depletion due to active oxidation to $\text{SiO}(\text{g})$. Key findings indicate that the oxidation rate is much more rapid in this oxidation regime, that the SiC depletion layer growth is best explained by parabolic gas phase diffusion in the porous layer, and again, oxygen transport in both zirconia and borosilicate glass must be considered in modeling the high temperature oxidation behavior of ZrB_2 -30 vol% SiC.

This work provided a quantitative analysis of the oxidation kinetics of ZrB_2 -30 vol% SiC. The thermodynamic and kinetic analyses of the two distinct oxidation regimes of ZrB_2 -30 vol% SiC enable improved life prediction.

Acknowledgements

Completing this thesis was only possible with the help and support of many people. The first thank you must go to Dr. Elizabeth Opila for her guidance and support during this research. She was always enthusiastic, easy to approach, and happy to assist. A number of undergraduate lab assistants contributed their time and thoughts to this study, so thank you as well to Siying Liu, Forrest Craven, Brandon Patterson, and David Lichtman. Fellow graduate students in Dr. Opila's research group, Joseph Hagan, Junchong Shen, Bohuslava McFarland, Robert Golden, Megan Wilson, and Crescent Islam, also assisted, whether it be lending an extra set of eyes to a resistive heating experiment or as a source of information. I would like to acknowledge the invaluable assistance of Barry Baber and Peter Schare in the design and construction of the resistive heating system. In addition, much of the characterization work would not have been possible without Richard White and the Nanoscale Materials Characterization Facility at the University of Virginia.

I would also like to acknowledge the National Hypersonic Research Center for initial funding for this work and Eric Neuman and Dr. William Fahrenholtz at Missouri University of Science and Technology who provided all of the ZrB₂-30 vol% SiC material. Dr. Wayne Jennings and Annette Marsolais at Case Western Reserve University were essential for their help with the XPS and ToF-SIMS characterization. Dr. Arthur Heuer at Case Western Reserve University made extensive use of the ToF-SIMS possible. Dr. David Marshall at Teledyne Scientific assisted in sectioning specimens for ToF-SIMS. I am also grateful for helpful discussions and advice from the Committee and professors at the University of Virginia, especially Dr. William Johnson, Dr. Triplicane Parthasarathy, and Dr. Petra Reinke.

Finally, thank you to the many friends and family who supported me and kept me sane.

Table of Contents

APPROVAL SHEET	ii
Abstract	iii
Acknowledgements	v
Table of Contents	vi
List of Figures	ix
List of Tables	xv
Chapter 1: Introduction	1
UHTCs and Their Applications.....	1
Oxidation Behavior of ZrB ₂ -based Materials.....	2
Chapter 2: Background	7
Variability of Oxidation Behavior	7
Oxide Morphology	8
Oxygen Diffusion Mechanism	9
Objectives.....	13
Chapter 3. Experimental Procedure	14
Specimen Preparation.....	14
Box Furnace Oxidation	15
Resistive Heating.....	17
Comparison of Box Furnace and Resistive Heating System	21
Double Oxidation	23
Characterization	25
Thermodynamic Calculations	28
Chapter 4 Task 1- Variability of Oxidation Kinetics.....	29
Objective	29
Results	29
<i>Oxidation Kinetics</i>	29
<i>Initial Stage Oxidation</i>	35
<i>Initial Oxide Composition</i>	41
<i>Viscous Flow of the Outer Oxide Layer</i>	43
<i>Initial Surface Roughness</i>	44

<i>Glass Pools and Bubble Formation</i>	47
Discussion	48
<i>Variability of Oxidation Kinetics</i>	48
<i>Initial Stage Oxidation</i>	50
<i>Viscous Flow of the Outer Oxide Layer</i>	51
<i>Initial Surface Roughness</i>	52
<i>Humidity</i>	52
<i>Glass Pools and Bubble Formation</i>	53
<i>Limitations</i>	56
Conclusions	57
Recommendations for Future Work.....	58
Chapter 5 Task 2- Oxide Morphology	59
Objective	59
Results	59
<i>Oxide Growth Kinetics</i>	59
<i>Oxide Morphology Regime I: Temperatures <1627°C</i>	61
<i>Oxide Morphology Regime II: Temperatures ≥1627°C</i>	64
<i>SiC Depletion Growth Kinetics</i>	69
Discussion	72
<i>Temperature Considerations for Resistive Heating Technique</i>	72
<i>Oxide Morphology Regime I: Temperatures <1627°C</i>	72
<i>Transition from C Condensed Oxidation to SiC Depletion</i>	74
<i>Oxide Morphology Regime II: Temperatures ≥1627°C</i>	77
<i>Depletion Kinetics</i>	78
Conclusions	79
Recommendations for Future Work.....	79
Chapter 6 Task 3- Oxygen Diffusion Mechanism	81
Objective	81
Results	81
<i>B₂O₃ Concentration in the Borosilicate Glass Layer</i>	81
<i>¹⁶O₂-¹⁸O₂ Double Oxidation Experiments: ToF-SIMS/EDS/SEM Characterization</i>	91

Discussion	99
<i>B₂O₃ Concentration in Borosilicate Glass</i>	99
<i>Oxygen Diffusion Pathways- Double Oxidation Experiments</i>	102
Conclusions:	107
Recommendations for Future Work:.....	107
Chapter 7 Considerations for Future Modeling and Application of ZrB ₂ -SiC	109
Comparison of Findings to Assumptions in Existing Life Prediction Models	109
Considerations for Future Application.....	110
Chapter 8 Conclusions	112
Appendices:.....	115
Appendix 1: Resistive Heating System.....	115
Obstacles Overcome.....	115
Pyrometry	119
Appendix 2: Resistive Heating Testing Conditions.....	120
Appendix 3: Casino Simulation for B Concentration Determined by Energy Dispersive Spectroscopy (Performed by Siying Liu)	122
Appendix 4: Inductively Couple Plasma Optical Emission Spectrometry (Performed by Forrest Craven, Siying Liu, Bohuslava McFarland)	126
Experimental	126
Example Calculation	128
Appendix 5: Collaborators	130
Appendix 6: Publications	131

List of Figures

Figure 1. Representative morphology of oxide scales on $\text{ZrB}_2\text{-SiC}$ oxidized in air. These were oxidized for 100 minutes at a) 1500°C and b) 1627°C . (Micrograph b reprinted with permission of Dr. Elizabeth Opila ²⁰ .)	3
Figure 2. $\text{B}_2\text{O}_3\text{-SiO}_2$ phase diagram, from ACerS NIST Phase Equilibria Diagrams, figure 11777. (Reprinted with permission of The American Ceramic Society.)	5
Figure 3. $\text{ZrO}_2\text{-SiO}_2$ phase diagram, from ACerS NIST Phase Equilibria Diagrams, figure Zr-190. (Reprinted with permission of The American Ceramic Society.)	6
Figure 4. Zr-O phase diagram, from ACerS NIST Phase Equilibria Diagrams, figure 11690. (Reprinted with permission of The American Ceramic Society.)	6
Figure 5. $\text{ZrB}_2\text{-30 vol\% SiC}$ specimen a) cut and placed in yttria stabilized zirconia (YSZ) boat for box furnace oxidation exposure. Scale marker is in cm b) Machined into bridge shape for resistive heating with the middle 3.5mm thinned to 0.5mm.	15
Figure 6. $\text{ZrB}_2\text{-30 vol\% SiC}$ specimen in yttria stabilized zirconia (YSZ) boat with YSZ spacer at $\sim 45^\circ$ angle.	16
Figure 7. Resistive heating setup with specimen chamber, pyrometer, and recording computer.	18
Figure 8. Resistive heating chamber with high current feed-throughs (red wires), 16O ₂ and 18O ₂ gas inlets, gas outlet, pump outlet, and low vacuum gauge.	18
Figure 9. Schematic of resistive heating system.	19
Figure 10. $\text{ZrB}_2\text{-30 vol\% SiC}$ bridge specimen prepared for oxidation in resistive heating system and held into system using alligator clips.	20
Figure 11. $\text{ZrB}_2\text{-30 vol\% SiC}$ bridge specimen with Pt wire prepared for temperature calibration test in resistive heating system.	20
Figure 12. Fractured cross sections of $\text{ZrB}_2\text{-30 vol\% SiC}$ oxidized at 1500°C for 20 minutes using a) standard box furnace b) resistive heating system. Both cross sections display the same morphology and similar oxide thicknesses, indicating no artifacts from resistive heating.	22
Figure 13. Fractured cross sections of $\text{ZrB}_2\text{-30 vol\% SiC}$ oxidized using the resistive heating system at 1500°C a) for 20 minutes consecutively b) for 20 minutes in 2 stages (15 minutes and 5 minutes). Both cross sections display the same morphology and similar oxide thicknesses, indicating no artifacts from double oxidation.	23
Figure 14. Specific mass change (mg/cm^2) for $\text{ZrB}_2\text{-30 vol\% SiC}$ oxidized in standard box furnace in ambient air as a function of time and temperature. a) Provides data for all times b) provides data for times under 4 hours for easier differentiation.	30
Figure 15. $\text{ZrB}_2\text{-30 vol\% SiC}$ mass gain after 100 minute exposures in standard box furnace in ambient air showing large variation in material behavior, even when specimens are cut from the same initial bar. Bar X indicates that no specific bar was identified.	31
Figure 16. Mounted and polished cross section of $\text{ZrB}_2\text{-30 vol\% SiC}$ exposed for 100 minutes in standard box furnace in ambient air at a) 1400°C b) 1500°C showing variation in layer thicknesses and scalloped penetration depths of oxidation.	32

Figure 17. Dependence of ZrO_2 thickness on borosilicate thickness for a single specimen oxidized 100 minutes at 1500°C in standard box furnace in ambient air. Oxidation resistance provided by borosilicate glass is apparent. Star indicates maximum oxidation depth, used in maximum mass gain prediction.	32
Figure 18. Specific mass change (mg/cm^2) for ZrB_2 -30 vol% SiC oxidized at 1500°C in ambient air, compared to both average k_p and the 95% confidence interval on k_p , calculated from results up to 4 hours. Insert corresponds to the boxed region. Star indicates maximum mass gain predicted using maximum oxidation depth. (See Figure 17.) Long term oxidation (24 and 100 hour tests) are much higher than calculated k_p or 95% confidence interval.	34
Figure 19. ZrB_2 -30 vol% SiC (as-received surface) after 10 second exposure at 1500°C in ambient air in standard box furnace showing the beginning of the oxide coverage of SiC by borosilicate glass and the oxidation of ZrB_2 to nano-scale ZrO_2	36
Figure 20. ZrB_2 grain in as-received ZrB_2 -30 vol% SiC (as-received surface) oxidized to ZrO_2 grains ($\sim 80\text{nm}$ grain size) after 10 second exposure at 1500°C in ambient air in standard box furnace.	36
Figure 21. ZrB_2 -30 vol% SiC (as-received surface) a) prior to oxidation b) after 20 second exposure at 1500°C in ambient air in standard box furnace (circle marks the same feature in both). Borosilicate glass has spread over the SiC grains and some $\text{ZrB}_2/\text{ZrO}_2$ regions. ZrO_2 grains are larger than after 10 second exposure at 1500°C	36
Figure 22. ZrB_2 -30 vol% SiC (as-received surface) after 30 second exposure at 1500°C in ambient air in standard box furnace, a) surface view, b) cross section. Borosilicate glass has spread over entire surface with uneven regions of ZrO_2 exposure.	37
Figure 23. ZrB_2 -30 vol% SiC (as-received surface) after 30 second exposure at 1500°C in ambient air in standard box furnace showing a) a borosilicate glass pool, b) bubbles on the surface, highlighted with white, and c) the ZrO_2 grains within a burst bubble.	38
Figure 24. XRD Pattern of as-received ZrB_2 -30 vol% SiC and after 10 seconds and 10 minutes at 1500°C in ambient air in standard box furnace showing the oxidation of ZrB_2 to ZrO_2 as a function of time. Note as oxidation time increased, the decrease of the major ZrB_2 peak at $2\theta = 41^\circ$ and the increase of the major ZrO_2 peak at $2\theta = 28^\circ$	40
Figure 25. ZrB_2 -30vol%SiC a)prior to oxidation, showing cut mark on bottom left b) after 1 minute exposure, with cut mark still visible though partly filled on bottom left (circle marks the same feature in both.) Borosilicate glass has covered the surface and most of the ZrO_2 grains. The exposed ZrO_2 is unevenly distributed.	40
Figure 26 ZrB_2 -30vol%SiC after 10 minute exposure at 1500°C a) at 10,000X b) at 150X. The borosilicate glass has covered the entire surface. Only a few, large regions of ZrO_2 are seen, as in a).	41
Figure 27. XPS results for as-received ZrB_2 -30 vol% SiC oxidized in stagnant air at 1500°C for times of 10 and 20 seconds using standard box furnace. Zr-O, Si-O, and B-O bonds are seen, indicating ZrO_2 and borosilicate glass on the surface.	42

Figure 28. Oxide thickness versus position for a ZrB ₂ -30 vol% SiC specimen oxidized at ~45° angle for 100 minutes at 1500°C in ambient air in standard box furnace, showing no evidence of glass flow.	44
Figure 29. ZrB ₂ -30 vol% SiC with 0.05µm surface finish after 10 second exposure at 1500°C in ambient air in standard box furnace, showing the distribution of the borosilicate glass over the surface a) at intermediate magnification b) at high magnification.	45
Figure 30. ZrB ₂ -30 vol% SiC with a 0.05µm polished surface finish after 20 second exposure at 1500°C in ambient air in standard box furnace showing the distribution of the borosilicate glass over the surface a) at intermediate magnification b) at high magnification.	46
Figure 31. ZrB ₂ -30 vol% SiC oxidized for 20 seconds at 1500°C in ambient air in standard box furnace using a) as-received material and b) material with a 0.05µm surface finish. Both show uneven distribution of the borosilicate glass over the surface, though the spacing is different. ..	46
Figure 32. ZrB ₂ -30 vol% SiC oxide morphology after oxidation at 1500°C for a) 24 hours b) 100 hours, showing similar morphology to samples oxidized for >4 hours, with both ZrO ₂ scallops and bubbles in the borosilicate present.	50
Figure 33. Proposed mechanism for ZrB ₂ -30 vol% SiC oxidation variability due to the formation and bursting of bubbles in the borosilicate glass.	55
Figure 34. Log(k _p) vs 1/T for ZrO ₂ layer growth showing clear change in activation energy between oxidation regimes. This is explained by increased CO(g) production at temperatures ≥1627°C.	60
Figure 35. Standard morphology of oxide scales on ZrB ₂ -SiC oxidized at temperatures a) below 1627°C, showing two layers of oxidation products b) above 1627°C, showing three layers of oxidation products.	62
Figure 36. EDS indicating the presence of both C and SiC particles in the ZrO ₂ layer of a ZrB ₂ -30 vol% SiC fracture section after oxidation at 1500°C for 20 minutes in flowing O ₂ using resistive heating. Scale marker indicates 5µm.	63
Figure 37. SE image and EDS maps of ZrB ₂ -30 vol% SiC fracture section after oxidation at 1600°C for 55 minutes in flowing O ₂ using resistive heating. C between ZrO ₂ grains is clear. Scale markers indicate 10µm.	64
Figure 38. SE image and EDS maps of ZrB ₂ -30 vol% SiC fracture section after oxidation at 1650°C for 50 minutes in flowing O ₂ using resistive heating. SiC depletion under ZrO ₂ and borosilicate layers is clear. Scale marker indicates 50µm.	65
Figure 39. SE image and EDS maps of ZrB ₂ -30 vol% SiC fracture section after oxidation at 1650°C for 50 minutes in flowing O ₂ using resistive heating showing borosilicate glass beneath the ZrO ₂ /ZrB ₂ interface. Scale marker indicates 10µm.	66
Figure 40. Oxidation conditions for SiC depletion in ZrB ₂ -30 vol% SiC. All exposures T≤1550°C were conducted in stagnant air. All exposures T>1550°C were conducted in 900sccm flowing O ₂	66
Figure 41. Fracture section of ZrB ₂ -30 vol% SiC oxidized at 1650°C for 45 minutes in flowing O ₂ using resistive heating system showing partially removed SiC grains (arrows) surrounded by	

ZrB ₂ grains, in the SiC depletion layer (base material is below the imaged region.) This indicates SiC depletion forms due to active oxidation of SiC to SiO(g) and CO(g). Scale marker indicates 4μm.	67
Figure 42. SE image and EDS maps of ZrB ₂ -30 vol% SiC fracture section after oxidation at 1650°C for 10 minutes in flowing O ₂ using resistive heating. C is seen between ZrO ₂ grains and SiC depletion has not begun. This indicates a time dependence to the transition between oxidation regimes. Scale marker indicates 10μm.	68
Figure 43. High magnification SE image and EDS maps of ZrB ₂ -30 vol% SiC fracture section after oxidation at 1650°C for 20 minutes in flowing O ₂ using resistive heating. Squares mark pores left by SiC depletion. Circles mark C remaining after oxidation of Si. Red dotted line marks boundary between ZrO ₂ and ZrB ₂ . This supports a time and microstructural dependence to the transition between oxidation regimes. Scale marker indicates 5μm.	68
Figure 44. ZrB ₂ -30 vol% SiC oxidized at 1800°C for a series of times (5-20 minutes), showing growth of the SiC depletion layer. The bracket highlights the porous layer. 5 minutes has 43±10μm, 15 minutes has 74±6μm, and 20 minutes has 104±8μm of SiC depletion. Scale maker indicates 50μm.	70
Figure 45. SiC depletion depth versus time in minutes for oxidized ZrB ₂ -30 vol% SiC.	71
Figure 46. Log(k) versus 1/T for both linear and parabolic growth of the SiC depletion layer in oxidized ZrB ₂ -30 vol% SiC. k _l is μm/min and k _p is μm/min ^{1/2} . No temperature dependence is evident, indicating gas phase diffusion is rate limiting for growth of the SiC depletion layer. ...	71
Figure 47. Ellingham diagram, plotted using FactSage, showing reactions of ZrB ₂ -SiC with 1 mole of O ₂ . This diagram explains the transition between oxidation regimes.	76
Figure 48. Fracture section of ZrB ₂ -30 vol% SiC oxidized in flowing O ₂ using resistive heating system at a)1600°C for 55 minutes b) 1650°C for 50 minutes, showing increased bubbling and ZrO ₂ in b).	77
Figure 49. Diagram illustrating disassociation of SiO ₂ to SiO(g) and O ₂ (g), which provides a source of O ₂ (g) for continued growth of the SiC depletion layer, limited by gas phase diffusion.	78
Figure 50. SEM/EDS results for ZrB ₂ -30 vol% SiC oxidized at 1500°C for 100 minutes in stagnant air after two DI H ₂ O soaks and dissolution in a) 3ml of HF solution at 35°C for 24 hours b) 3ml of HF solution diluted with 12mL of DI H ₂ O at 35°C for 24 hours, showing the area with the most products left behind after dissolution.	82
Figure 51. Total mass of generated oxides versus temperature for ZrB ₂ -30 vol% SiC specimens oxidized to generate the same oxide thickness. 1300°C specimens oxidized for 221 minutes, 1400°C specimens oxidized for 128 minutes, and 1500°C specimens oxidized for 100 minutes. Similar mass gain indicates correct choice of oxidation times for generating the same quantity of oxide products.	86
Figure 52. Total mass of generated oxides versus temperature for ZrB ₂ -30 vol% SiC specimens oxidized for 221 minutes, showing an increase in oxide formation with increasing temperature.	87

Figure 53. XPS results for ZrB ₂ -30 vol% SiC oxidized at 1500°C for 10 (open symbols) and 100 (closed symbols) minutes in stagnant air. Both conditions showed lower B content at the surface then inside the borosilicate scale. 100 minutes of oxidation showed decreased quantities of B with a corresponding increase in Si compared to oxidation for 10 minutes.	88
Figure 54. XPS and EDS results showing increased B deeper into the borosilicate glass for a specimen oxidized at 1500°C for 100 minutes in stagnant air, showing the first 5µm of the scale. Dotted line indicates B concentration using B diffusion coefficient from best fit to EDS results. Dashed line indicates B concentration using B diffusion coefficient from best fit to XPS results. Solid line indicates B concentration using calculated B diffusion coefficient from ICP-OES results.	89
Figure 55. SEM/ToF-SIMS results for ZrB ₂ -30 vol% SiC oxidized at 1500°C for 10 minutes in ¹⁶ O ₂ and 9 minutes in ¹⁸ O ₂ . ¹⁸ O ₂ is found throughout both the borosilicate glass and the ZrO ₂ +C layer.....	92
Figure 56. Line scan of ¹⁸ O through oxide formed on ZrB ₂ -30 vol% SiC exposed at 1500°C for 10 minutes in ¹⁶ O ₂ and 9 minutes in ¹⁸ O ₂ . Dashed lines mark approximate location of interfaces.	92
Figure 57. SEM/ToF-SIMS/EDS results for ZrB ₂ -30 vol% SiC oxidized at 1500°C for 10 minutes in ¹⁶ O ₂ and 9 minutes in ¹⁸ O ₂ , showing ¹⁸ O throughout the ZrO ₂ grains even at the ZrO ₂ /ZrB ₂ interface. Scale bar indicates 10µm.	93
Figure 58. ToF-SIMS/SEM results for ZrB ₂ -30 vol% SiC oxidized at 1650°C for 29 minutes in ¹⁶ O ₂ and 45 seconds in ¹⁸ O ₂ . ¹⁸ O ₂ has exchanged with ¹⁶ O ₂ in initial borosilicate scale, and permeated through the borosilicate glass and formed new Si ¹⁸ O ₂ at the borosilicate glass/SiC depletion layer interface. Scale bar indicates 100µm.	95
Figure 59. High magnification of ZrB ₂ -30 vol% SiC oxidized at 1650°C for 29 minutes in ¹⁶ O ₂ and 45 seconds in ¹⁸ O ₂ , showing ¹⁸ O in SiO ₂ at the no depletion/SiC depletion interface. Scale bar indicates 10µm.	96
Figure 60. SEM/ToF-SIMS results for ZrB ₂ -30 vol% SiC oxidized at 1650°C for 45 minutes in ¹⁶ O ₂ and 5 minutes in ¹⁸ O ₂ . ¹⁸ O ₂ was found throughout the borosilicate glass and ZrO ₂ grains. Scale bar indicates 100µm.	97
Figure 61. SEM/EDS/ToF-SIMS results for ZrB ₂ -30 vol% SiC oxidized at 1650°C for 45 minutes in ¹⁶ O ₂ and 5 minutes in ¹⁸ O ₂ . The circle marks an area in ¹⁸ O map showing less ¹⁸ O in in borosilicate glass. Scale bar indicates 20µm.	98
Figure 62. Approximate B ₂ O ₃ concentration (mol%) throughout borosilicate glass scale formed during oxidation of ZrB ₂ -30 vol% SiC. (Values given are for specimen oxidized at 1500°C for 100 minutes in stagnant air, using average B concentration (ICP-OES) to determine the average diffusion coefficient.) A majority of the borosilicate glass is shown to have sufficient B ₂ O ₃ concentration to be liquid at the oxidation temperature.....	101
Figure 63. Cross-sectional view of ZrB ₂ -30 vol% SiC oxidized at 1500°C for 100 minutes in stagnant air with a nearly uniform oxidation front between ZrB ₂ /SiC and the oxides.	101

Figure 64. Schematic of $^{18}\text{O}_2$ diffusion through the borosilicate glass to form new SiO_2 at the $\text{ZrO}_2/\text{ZrB}_2$ interface.....	104
Figure 65. SEM/ToF-SIMS results for ZrB_2 -30 vol% SiC oxidized at 1650°C for 45 minutes in $^{16}\text{O}_2$ and 5 minutes in $^{18}\text{O}_2$, showing change of ^{18}O contrast from brighter in ZrO_2 near surface to brighter in borosilicate near $\text{ZrO}_2/\text{ZrB}_2$ interface. The total ion count is included to show lack of microstructural influence.	106
Figure 66 a) Initial specimen holder using copper blocks with insets. b) Flat copper specimen holder with silver foil clamps. c) Flat copper specimen holder with Maycor clamps.	116
Figure 67. Final holding arrangement for ZrB_2 -30 vol% SiC bridge specimen in resistive heating system. Cu wire feeds the current into the system, Pt foil prevents reaction of copper wire with hot specimen, ZrO_2 supports prevents specimen snapping upon insertion due to torque. Specimen is held in place using alligator clips.	116
Figure 68. Plot of emissivity and temperature versus current for ZrB_2 -30 vol% SiC specimen oxidized at 1300°C for 10 minutes a) at full scale b) showing the scatter in the temperature and emissivity measurements.	121
Figure 69. Casino simulation showing sampling volume in borosilicate glass formed on ZrB_2 -30 vol% SiC after oxidation at 1500°C for 100 minutes in stagnant air in standard box furnace for an accelerating voltage of 5kV.	123
Figure 70. Casino simulation showing sampling volume in borosilicate glass formed on ZrB_2 -30 vol% SiC after oxidation at 1500°C for 100 minutes in stagnant air in standard box furnace for an accelerating voltage of 10kV.	124
Figure 71. Casino simulation showing sampling volume in borosilicate glass formed on ZrB_2 -30 vol% SiC after oxidation at 1500°C for 100 minutes in stagnant air in standard box furnace for an accelerating voltage of 20kV.	124
Figure 72. Casino simulation of depth versus normalized hits generated for 5kV in the simulated borosilicate glass.	125

List of Tables

Table 1 Possible Oxygen Diffusion Pathways/Mechanisms during oxidation of ZrB ₂ -SiC.	12
Table 2. Conditions for Double Oxidation Experiments of ZrB ₂ -30 vol% SiC. * indicates sectioned specimen was successful for ToF-SIMS. † ZrO ₂ growth is calculated using experimental k _p values.	24
Table 3. Thickness of oxide layers formed on ZrB ₂ -30 vol% SiC after oxidation in standard box furnace in ambient air for 100 minutes as a function of temperature. Large standard deviations are seen for all oxide thicknesses.	31
Table 4. Comparison of literature and experimental results for oxidation of ZrB ₂ -SiC in standard box furnace in air. k _p s calculated for this work are of the same order of magnitude as the literature.	33
Table 5. ZrO ₂ and borosilicate glass distributions after short-term oxidation of ZrB ₂ -30 vol% SiC (as-received surface) in ambient air at 1500°C in standard box furnace.	35
Table 6. Mass gain due to oxidation of ZrB ₂ -30 vol% SiC in ambient air at 1500°C in standard box furnace. As-received and polished surfaces prior to oxidation show average mass gains within a standard deviation of each other.	39
Table 7. XPS energy assignments for spectra shown in Figure 27. (?) indicates uncertainty in identification.	42
Table 8. Observations of bubbles in the borosilicate glass phase formed during oxidation of ZrB ₂ -30 vol% SiC in ambient air in standard box furnace.	47
Table 9. Experimental results for oxidation kinetics of ZrB ₂ -30 vol% SiC. Note the large R ² values due to scatter in the data.	60
Table 10. Balanced reactions for transition in ZrB ₂ -SiC oxidation behavior.	76
Table 11. Mass change data for ZrB ₂ -30 vol% SiC oxidized under stagnant air in a standard box furnace after oxidation and after H ₂ O soak (leaching).	83
Table 12. Summary of B retained in the borosilicate scale after oxidation of ZrB ₂ -30 vol% SiC under stagnant air conditions. A high percentage of the B does not volatilize under the conditions tested, leading to a high B ₂ O ₃ concentration in the borosilicate glass.	85
Table 13. Concentration results from EDS performed at varying accelerating voltages, showing increased B concentration deeper in the borosilicate scale.	89
Table 14. Resistive heating test conditions.	121
Table 15 Layer information used in Casino simulations for EDS penetration depth determinations of borosilicate glass formation on ZrB ₂ -30 vol% SiC after oxidation at 1500°C for 100 minutes in stagnant air in standard box furnace.	123

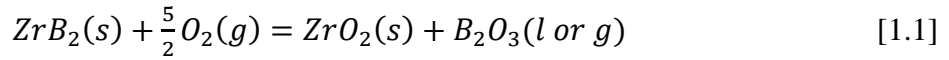
Chapter 1: Introduction

UHTCs and Their Applications

Ultra-High Temperature Ceramics (UHTCs) are a family of materials that have melting temperatures in excess of 3000°C, making them attractive for aerospace applications such as Thermal Protection Systems (TPS) on hypersonic flight vehicles. Design of future hypersonic vehicles will incorporate sharper wing leading edges and nose cones, allowing for better maneuverability and higher speeds^{1,2}. When the radius of the wing tip is made sharper and the speed is increased the temperatures seen by the space craft will increase to 1700°-3000°C due to the shockwaves' closer proximity to the vehicle surface²⁻⁴. This temperature range is beyond the operating capability of current TPS, necessitating the development of new TPS materials³⁻⁷. One of the largest concerns for non-oxide TPS materials is oxidation behavior at ultra-high temperatures. Current materials, including SiC-coated carbon-carbon composites, do not have sufficient oxidation resistance at these ultra-high temperatures due to formation of liquid (SiO_2 $T_m=1723^\circ\text{C}$) and gaseous (SiO(g)) products⁴. UHTCs, on the other hand, form solid oxides which themselves have very high melting temperatures. One member of this family, ZrB_2 , has been extensively studied since the 1960s due to its high melting temperature ($T_m=3245^\circ\text{C}$), relatively low theoretical density (6.09g/cm^3), strength retention at high temperatures, chemical stability, resistance to erosion/corrosion, and the formation of ZrO_2 ($T_m=2715^\circ\text{C}$)^{3,4,7-9}. However, the oxidation rate of ZrB_2 and ZrB_2 -based materials is rapid and unacceptable for reusable applications. In addition, there are still many unanswered questions concerning the oxidation mechanism. This work develops a more quantitative understanding of the oxidation mechanism to enable better life prediction and identify methodology for improvements in oxidation behavior.

Oxidation Behavior of ZrB₂-based Materials

When pure ZrB₂ is exposed to temperatures of 900°-1200°C, a two-layer oxide is formed of ZrO₂ grains covered and filled in by a B₂O₃ glassy layer⁹⁻¹¹. The oxidation occurs via the following reaction:



The B₂O₃ glass forms a protective layer and parabolic oxidation kinetics are exhibited¹¹. Above 1300°C, the B₂O₃ volatilizes (Reaction 1.2), leaving a porous and non-protective ZrO₂ layer, made up of columnar grains.

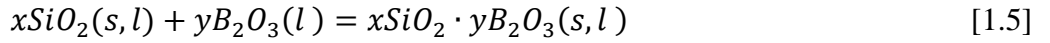
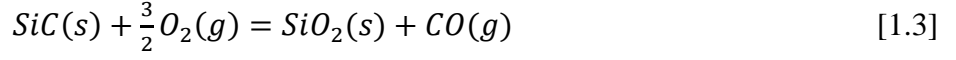


Mass gain kinetics become linear¹¹⁻¹⁴.

In order to improve the oxidation resistance of ZrB₂, a number of additives have been tested, including Al+B, Zr+Si, TaSi₂ and SiC^{5, 10, 15, 16}. Of these, SiC was found to provide the greatest enhancement to the oxidation resistance under almost all conditions due to the formation of a borosilicate layer^{7, 10, 14, 17}. According to Fahrenholtz et al., the addition of 30 vol% SiC provided the optimum oxidation resistance¹⁸. However, when balancing both oxidation resistance and mechanical properties, an addition of 20 vol% SiC has been found by researchers to be the best composition^{8, 10}.

The improvement in oxidation behavior from SiC addition begins at temperatures between 1200°C and 1300°C^{6, 13, 19}. Below these temperatures, preferential oxidation of the ZrB₂ occurs^{11, 20}, while above these temperatures the SiC grains begin to oxidize and form a SiO₂-rich borosilicate phase, which is an amorphous solid upon cooling to room temperature^{12, 13, 19}. The borosilicate glass layer provides the oxidation protection, slowing oxygen diffusion and vaporization of B₂O₃^{12, 19, 21-23}. Parabolic mass gain kinetics are observed for this material, as the

oxygen diffuses through the borosilicate glass and/or ZrO_2 and reacts with the base ZrB_2 -SiC material^{13, 24}. The reactions describing the oxidation include Reactions [1.1] and [1.2], as well as:



The micrographs in Figure 1 are representative of the morphology of ZrB_2 -SiC after it has been oxidized. The protective borosilicate glass layer forms the top of the oxide scale. Beneath the borosilicate glass are ZrO_2 grains. The literature assumes that borosilicate glass fills in the regions between the ZrO_2 grains^{25, 26}.

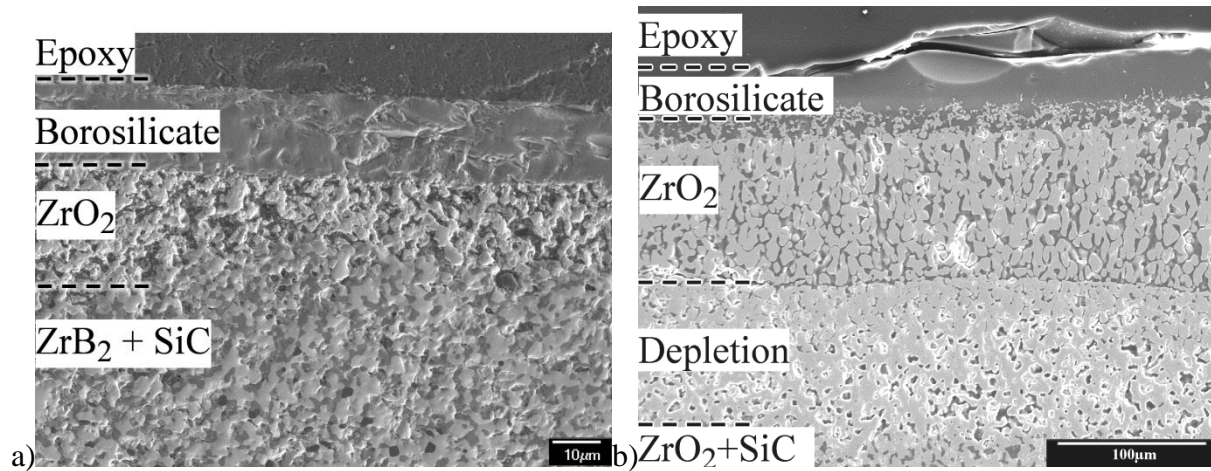
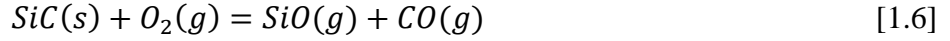


Figure 1. Representative morphology of oxide scales on ZrB_2 -SiC oxidized in air. These were oxidized for 100 minutes at a) 1500°C and b) 1627°C. (Micrograph b reprinted with permission of Dr. Elizabeth Opila²⁰.)

There is indication in some studies of a SiC depletion layer between the unreacted material and the ZrO₂/borosilicate glass layer, as seen in Figure 1b, which occurs by Reaction [1.6].



This reaction will be discussed in detail later. It is important to note that the oxidation of the two phase ZrB₂-SiC mixture offers additional protection to both phases relative to oxidation of the phases individually^{19, 22}. The improvement relative to ZrB₂ has been explained by the more sluggish oxygen diffusion through the SiO₂-rich layer than through B₂O₃, while the improvement over pure SiC at temperatures above the melting point of SiO₂ is explained by the “solid pillars, liquid roof” scale architecture described by Li et al.^{5, 22, 27-29}. The crystalline ZrO₂ provides a skeleton to act as mechanical support for the borosilicate glass, which adheres strongly to the skeleton by capillary forces.

When one mole of SiC oxidizes to SiO₂, there is a volume increase of 118%. ZrB₂ undergoes an increase of 17% when forming ZrO₂. This large volume change due to SiC oxidation and the presence of restricting ZrO₂ columns is believed to cause the SiO₂ to be transported to the top of the oxide forming the protective outside layer, as well as filling in the spaces between the ZrO₂ grains. Due to the presence of B₂O₃ dissolved in the SiO₂, the borosilicate glass will have a much lower melting temperature than pure SiO₂. The impact of B₂O₃ on the melting temperature of SiO₂ can be seen in Figure 2. B₂O₃ also increases O₂ diffusion through SiO₂ on Si substrates³⁰. By adding as little as 1-3 mol% of B₂O₃, the apparent oxygen diffusion coefficient increased by 2-3 orders of magnitude.

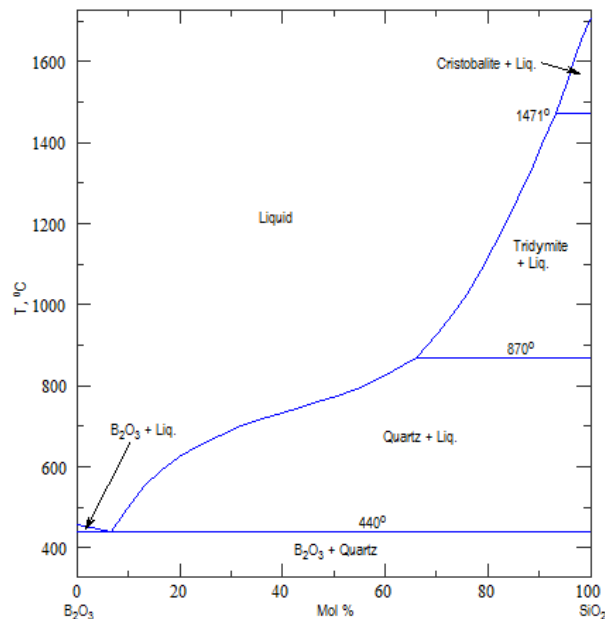


Figure 2. B₂O₃-SiO₂ phase diagram, from ACerS NIST Phase Equilibria Diagrams, figure 11777. (Reprinted with permission of The American Ceramic Society.)

The ZrO₂ skeleton supports against bubble breakouts and external shear flow²². Some bubbles still form in the borosilicate glass and burst, as CO(g) is formed at the reaction interface at significant pressures by Reactions 1.3 or 1.6 and move to escape the material. It has been suggested by several researchers that this gas causes the ZrO₂ to exhibit a columnar oriented structure in the oxide^{23, 28}.

According to the phase diagram of ZrO₂ and SiO₂ (Figure 3), at temperatures below ~1550°C, there is a possible stable phase of ZrSiO₄, however, this has not been commonly seen in any previous oxidation work, and the oxides here will be considered to be ZrO₂, B₂O₃, SiO₂, SiO(g), and CO(g) only. ZrO₂ has several phases over the temperature range of interest in this work. At room temperature up to 1205°C, it is a monoclinic structure. Above 1205°C, it transforms to tetragonal, and then at ~2370°C it transforms to cubic. The Zr-O phase diagram is shown in Figure 4. While SiO₂ has a number of polymorphs, in the high temperature oxidation of ZrB₂-SiC, SiO₂ is found to be amorphous.

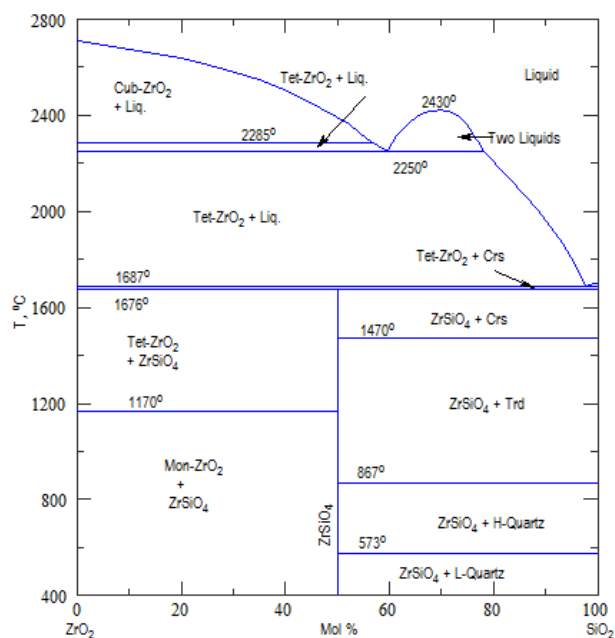


Figure 3. ZrO_2 - SiO_2 phase diagram, from ACerS NIST Phase Equilibria Diagrams, figure Zr-190. (Reprinted with permission of The American Ceramic Society.)

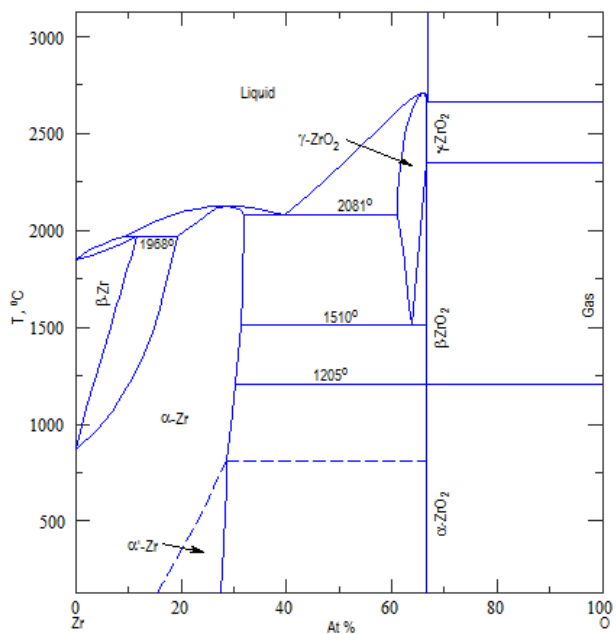


Figure 4. Zr-O phase diagram, from ACerS NIST Phase Equilibria Diagrams, figure 11690. (Reprinted with permission of The American Ceramic Society.)

Chapter 2: Background

Variability of Oxidation Behavior

Most studies of $\text{ZrB}_2\text{-SiC}$ oxidation are screenings of various material compositions. Sufficient data for a statistical analysis of oxidation as a function of time, temperature and material composition are not available. It has also been noted by some authors that while a general behavior is common for certain time/temperature conditions, quantitative agreement between studies for even nominally pure diborides is not necessarily seen¹¹. It is difficult to compare oxidation results from one study to another due to different and often unspecified parameters. Parameters that are often not reported include the atmosphere under which the material is tested, gas flow rate, specimen texturing, and humidity. Some experiments are conducted isothermally while others ramp up to the desired temperature^{23, 24, 31}. Additionally, a number of different testing apparatuses are used, which can impact the results. These include box furnaces, oxyacetylene torches, arc-jet facilities, and resistive heating^{29, 31-33}. Finally, results are reported using different conventions, such as weight gain, scale thickness, or recession as functions of time and temperature¹¹.

While several models for UHTC oxidation kinetics based on results found in the literature exist, the wide range of results makes accurate modeling difficult^{5, 22, 26}. The model by Parthasarathy et al. suggests the quantitative differences from different tests could be due to small changes in porosity or trace impurities in the specimens, both of which are often unreported^{11, 34}. Levine et al. suggest that variation in mechanical properties may be due to issues in repeatable processing, and this could also lead to differences in oxidation behavior²⁴. Other sources of variability in oxidation kinetics may include poor experimental or manufacturing technique, differences in relative humidity during testing, impurities (either

environmental or processing), surface roughness, viscous flow on the macro-scale, or the formation of bubbles in the glass scale. Previous work on ZrB₂-SiC has focused on oxidation times between 10 minute and 2 hours and did not consider the short-term oxidation behavior or its impact^{20, 24, 25, 29, 31, 32, 35}. Gangireddy et al. did observe oxide formation at 1450°-1650°C with *in-situ* optical microscopy, but focused the bulk of their study on bubble formation not oxidation kinetics³⁶.

Oxide Morphology

Prior results indicate that the oxidation of ZrB₂-SiC at 1500°C is passive (Reactions 1.1 and 1.3) and forms a protective layer of borosilicate above ZrO₂, along with CO(g)^{10, 22}. The transition from passive oxidation (Reaction 1.3) to active oxidation (Reaction 1.6) of SiC occurs at high temperatures and low oxygen partial pressures^{4, 6, 13, 20, 23-25, 28, 31, 32, 37}. The oxygen partial pressure at the ZrO₂/ZrB₂ interface is sufficiently low such that at high temperatures the SiC is expected to undergo active oxidation (Reaction 1.6) leading to SiC depletion^{13, 38}. The gases formed at low oxygen partial pressures at the oxide/substrate interface in turn oxidize at the higher oxygen partial pressures found at the oxide surface (Reactions 1.4 and 2.1).



Conditions for formation of the SiC depletion layer, e.g. the transition from passive to active oxidation in the presence of ZrB₂, are not well characterized. It is generally agreed that materials containing 10 vol% or less of SiC do not show a depletion layer and theoretically are not expected to, due to the lack of interconnectivity of the SiC grains^{16, 23, 28}. The SiC grains must be interconnected to provide a path for inward diffusion of the oxygen. When the interior SiC reacts to form SiO(g) and CO(g), pores are left behind through which the O₂(g) diffuses, further depleting the interior of the material. The SiC depletion layer has been reported in ZrB₂-

SiC based materials containing more than 10 vol% SiC when they are oxidized at temperatures as low as 1400°C^{13, 25}, greater than 1600°C²³, only lower than 1900°C²⁰, or not at all^{29, 32}. In addition, the thermodynamics and kinetics for the depletion reaction are poorly understood. A thermodynamic model has been proposed by Fahrenholtz to elucidate the SiC depletion behavior¹³, though its prediction of onset temperature is not in agreement with the results in this work. The porous structure formed during SiC depletion could lead to reduced load-bearing capability or reduced thermal conductivity of ZrB₂-SiC for applications at ultra-high temperatures. Therefore understanding conditions necessary for its formation should help in developing this material for future use²³.

Oxygen Diffusion Mechanism

While the specific oxidation rates of ZrB₂ and ZrB₂-SiC have been measured and semi-quantitatively modeled^{9-11, 26, 34, 39-42}, a detailed and quantitative understanding of the presence/concentration of B₂O₃ in the glass layer formed upon oxidation of ZrB₂-SiC is currently lacking due to the low sensitivity of most characterization techniques to light elements^{13, 20}.

Some work has shown the presence of B in the glass phase, including Tripp et al. who used Electron Microprobe Analysis (EMPA) on material oxidized at 1300°C and 1400°C¹⁹. Karlsdottir et al. discuss the flow of B₂O₃ to the surface of the oxide, which they analyzed using EPMA and Cathodoluminescence (CL)^{43, 44}. They also stated that the surface was depleted in B₂O₃ due to its high vapor pressure. The vapor pressure of B₂O₃ at 1500°C is 233Pa while SiO₂ is 3x10⁻⁴Pa^{13, 45}, suggesting selective volatilization of B₂O₃ and enrichment of SiO₂ will occur in the borosilicate layer relative to the amounts predicted by equilibrium. The B₂O₃ volatilization reactions include:





This depletion has been shown at the oxide surface by Rezaie et al. using Secondary Ion Mass Spectrometry (SIMS) ²¹. The diffusion of B through borosilicate glass is dependent on temperature and glass composition. According to Kawagishi et al., the B diffuses through Si sites of the SiO₂ lattice ⁴⁶. Diffusion rates are found to be on the order of 10⁻²⁰ to 10⁻¹⁴ cm²/sec, when studying the temperature range 900°C-1400°C, with low concentrations of B (<15mol%) ⁴⁶⁻⁴⁹. Neither high temperatures, nor high B concentrations, have been studied for B diffusion in borosilicate glass. An understanding of the B₂O₃ content and concentration profile in the borosilicate glass layer is critical to predicting the oxidation rate of ZrB₂-SiC.

Five possible pathways/mechanisms for oxygen diffusion can be envisioned due to the multiple phases and morphologies in the oxide and these are displayed in Table 1 ⁵⁰. It has been theorized by many (including Parthasarathy et al.) that the rate controlling mechanism of the oxidation of ZrB₂-SiC is the inward diffusion of oxygen through the borosilicate glass, while the ZrO₂ grains have negligible contribution, however, this has not been decidedly proven ^{12, 13, 19, 26, 40}. Previous work has shown ¹⁸O₂ tracer diffusion through ¹⁶O oxide layers (double oxidation) to be one way to determine oxygen diffusion pathways ⁵¹⁻⁵⁴. Predictions for the tracer profiles exhibited by each of the pathways/mechanisms are included in Table 1.

Molecular oxygen may permeate through interstitial spaces in the amorphous borosilicate structure. Network exchange, similar to lattice diffusion in crystalline phases may occur, whereby the oxygen jumps from one network site to the next in the borosilicate glass. Deal and Grove show permeation of oxygen in thermally grown oxide on silicon ⁵⁵. Ogbuji and Opila have found that the enthalpy for the oxidation of SiC is essentially the same as that for Si, indicating that the controlling mechanism of oxidation is the same for both materials ⁵⁶. Network diffusion

is shown to be much slower than permeation during oxidation of silica and in silicate glasses, though the difference lessens as temperature increases^{50, 57, 58}. Zheng et al. have found a transition from permeation to exchange to occur above 1200°C for single-crystal SiC^{59, 60}. For vitreous silica, Kalen et al. found that both network and interstitial mechanism were in operation⁶¹. However, few studies have been done at temperatures as high as those studied here, nor on borosilicate glasses.

Much of the diffusion research for ZrO₂ has been conducted on Y or Ca doped ZrO₂ and monoclinic ZrO₂, which is stable at room temperatures, while at high temperatures such as those studied here, tetragonal ZrO₂ is the stable phase^{40, 62}. The addition of such dopants is known to increase oxygen diffusion through vacancy formation⁶³. Evidence of grain boundary diffusion was found by Brossmann et al. for ultrafine grained, undoped monoclinic ZrO₂⁶². In tetragonal ZrO₂, oxygen is believed to diffuse by the vacancy mechanism, due to the predominance of intrinsic oxygen vacancies^{40, 64}. There may also be Knudsen diffusion occurring through pores in the material⁶⁵.

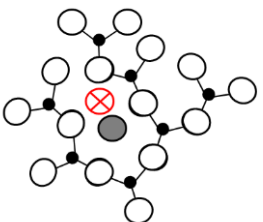
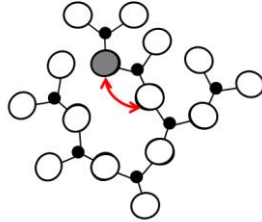
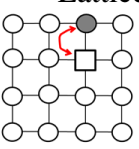
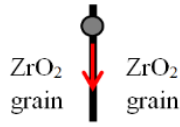
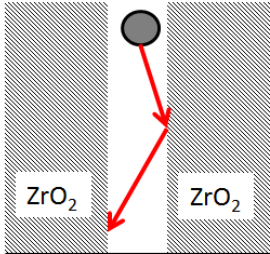
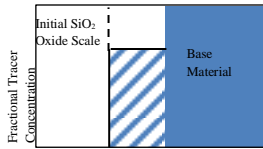
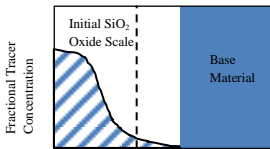
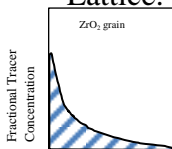
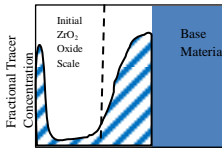
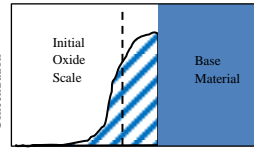
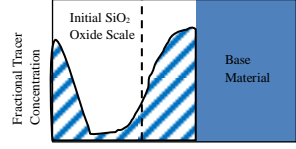
Mechanism	Transport through borosilicate glass		Transport through ZrO_2	Transport through pores
	Permeation	Network Exchange	Lattice or Grain Boundary Diffusion	Knudsen Diffusion
Atomistics of Diffusion	No breaking of bonds. Molecular O_2 is being transported.	Molecular O_2 must dissociate into 2O^- .	Molecular O_2 must dissociate into 2O^- .	Molecular O_2 travels through pores.
	 <p>50</p>	 <p>50</p>	<p>Lattice:</p>  <p>Grain Boundary:</p>  <p>65</p>	
Possible Tracer Concentration Profile			<p>Lattice:</p>  <p>Grain Boundary:</p> 	
	<p>Permeation and Network Together:</p> 			

Table 1 Possible Oxygen Diffusion Pathways/Mechanisms during oxidation of $\text{ZrB}_2\text{-SiC}$.

Objectives

Task 1 of this work includes a statistical analysis of ZrB_2 -30 vol% SiC oxidation under well-defined/controlled conditions at temperatures between 1300°C and 1550°C. Variation of oxidation results are examined in relation to viscous flow and bubble formation in the glass scale. The initial stages of oxidation were explored for the first time to try to understand any relationship to the variable performance in ZrB_2 -SiC oxidation observed at longer times. The effects of surface roughness on short and long term oxidation behavior, which has not previously been reported in the literature, were also examined.

Task 2 provides a detailed look at the constituents and phase distributions in the oxide layers as a function of time and temperature. It provides a thermodynamic explanation of the transition between low and high temperature oxidation regimes. The primary goal was to determine conditions for formation of the SiC depletion layer and to develop a thermodynamic and kinetic description to explain the observed structure.

Task 3 confirms the presence of B_2O_3 in established oxide scales and quantifies its concentration in the glass layer formed during oxidation at temperatures of 1300°C-1500°C. The diffusion pathways of the oxygen are also explored during oxidation of ZrB_2 -30 vol% SiC at temperatures of 1500°C and 1650°C using $^{18}\text{O}_2$ tracer diffusion techniques.

The information gained in these three tasks provides a more detailed understanding of

- 1) Quantitative measurement of oxidation rates of ZrB_2 -30 vol% SiC
- 2) Thermodynamic and kinetic descriptions of oxidation mechanisms of ZrB_2 -30 vol% SiC
- 3) Composition of the borosilicate glass responsible for oxidation resistance

thereby contributing to improved life prediction and development of strategies for improving oxidation resistance of ZrB_2 -SiC.

Chapter 3. Experimental Procedure

Specimen Preparation

ZrB₂-30 vol% SiC specimens were fabricated at Missouri University of Science and Technology using attrition milled powders which were then hot pressed^{25, 66}. WC contamination (~2 wt%) was observed due to the attrition milling, which used WC milling media in polyethylene jars. Specimens were cut from a series of billets using an automated surface grinder into bars of 40mm x 4mm x 3mm and were finished using 1200 grit diamond abrasive. These bars were cut to size (~7mm x 4mm x 3mm) for box furnace testing using a diamond blade. A reference location on the surface was established on a fraction of specimens with a small cut using a diamond blade (Figure 5a.) Two specimen surface preparations were examined: as received (approximate roughness of $0.39 \pm 0.15 \mu\text{m}$) and after polishing to $0.05 \mu\text{m}$ using diamond abrasive (approximate roughness of $0.07 \pm 0.03 \mu\text{m}$.) Surface roughness was measured using a contact profilometer to determine the Ra value using a linear trace (TR200, TIME Group, Inc., Clarksville, TN.) The top surfaces of specimens with marked reference locations were coated with a thin layer of carbon using the Precision Etching and Coating System (PECS) and then characterized using Scanning Electron Microscopy (SEM, JEOL 6700F, Tokyo, Japan) prior to oxidation testing. A portion of the bars were shipped to Bomas Machine Specialties (Sommerville, MA) for machining into “bridge” shaped specimens for oxidation testing. The bridges were 15mm x 3mm x 1.5mm, with the middle 3.5mm thinned to 0.5mm (Figure 5b.)

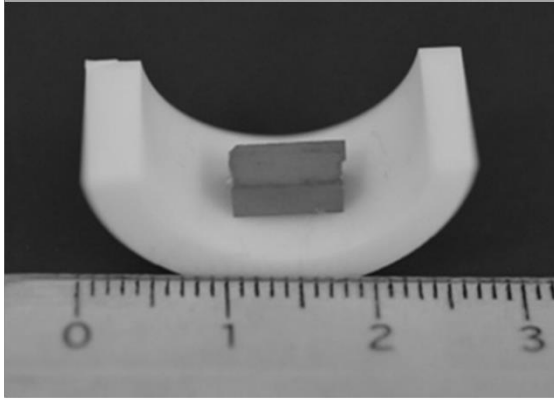
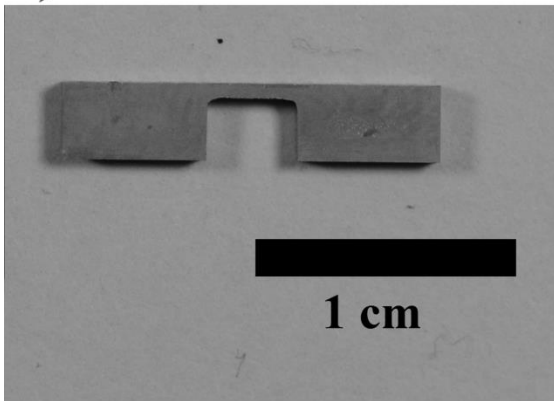


Figure 5. ZrB₂-30 vol% SiC specimen a) cut and placed in yttria stabilized zirconia (YSZ) boat for box furnace oxidation exposure. Scale marker is in cm b) Machined into bridge shape for resistive heating with the middle 3.5mm thinned to 0.5mm.

a)



b)

Box Furnace Oxidation

Prior to box furnace oxidation, all specimens were cleaned using baths of detergent and DI water, DI water, acetone and then ethanol, each for 2 minutes in a sonicator. Dimensions and initial weight of all specimens were recorded. Specimens were individually oxidized and characterized. The

specimens were placed in curved sections of an yttria stabilized zirconia (YSZ, Ortech, Inc., Sacramento, CA) tube while in the furnace, providing line contacts between the specimen and boat, as shown in Figure 5a. This boat helped prevent contamination of the specimen and allowed for easy removal from the furnace. The tests were carried out in a box furnace with molybdenum disilicide heating elements (RapidTemp, CM Furnaces Inc., Bloomfield, NJ) under stagnant ambient air conditions. The furnace was brought to the desired temperature and then the specimens were placed inside. Timing of each test was begun upon insertion of the specimen into the furnace. When opened, the furnace temperature fell $\sim 200^{\circ}\text{C}$, but returned to within 10°C of the testing temperature in 10 seconds and was constant at the testing temperature within 10 minutes.

Tests were run for a series of temperatures (1300°, 1400°, 1500°, 1550°C) for 10 seconds to 100 hours, using material from multiple bars. Tests conducted on material cut from the same bar are clearly indicated in the results. For the short-term tests (10 seconds-1 minute), the box furnace was heated to 1500°C, then the furnace was opened and the specimen was placed inside for the designated time. The temperature of the furnace dropped to ~1300°C upon insertion and then rose back to 1500°C in approximately 10 seconds. While the specimen temperature is not known precisely for the short-term tests, the exposures accurately represent the heating transient of the longer-term tests. Two specimens were also oxidized in the box furnace for 100 minutes at 1500°C with the specimen placed at an ~45° angle, as shown in Figure 6, in an attempt to characterize macroscopic glass flow.

Specimens were removed from the hot furnace and cooled rapidly to room temperature (<5minutes) in ambient air. Final dimensions and weight were recorded. The weight of the boat was also measured before and after testing and no significant weight change was found.

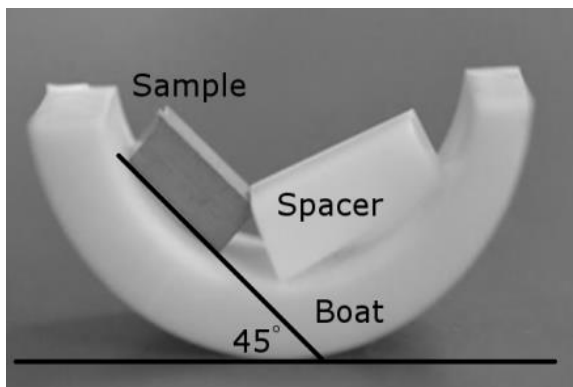


Figure 6. ZrB_2 -30 vol% SiC specimen in yttria stabilized zirconia (YSZ) boat with YSZ spacer at ~45° angle.

Resistive Heating

Resistive heating was used to test the oxidation behavior at ultra-high temperatures (1300°-1800°C), after a method first developed by Karlsdottir and Halloran, which they have called “the ribbon method”³¹. This method resistively heats the specimen using a high current, ~100 Amps, that runs through the specimen. As the resistance of ZrB_2 is similar to metals, $\sim 15 \times 10^{-6} \Omega \text{cm}$, this approach works well⁶⁷. A “ribbon” or bridge specimen, as seen in Figure 5b, is used for this technique, and the thin bridge region is $\sim 500 \mu\text{m}$ thick by $\sim 1500 \mu\text{m}$ wide, as described above. Prior to resistive heating oxidation, all specimens were cleaned using baths of detergent and DI water, DI water, acetone and then ethanol. The specified specimen geometry allows the center of the specimen, which is not in direct contact with any surfaces, to heat to ultra-high temperatures, while the supporting ends remain relatively cool, minimizing high temperature contamination and interaction of the specimen with the heating apparatus. This method has the advantage of being more economical than the arc-jet facilities and allows for more control than using an oxyacetylene torch, both alternative techniques for reaching $T > 1500^\circ\text{C}$.

The system set up is shown in Figure 7 through Figure 9. The specimen temperature was measured using an emissivity correcting infrared pyrometer (Pyrofiber Lab PFL-0865-0790-2500C311, Pyrometer Instrument Company, Windsor, NJ) with a spot size of 1.5mm, which automatically corrected for the changing emissivity (generally 0.80-0.99) of the oxidizing surface using pulsed laser technology. The pyrometer also controlled the current, which ran through the specimen by providing the temperature reading to a control unit with a Eurotherm controller (BPAN controller, Micropyretics Heaters International Inc., Cincinnati, Ohio). The control unit provided the changing current, which was passed through a transformer to step the

current up to the required level. The current running through the specimen was read continuously by a NI-6009 data acquisition card (DAQ) and the pyrometer was set to a data acquisition rate of ~4 measurements per second. Both the pyrometer temperature and the current were recorded by a computer.

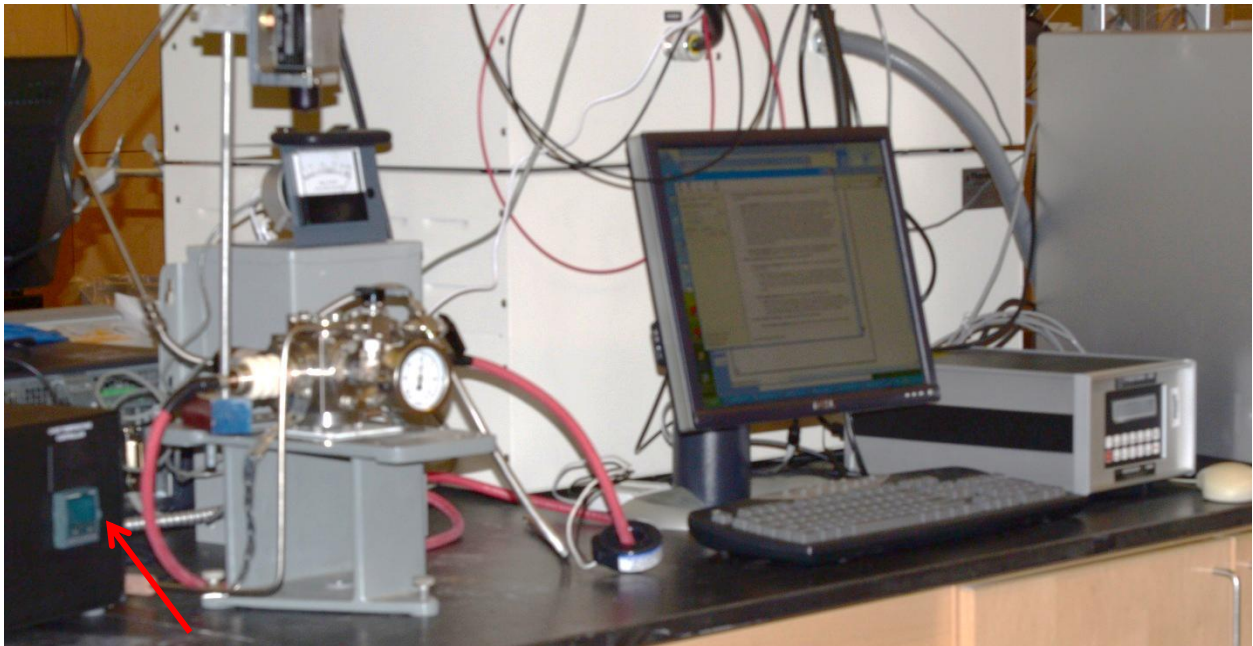


Figure 7. Resistive heating setup with specimen chamber, pyrometer, and recording computer.

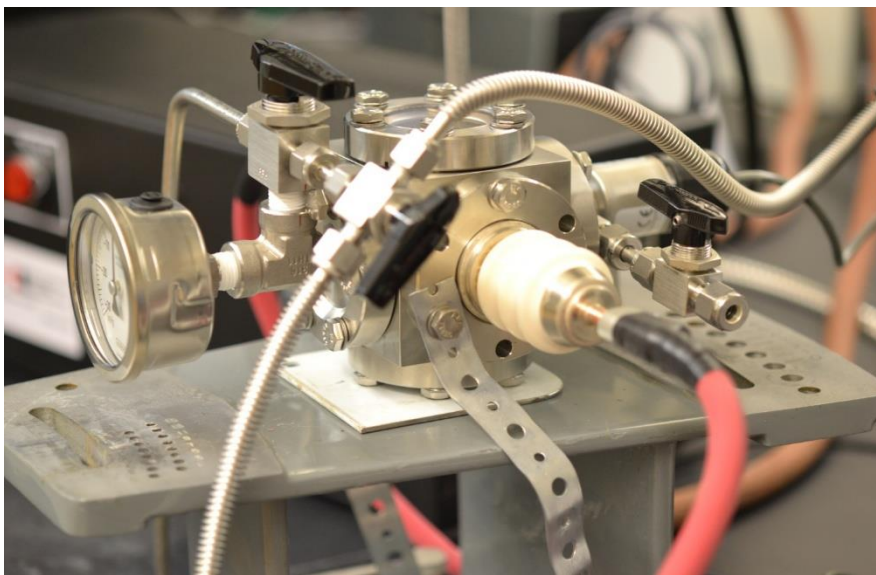


Figure 8. Resistive heating chamber with high current feed-throughs (red wires), $^{16}\text{O}_2$ and $^{18}\text{O}_2$ gas inlets, gas outlet, pump outlet, and low vacuum gauge.

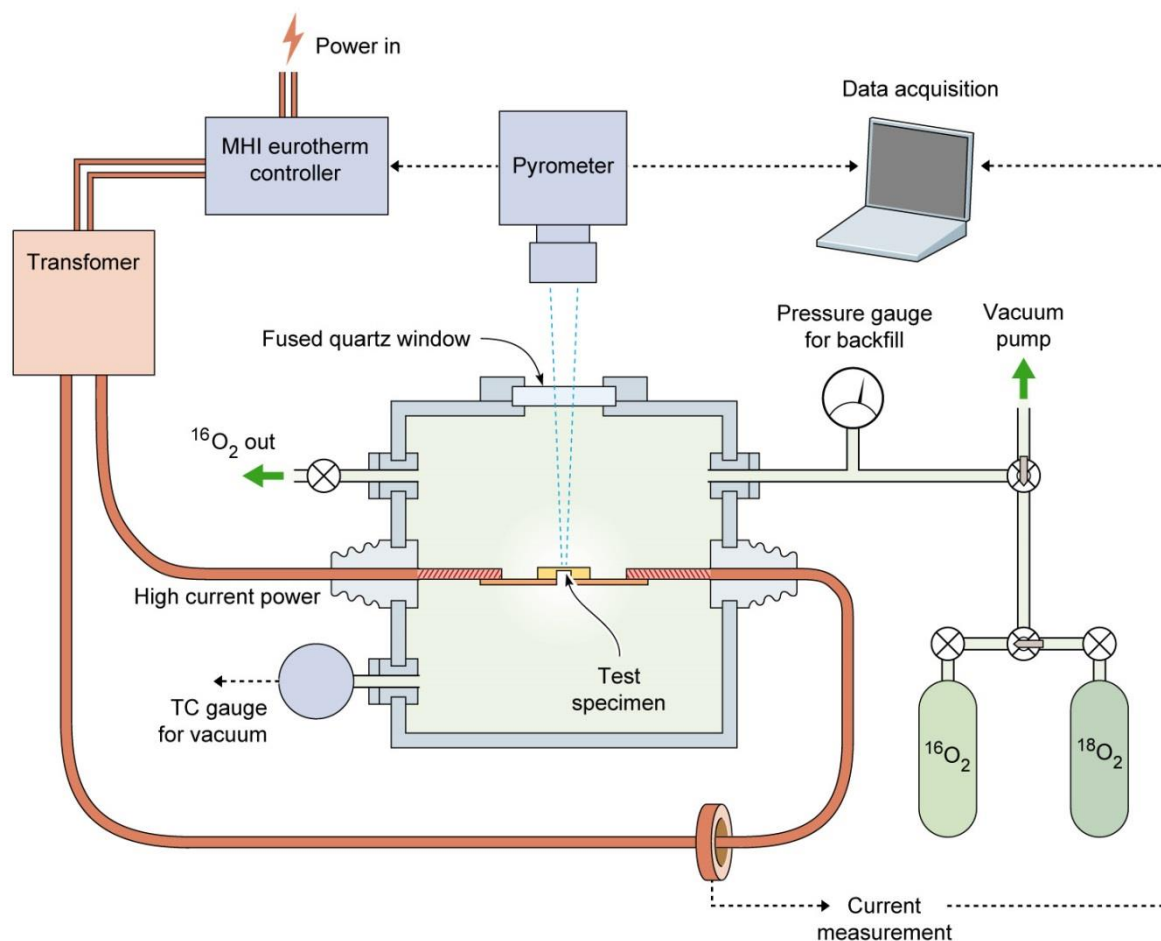


Figure 9. Schematic of resistive heating system.

For testing, each end of the bridge specimen was positioned on a section of flattened copper wire with a cross-section of 1.05mm x 2.85mm, which was attached to the current feedthroughs in the specimen chamber (Figure 10.) A piece of platinum foil (0.06mm thick, Heraeus Materials Technology, Chandler, AZ) was placed between the copper wire and the specimen to minimize reactions between the specimen and the wire. The specimen was held in place using toothless alligator clips, which were electrically isolated using 0.8mm thick sheets of Maycor (a glass-mica ceramic, McMaster-Carr, Robbinsville, NJ) or stabilized ZrO_2 (Ceramic

Technologies, Inc, Houston, TX). A bar of ZrO_2 was super glued to the side of the specimen to provide stability against torqueing when inserting the specimen into the system. $\text{B}_2\text{O}_3(\text{g})$ condensation on the window was prevented by flowing $\text{O}_2(\text{g})$ through the chamber at a rate of 900sccm. The $\text{O}_2(\text{g})$ flowed through drierite (CaSO_4) prior to entering the resistive heating chamber to maintain low humidity.

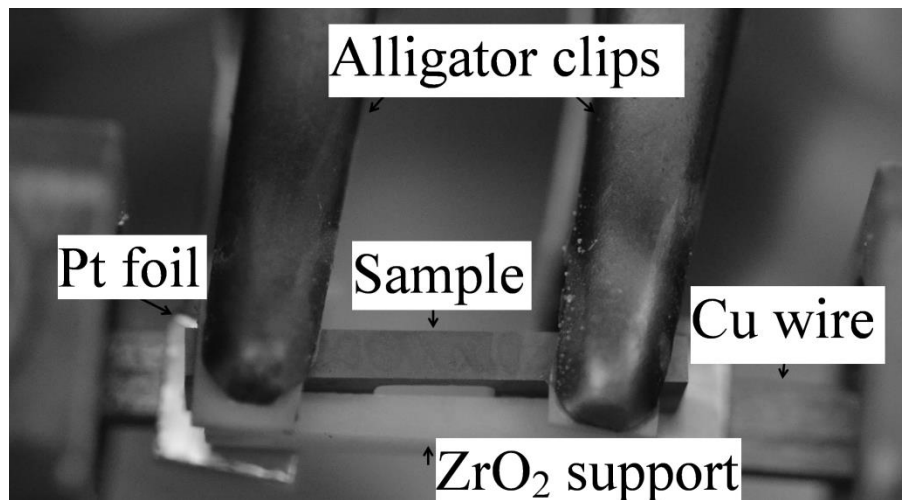


Figure 10. ZrB_2 -30 vol% SiC bridge specimen prepared for oxidation in resistive heating system and held into system using alligator clips.

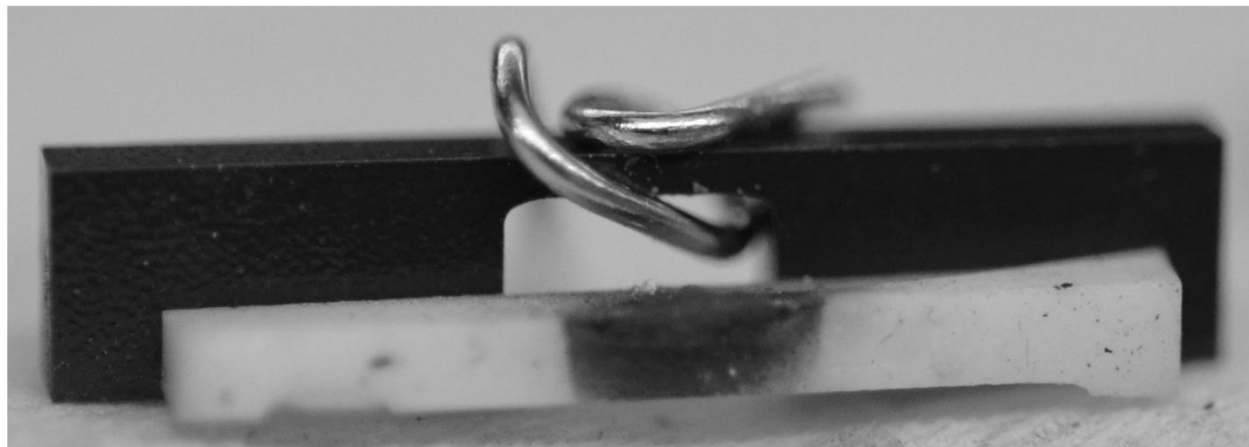


Figure 11. ZrB_2 -30 vol% SiC bridge specimen with Pt wire prepared for temperature calibration test in resistive heating system.

Pt (ϕ 0.508mm, Sigmund Cohn, Mount Vernon, NY) and Pd (ϕ 0.203mm, Alfa Aesar, Ward Hill, MA) wires were used as melting point standards (T_m = 1555°C and 1768°C) to confirm the pyrometer readings. The wires of each metal were wrapped around pre-oxidized bridge specimens, making certain to have good contact with the thin bridge region (Figure 11). The specimens were then inserted into the resistive heating system. The temperature of the specimen was slowly increased (10-20°C/min) while the wire was observed. When the wire melted, the set temperature of the control unit was recorded. Observed melting temperatures of the Pd and Pt wires occurred at set temperatures of 1527°C and 1752°C, respectively. These wire melting point tests indicate that the system operates within 28° of true temperature in the test temperature range (1500°C-1800°C), a reasonable accuracy given the difficulty of measuring ultra-high temperatures.

Tests were run at temperatures of 1300° to 1800°C for times of 5-70 minutes. The longest tests at 1700°C and 1800°C were 40 minutes and 20 minutes respectively due to near total oxidation through the 0.5mm thickness of the ZrB_2 -SiC specimens. After resistive heating oxidation, the bridge specimens were snapped in half, which often occurred naturally upon cooling. The fractured cross-sections were then characterized, as described in a later section. Further details of this resistive heating technique are given in Appendix 1. The resistive heating exposures performed are given in Appendix 2.

Comparison of Box Furnace and Resistive Heating System

Concerns exist that internal heating by resistive heating can result in different oxidation rates and microstructures when compared to conventional box furnace radiative heating. The validity of the resistive heating tests was established by comparing specimens exposed in the box furnace and resistive heating system. Both tests were performed on bridge specimens of ZrB_2 -30

vol% SiC oxidized for 20 minutes at 1500°C (near the maximum temperature capability of the box furnace.) The specimens were exposed in stagnant air (box furnace) and flowing O₂ (resistive heating). Both specimens were fractured after oxidation and characterized using SEM. A similar appearance of the oxide cross-sections was observed, as presented in Figure 12. The box furnace specimen showed an average borosilicate thickness of $5.5 \pm 0.8 \mu\text{m}$ and ZrO₂ thickness of $13.1 \pm 1.6 \mu\text{m}$. The resistive heating specimen showed an average borosilicate thickness of $7.1 \pm 0.8 \mu\text{m}$ and ZrO₂ thickness of $11.0 \pm 2.1 \mu\text{m}$. (Number of measurements used and locations chosen is described in a following section.) The similar oxide thicknesses and morphology show that the two tests are equivalent at 1500°C and no artifacts of resistive heating were observed. These tests also provide confirmation that the pyrometer reading at 1500°C is reasonably accurate for resistively heated specimens.

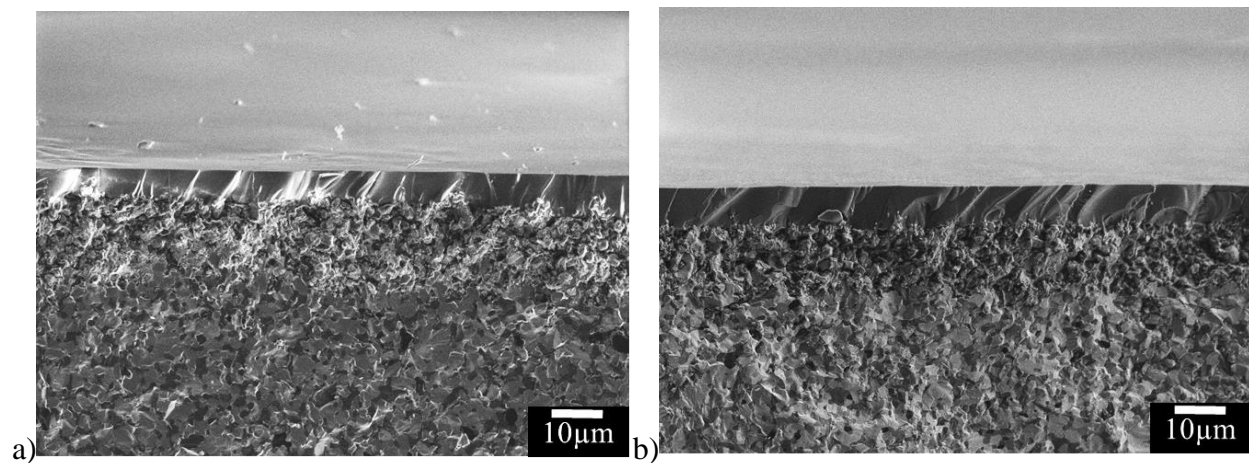


Figure 12. Fractured cross sections of ZrB₂-30 vol% SiC oxidized at 1500°C for 20 minutes using a) standard box furnace b) resistive heating system. Both cross sections display the same morphology and similar oxide thicknesses, indicating no artifacts from resistive heating.

Double Oxidation

Two stage oxidation experiments were performed using the resistive heating system for tracer diffusion studies. Specimens were oxidized for a pre-determined time under flowing standard lab grade $^{16}\text{O}_2$ (GTS-Wilco, Allentown, PA) as described above. Then the specimen was cooled to room temperature, which happens rapidly once the current flow ceases, and the gas flow was turned off. The specimen was then reinserted with new copper wire and platinum foil if needed. The system was pumped down to a pressure of 1.3×10^{-2} Pa or below, current and temperature acquisition were re-started, and the specimen was brought back up to temperature. Then the system was backfilled with $^{18}\text{O}_2$ (97% enrichment, Sigma Aldrich, Saint Louis, MO) to 1×10^{-5} Pa and the specimen was oxidized for a second pre-determined time. A baseline exposure was performed using $^{16}\text{O}_2$ for both oxidation stages to show that normal oxidation behavior was observed when the specimen was heated twice (Figure 13). The $^{18}\text{O}_2$ tracer exposures performed are listed in Table 2. These tests did show total ZrO_2 layer growth similar to the predicted growth, further proving normal oxidation behavior for resistive heating and double oxidation.

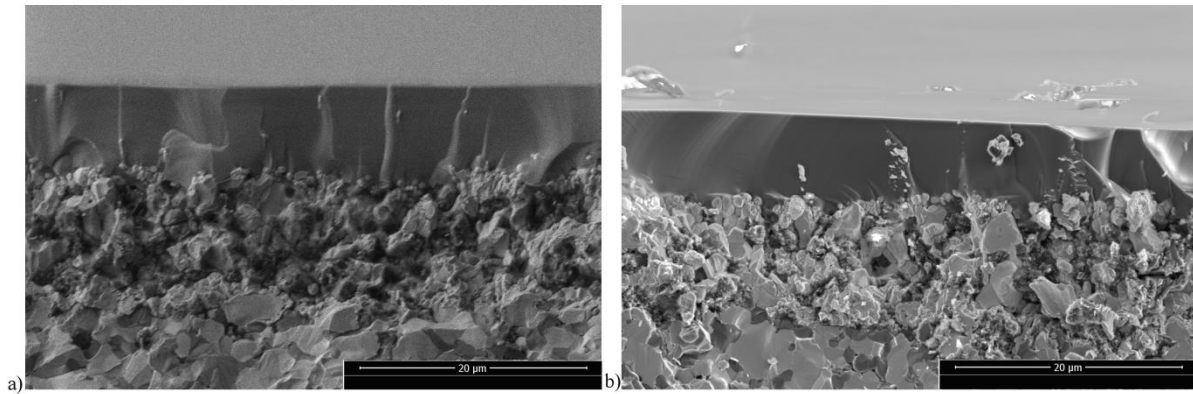


Figure 13. Fractured cross sections of ZrB_2 -30 vol% SiC oxidized using the resistive heating system at 1500°C a) for 20 minutes consecutively b) for 20 minutes in 2 stages (15 minutes and 5 minutes). Both cross sections display the same morphology and similar oxide thicknesses, indicating no artifacts from double oxidation.

Specimen	$^{16}\text{O}_2$			$^{18}\text{O}_2$			Additional Information
	Time (min)	Temperature ($^{\circ}\text{C}$)	ZrO ₂ grown (μm) [†]	Time (min)	Temperature ($^{\circ}\text{C}$)	ZrO ₂ grown (μm) [†]	
95	20	1500	11	3	1200	--	Not Observed
80	15	1500	9	5	1500	2	Observed, sectioning beveled oxide layers
89	19	1500	11	1	1500	<1	Observed, sectioning formed Zr-Si-O phase
76 *	10	1500	8	9	1500	3	Observed
93 *	29	1650	64	0.75	1650	<1	Observed, oxidized through but was able to section lower in hot zone
79 *	45	1650	80	5	1650	4	Observed

Table 2. Conditions for Double Oxidation Experiments of ZrB₂-30 vol% SiC. * indicates sectioned specimen was successful for ToF-SIMS. [†] ZrO₂ growth is calculated using experimental k_p values.

Conventional mounting and polishing of specimen cross-sections resulted in surfaces too rough for Time of Flight- Secondary Ion Mass Spectrometry (ToF-SIMS), due to the significant differences in hardness of ZrB₂, ZrO₂, SiC, C, and borosilicate glass. Instead, the double oxidization specimens were fractured and half of each specimen was ion polished (Dr. Marshall, Teledyne Scientific, Thousand Oaks, CA; JEOL Cross Section Polisher SM-09010, Tokyo, Japan.) For this process, a thin layer of metal (Au) was deposited on the top surface to make contact with the knife blade that defines the position of the ion polished surface. The specimens were then polished back directly from the fracture surface with an Ar ion beam. Due to the rough nature of the fracture surface, several iterations of ion milling were performed. The final ion polished specimen provided the smooth surface needed for ToF-SIMS.

Characterization

Oxidized specimens were stored in a desiccator cabinet to minimize reaction of any B_2O_3 remaining in the specimen with water vapor in the air. The oxidized specimens were characterized in plan view and cross-section using Scanning Electron Microscopy (SEM, JEOL 6700F, Tokyo, Japan; FEI Quanta 600F, Hillsboro, OR) and Energy Dispersive Spectroscopy (EDS, Princeton Gamma-Tech Inc., Princeton, NJ; Oxford Instruments Aztec X-Max^N 150, Concord, MA) after the surface was coated with a thin layer of carbon. (During the course of this research, available SEM/EDS capabilities varied.) An operating voltage of 5kV was used to maximize the EDS signal intensity for light elements, unless otherwise specified. To observe oxide thicknesses of box furnace oxidized specimens, the specimens were mounted in epoxy while under vacuum, cross sectioned using a diamond blade, and remounted in epoxy. The first epoxy mount was performed in an attempt to prevent pullout and spallation of the oxide during sectioning and polishing. Even with careful polishing SiO_2/SiC appears to pull out from the ZrO_2 oxide layer, resulting in the appearance of SiC depletion, as will be discussed in Chapter 5. The cross sections were polished using diamond polishing paste down to $1\mu m$ in a mixture of ethylene glycol and 200 proof ethanol, and then coated with carbon. Nonaqueous ethylene glycol and 200 proof ethanol were used as lubrication during specimen preparation to minimize loss of B_2O_3 , which is soluble in water. Average grain sizes for both cross sections and surface views were determined using the lineal intercept method in at least 3 regions of each specimen and using at least 50 grains per region. Oxide layer thicknesses were determined by measuring the thicknesses in a minimum of 20 random locations over the cross section and averaging. X-ray diffraction (XRD) was performed on the unoxidized and representative oxidized specimens (Panalytical X'Pert Diffractometer, Westborough, MA).

X-ray Photoelectron Spectroscopy (XPS, PhiVersa Probe XPS spectrometer, Chanhassan, MN) was performed at Case Western Reserve University (CWRU, Cleveland, OH) on the surface of specimens oxidized for 10 and 20 seconds and 10 and 100 minutes at 1500°C. XPS was performed using monochromated Al K α radiation of 1486.6eV, with a bandpass energy of 11.75eV and an increment of 0.1eV/step. The resolution on Ag_{3d₅} is 0.6eV. The analyzed area for each specimen was about 0.5mm² and the scans were performed under identical conditions. Curve fitting was done using the Gaussian-Lorentzian peak and a Shirley background algorithm of the PHI data massaging program MultiPak^{68, 69}. Depth profiling was performed using Ar sputtering at 3kV energy on a non-spinning specimen. The calibration standard for the rate of sputtering was electrochemically grown Ta₂O₅ and the calibration was done with 100 nm layer of oxide on foil. The sputter rate was determined to be ~6nm/min sputter rate on Ta₂O₅ foil and is likely very similar, or slightly slower in this material as SiO₂ is slightly slower to sputter.

EDS (Oxford Instruments Aztec X-Max^N 150, Concord, MA) was performed on the surface of a specimen oxidized at 1500°C for 100 minutes using a series of electron beam accelerating voltages (5kV, 10kV and 20kV). The change in B composition with accelerating voltage and sampling depth was used to provide additional information about the B concentration profile in the borosilicate glass. The depth of the interaction volume for each energy was determined using the Casino simulation program and densities for borosilicate glass at each composition in an iterative method⁷⁰. See Appendix 3 for more information on the Casino simulation process.

To determine the average composition of the borosilicate layer of the formed oxide, Inductively Coupled Plasma Optical Emission Spectroscopy (ICP-OES, Thermo-Scientific, Waltham, MA) was performed. This required the oxide to be dissolved, first in a water soak (to

remove B₂O₃) and then an HF soak (to remove SiO₂). Comparison of the emission spectra from each solution to prepared standards of known concentrations and normalized with an internal yttrium standard allowed for precise composition measurements. Details of this process are given in Appendix 4.

Time of Flight-Secondary Ion Mass Spectrometry (ToF-SIMS, PHI THRIFT V nanoToF, Chanhassan, MN) was performed at CWRU on cross-sectioned specimens after double oxidation in ¹⁶O₂ and ¹⁸O₂. ToF-SIMS is sensitive to both elements and isotopes, and can map the location of ¹⁶O₂ and ¹⁸O₂. The ToF-SIMS uses a GaAu gold gun and the ion beam is accelerated to 30kV. The unwanted ions are filtered out by mass, so that only singly charged Au ions impinge on the surface. These primary ions sputter the surface, ejecting secondary ions (or neutral atoms), which are separated by mass. The secondary ions are accelerated into the detector (Trift detector-Dual MicroChannel Contrast Diaphragm) and analyzed by time of flight, which varies according to mass.

There are two data collection modes available, mass resolution and spatial resolution. The instrument also operates in either positive or negative mode, collecting positive or negative ions favorably in each mode. Mass resolution mode has a resolution on the order of milli-amu, and was used here to confirm the isotopes present in the oxidized cross section specimen. Mass calibration in the negative operation mode was done with peaks of CH, OH, and C₂H. Positive operation mode used CH₃, C₂H₃, and C₃H₅. Spatial resolution mode has a resolution between ~3nm to 0.5μm without fine tuning, and was used to map the location of the ions of interest. For the specimens analyzed in this work, positive mode was used to collect Zr, Si, and B, while negative mode was used to collect C, ¹⁶O₂, and ¹⁸O₂.

Limitations of the ToF-SIMS technique include the requirement for a flat specimen to obtain data as surface roughness leads to regions with low ion signal. Avoiding epoxy in specimen mounting and polishing is also beneficial as epoxy can lead to specimen charging. When collecting data, it is important to be aware of the ions which can be detected in each mode. There is an image shift when switching between modes, and no fine stage control. This means the same area cannot be imaged for both modes, especially at high magnification (micrograph width less than $\sim 100\mu\text{m}$). Due to the image shift, it is not possible to image the exact same grains at high magnification when looking for O (collected in negative mode) and Si or Zr (collected in positive mode), making it difficult to judge if the ^{18}O is in the borosilicate or the ZrO_2 , unless EDS can be performed on the same grains. It should also be noted that different phases may release ions at different rates. This means that in one map, intensity changes between phases may not directly correspond to concentration changes. In addition, due to the strong gettering nature of ZrB_2 , both ZrB_2 and ZrO_2 grains appear to contain ^{16}O , making it impossible to use ^{16}O maps to determine the location of the oxide. Since $^{18}\text{O}_2$ is not abundant in the atmosphere, maps of ^{18}O are still accurate representations of the location of oxide containing ^{18}O .

Thermodynamic Calculations

Factsage (version 6.3), a computer program for chemical thermodynamics calculations based on Gibbs' free energy minimization⁷¹, was used for all thermodynamic analysis performed in this work. The Fact pure substances (FactPS) database was chosen.

Chapter 4 Task 1- Variability of Oxidation Kinetics

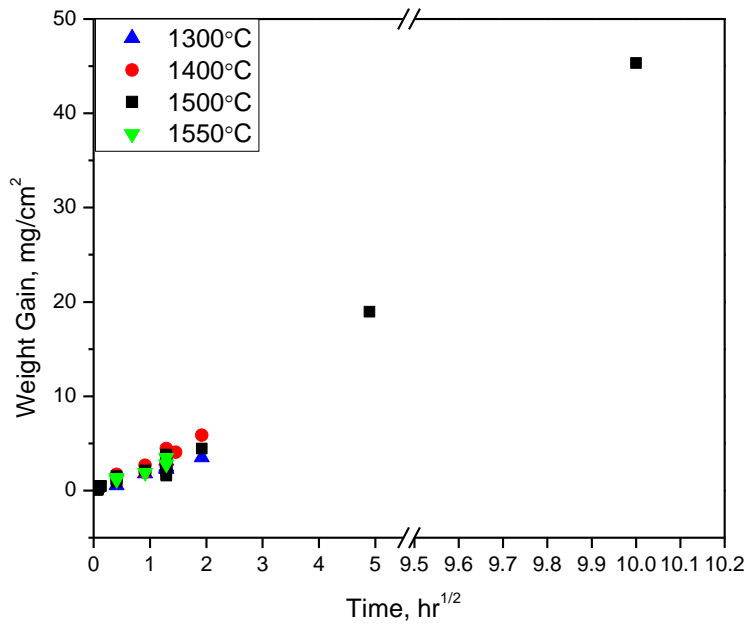
Objective

This task aimed to determine oxidation kinetics of ZrB_2 -30 vol% SiC through quantitative microscopy and careful mass gain measurements. This task studied the observed variability of measurements of oxidation kinetics and products of ZrB_2 -30 vol% SiC. A number of mechanisms were considered to explain this variability, including initial inhomogeneities in oxide phase distribution, macro flow of the borosilicate glass, surface roughness, humidity, and bubble formation.

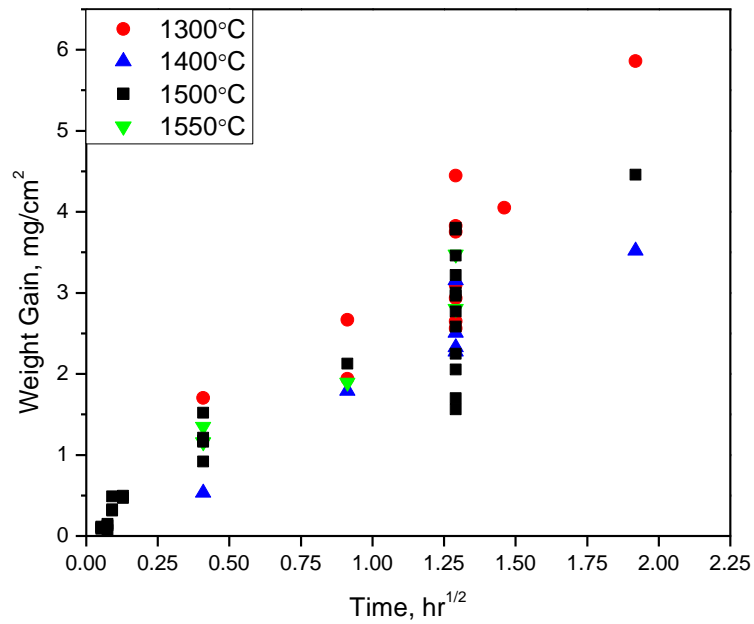
Results

Oxidation Kinetics

All mass gain measurements taken throughout this study are shown in Figure 14. The results were combined and plotted as mass gain per surface area versus square root of time to best account for the transient oxidation behavior at short times⁷². The specific mass change results at one oxidation time, 100 minutes, at each temperature are shown in Figure 15. At 1500°C, the mass gain for seven tests under identical testing parameters was $2.54 \pm 0.73 \text{ mg/cm}^2$ where the uncertainty reflects one standard deviation. When three specimens from a single bar were tested, the mass gain was $1.77 \pm 0.26 \text{ mg/cm}^2$. Average oxide thicknesses over all tests performed for 100 minutes are reported in Table 3, again showing large standard deviations. The cross sections in Figure 16 show that even within a single specimen there is large variation in oxide layer thicknesses. Standard deviations of the oxide layer thicknesses are between 30-80% of the average thickness when analyzing any single specimen. Figure 17 shows some correlation between ZrO_2 and borosilicate glass thicknesses exists.



a)



b)

Figure 14. Specific mass change (mg/cm²) for ZrB₂-30 vol% SiC oxidized in standard box furnace in ambient air as a function of time and temperature. a) Provides data for all times b) provides data for times under 4 hours for easier differentiation.

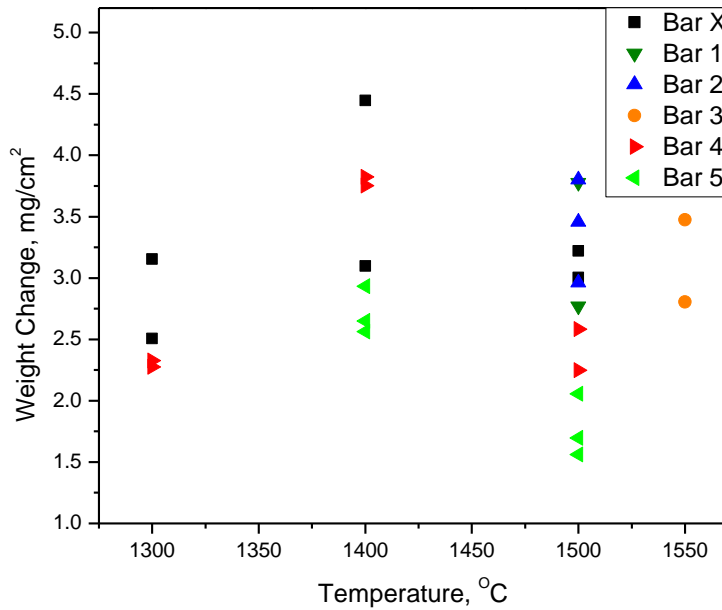


Figure 15. ZrB₂-30 vol% SiC mass gain after 100 minute exposures in standard box furnace in ambient air showing large variation in material behavior, even when specimens are cut from the same initial bar. Bar X indicates that no specific bar was identified.

Temperature (°C)	ZrO ₂ thickness (μm)	Std. dev. (μm)	Borosilicate thickness (μm)	Std. dev. (μm)	Total oxide thickness (μm)	Std. dev. (μm)	# of specimens measured (Avg. # of measurements per specimen)
1300	25.1	8.7	7.7	6.0	32.8	6.3	1 (19)
1400	15.3	13.3	22.1	15.3	37.5	17.3	3 (35)
1500	21.9	15.6	27.6	20.5	39.6	26.4	6 (45)
1550	23.2	10.7	14.9	6.9	38.0	9.9	1(64)

Table 3. Thickness of oxide layers formed on ZrB₂-30 vol% SiC after oxidation in standard box furnace in ambient air for 100 minutes as a function of temperature. Large standard deviations are seen for all oxide thicknesses.

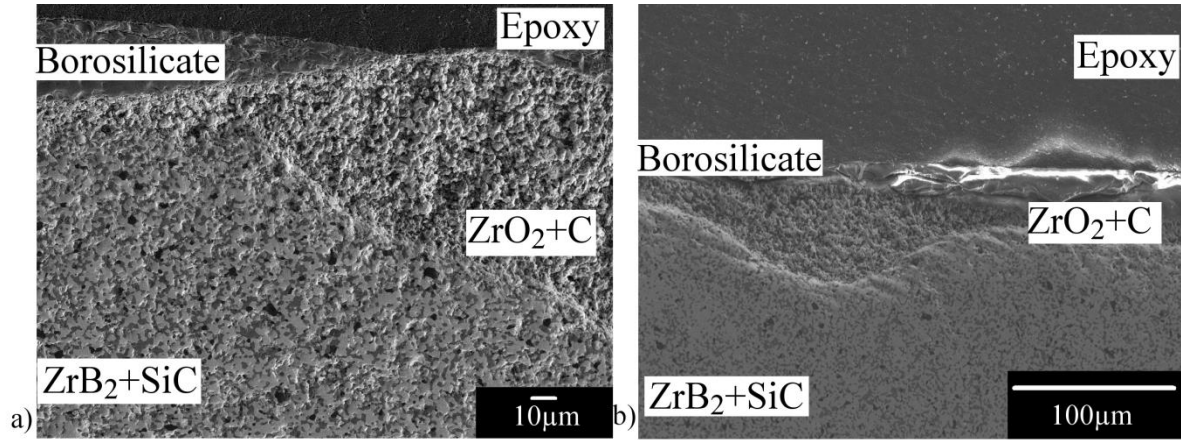


Figure 16. Mounted and polished cross section of ZrB_2 -30 vol% SiC exposed for 100 minutes in standard box furnace in ambient air at a) 1400°C b) 1500°C showing variation in layer thicknesses and scalloped penetration depths of oxidation.

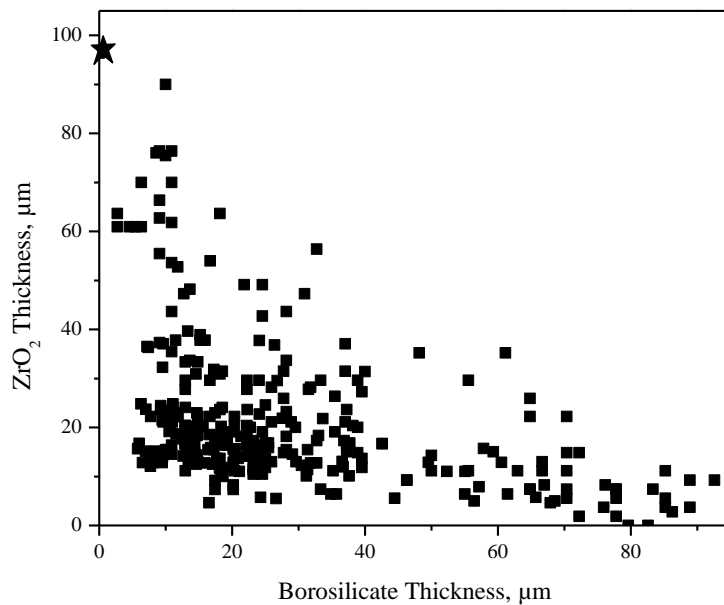


Figure 17. Dependence of ZrO_2 thickness on borosilicate thickness for a single specimen oxidized 100 minutes at 1500°C in standard box furnace in ambient air. Oxidation resistance provided by borosilicate glass is apparent. Star indicates maximum oxidation depth, used in maximum mass gain prediction.

All oxidation mass gain results for each temperature between 1300°C and 1550°C (except the 24 and 100 hour tests) were plotted as mass gain per surface area versus square root of time, to determine the parabolic oxidation rate constant. The two longer term tests at 1500°C were excluded to analyze the predictive capabilities of the results from times of 4 hours and less. The predictive capabilities of short-term oxidation will be discussed later. From the plots, parabolic rate constants (k_p) were calculated as reported in Table 4. A 95% confidence interval was determined for the slope of each plot, and from this, a maximum k_p was calculated. The mass gain and calculated rate constants for the 1500°C tests are shown in Figure 18.

Paper	SiC content	Temperature (°C)	Time (minutes)	Mass change (mg/cm ²)	k_p (mg ² /cm ⁴ h)	Maximum k_p (95% confidence) (mg ² /cm ⁴ h)
This study	30	1300	100	2.57±0.4	4.0	10.6
		1400	100	3.36±0.8	7.4	24.7
		1500	100	2.73±0.8	4.4	12.9
		1550	100	3.14±0.5	4.4	11.6
20, 24	20	1327	10	1.25	4.9, 6.3	
			50	2		
			100	2.5		
		1627	10	3.75	100	
			50	8.75		
			100	13		
15	20	1627	10	1.8	10.94	
			50	3		
			100	4.5		
	33.3	1627	10	3.5	NA	
			50	5.2		
			100	5.3		

Table 4. Comparison of literature and experimental results for oxidation of ZrB₂-SiC in standard box furnace in air. k_p s calculated for this work are of the same order of magnitude as the literature.

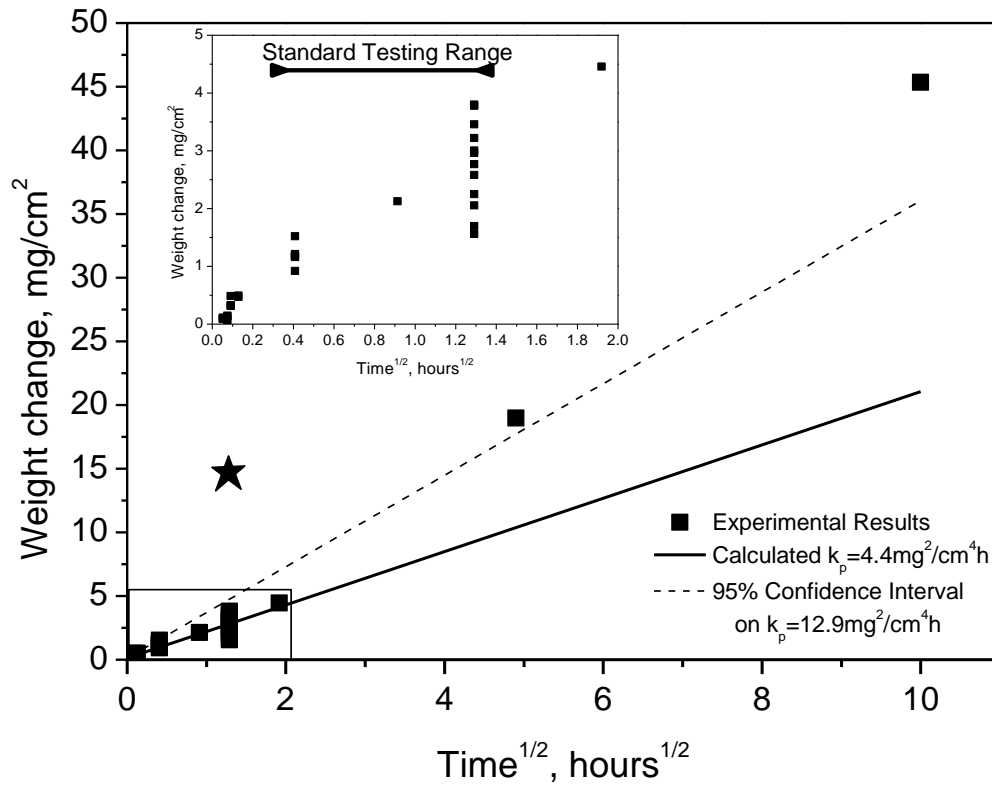


Figure 18. Specific mass change (mg/cm^2) for ZrB_2 -30 vol% SiC oxidized at 1500°C in ambient air, compared to both average k_p and the 95% confidence interval on k_p , calculated from results up to 4 hours. Insert corresponds to the boxed region. Star indicates maximum mass gain predicted using maximum oxidation depth. (See Figure 17.) Long term oxidation (24 and 100 hour tests) are much higher than calculated k_p or 95% confidence interval.

Initial Stage Oxidation

The short-term ZrB₂-30 vol% SiC oxide growth morphology was characterized and compared to the as-received specimen surfaces for oxidation times of 10, 20, 30 seconds, 1 and 10 minutes at 1500°C. Table 5 describes the oxide distributions, which are shown in Figure 19 through Figure 23. Mass change due to oxidation at 1500°C for all times is presented in Table 6. For reference, the as-received specimens contained ZrB₂ grains of 1.4±0.8µm in diameter and SiC grains of 0.9±0.5µm. As determined by SEM, small ZrO₂ grains completely covered the surface ZrB₂ at even the shortest 10 second exposure. The ZrO₂ grains grew with time as quantified in Table 5. Figure 22 shows that the size of the ZrO₂ grains visible on the surface after 30 seconds of oxidation was not regular, and regions much larger than the initial grain size had distinctly different visible ZrO₂ patterns.

Time	ZrO₂ grain size	Borosilicate distribution	Figures
10 seconds	80nm±3	Partial coverage of SiC	19, 20
20 seconds	167nm±52	Complete coverage of SiC Partial coverage of ZrO ₂	21
30 seconds	85nm±20 on surface 268nm±92 inside burst bubble 300-2000nm (in cross section)	Complete coverage of SiC Nearly complete coverage of ZrO ₂ Bubbles in glass layer	22, 23
1 minute	Small islands over surface	Continuous	
10 minutes	166nm±58 or several microns on surface 404nm±196 inside burst bubble	Continuous	

Table 5. ZrO₂ and borosilicate glass distributions after short-term oxidation of ZrB₂-30 vol% SiC (as-received surface) in ambient air at 1500°C in standard box furnace.

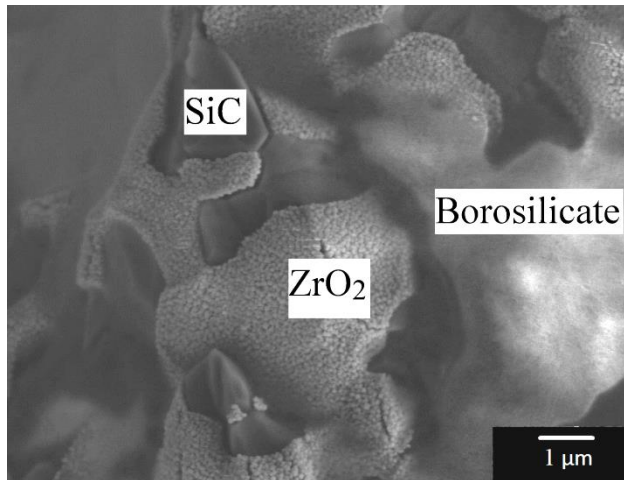


Figure 19. ZrB₂-30 vol% SiC (as-received surface) after 10 second exposure at 1500°C in ambient air in standard box furnace showing the beginning of the oxide coverage of SiC by borosilicate glass and the oxidation of ZrB₂ to nano-scale ZrO₂.

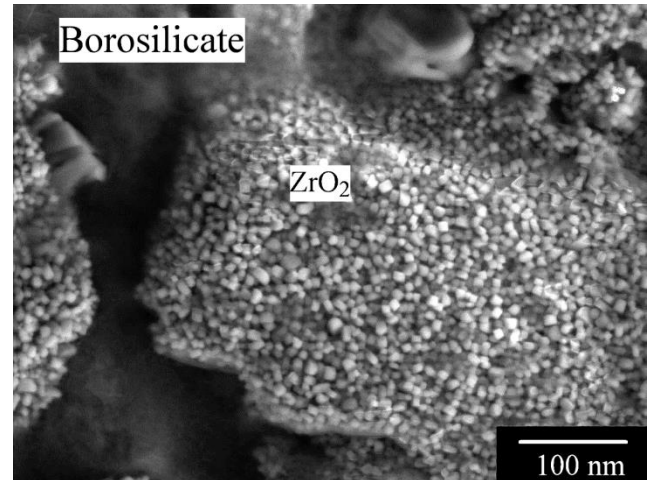


Figure 20. ZrB₂ grain in as-received ZrB₂-30 vol% SiC (as-received surface) oxidized to ZrO₂ grains (~80nm grain size) after 10 second exposure at 1500°C in ambient air in standard box furnace.

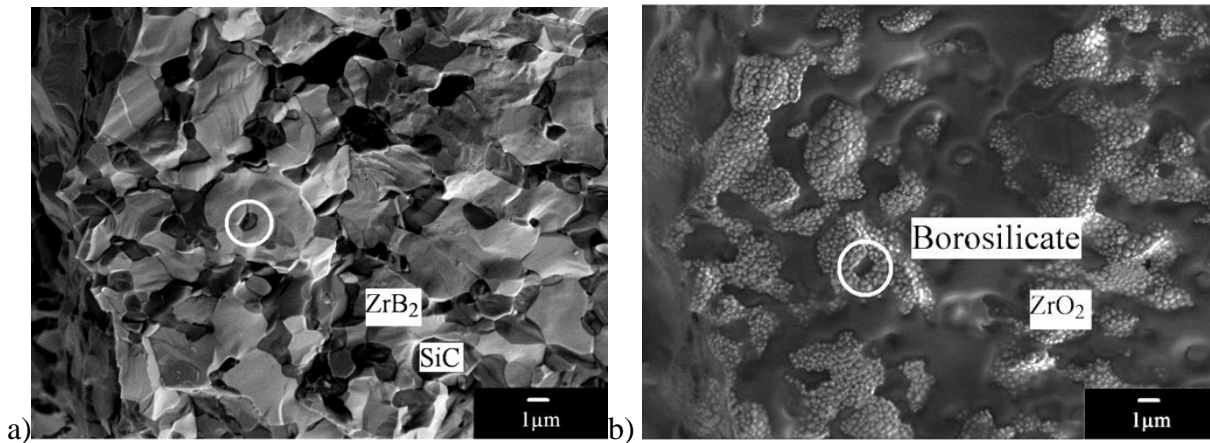


Figure 21. ZrB₂-30 vol% SiC (as-received surface) a) prior to oxidation b) after 20 second exposure at 1500°C in ambient air in standard box furnace (circle marks the same feature in both). Borosilicate glass has spread over the SiC grains and some ZrB₂/ZrO₂ regions. ZrO₂ grains are larger than after 10 second exposure at 1500°C.

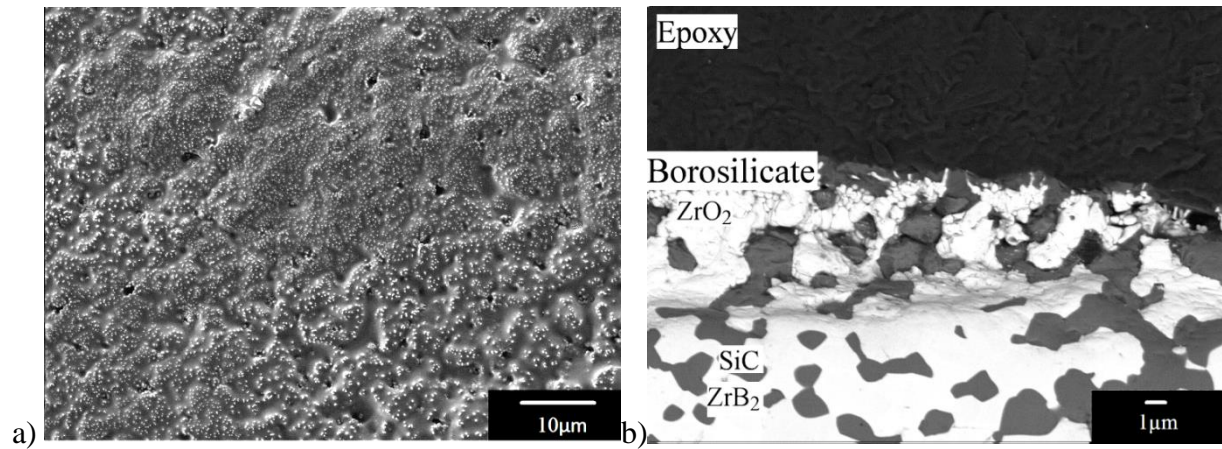
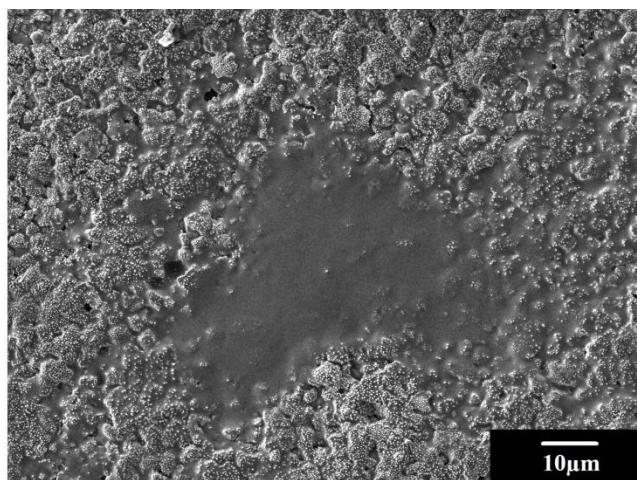
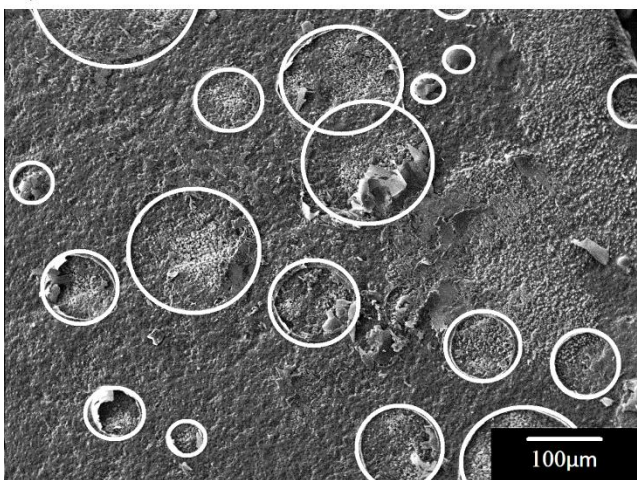


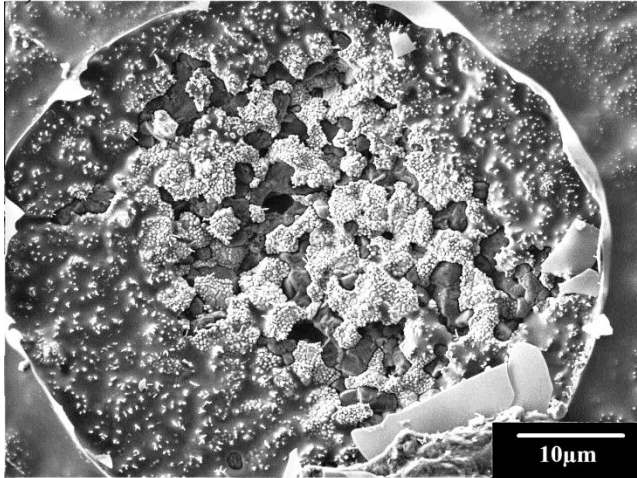
Figure 22. ZrB₂-30 vol% SiC (as-received surface) after 30 second exposure at 1500°C in ambient air in standard box furnace, a) surface view, b) cross section. Borosilicate glass has spread over entire surface with uneven regions of ZrO₂ exposure.



a)



b)



c)

Figure 23. ZrB_2 -30 vol% SiC (as-received surface) after 30 second exposure at 1500°C in ambient air in standard box furnace showing a) a borosilicate glass pool, b) bubbles on the surface, highlighted with white, and c) the ZrO_2 grains within a burst bubble.

Time	Surface finish (prior to oxidation)	Average mass gain/surface area (mg/cm ²)	Standard deviation (# of specimens)
10 seconds	As-received	0.10	0.02 (3)
	Polished	0.10	-- (1)
20 seconds	As-received	0.11	0.05 (3)
	Polished	0.13	-- (1)
30 seconds	As-received	0.38	0.10 (3)
1 minute	As-received	0.48	0.18 (2)
10 minutes	As-received	1.30	0.19 (6)
50 minutes	As-received	2.13	-- (1)
100 minutes	As-received	2.54	0.73 (14)
	Polished	2.96	-- (1)

Table 6. Mass gain due to oxidation of ZrB₂-30 vol% SiC in ambient air at 1500°C in standard box furnace. As-received and polished surfaces prior to oxidation show average mass gains within a standard deviation of each other.

At 10 minutes, XRD indicated the surface oxide was thicker than the XRD penetration depth, as shown in Figure 24. Note as oxidation time increased, the decrease of the major ZrB₂ peak at 2 Theta= 41° and the increase of the major ZrO₂ peak at 2 Theta=28°. While the XRD plot indicated monoclinic ZrO₂, it is expected that at 1500°C the ZrO₂ had a tetragonal crystal structure and transformed upon cooling. The borosilicate phase is expected to be amorphous and thus did not show peaks in XRD. The borosilicate glass initially formed on SiC grains (10 seconds) and began covering the ZrO₂ grains (20-30 seconds.) Borosilicate glass formation at 10 seconds was confirmed by XPS (described below.) By one minute, the borosilicate glass layer continuously covered the surface with only small ZrO₂ islands exposed (Figure 25.) After 10 minutes, very little ZrO₂ was seen on the surface, though that which did appear was no longer fine grains, but grains several microns or more in size (Figure 26.)

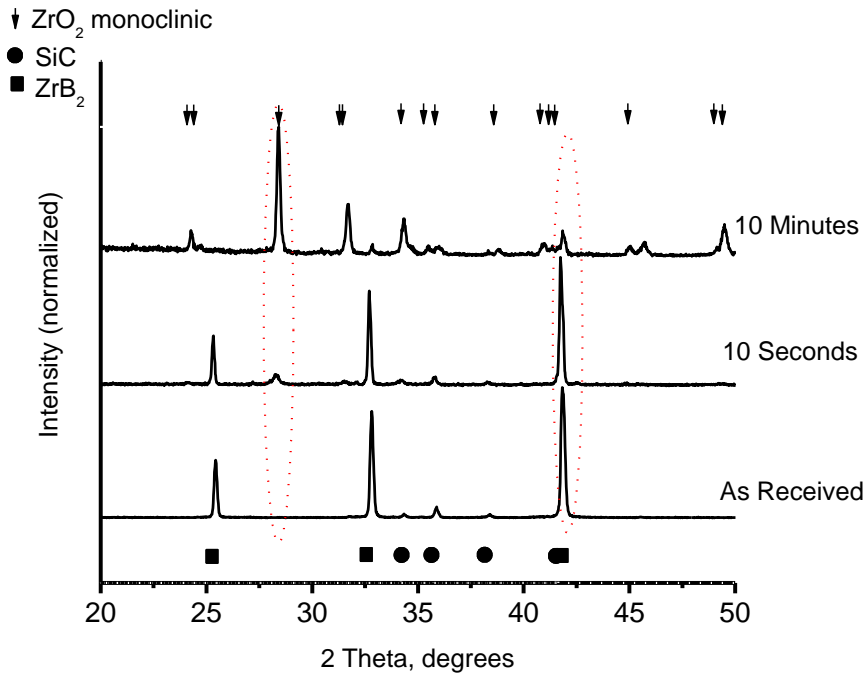


Figure 24. XRD Pattern of as-received ZrB₂-30 vol% SiC and after 10 seconds and 10 minutes at 1500°C in ambient air in standard box furnace showing the oxidation of ZrB₂ to ZrO₂ as a function of time. Note as oxidation time increased, the decrease of the major ZrB₂ peak at 2 Theta= 41° and the increase of the major ZrO₂ peak at 2 Theta=28°.

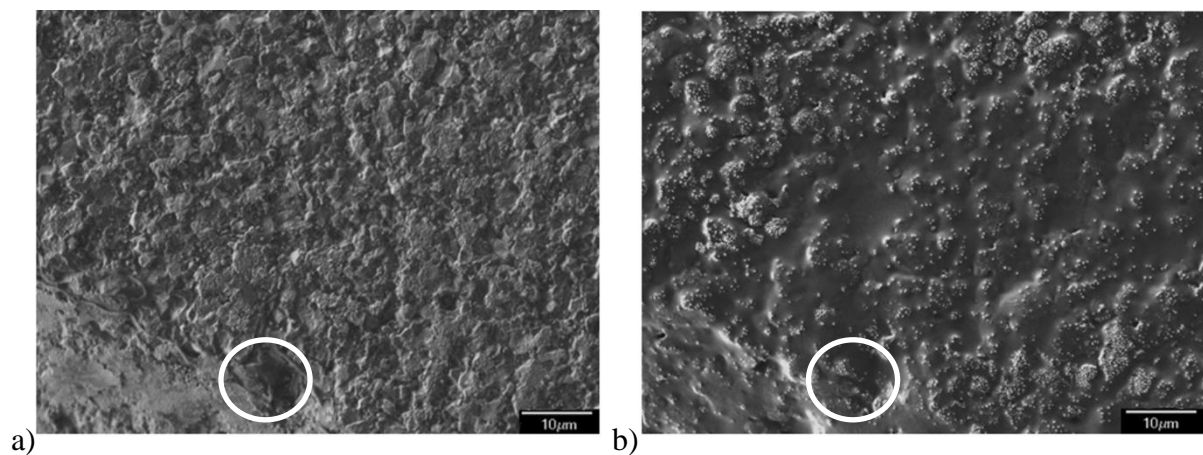


Figure 25. ZrB₂-30vol%SiC a)prior to oxidation, showing cut mark on bottom left b) after 1 minute exposure, with cut mark still visible though partly filled on bottom left (circle marks the same feature in both.) Borosilicate glass has covered the surface and most of the ZrO₂ grains. The exposed ZrO₂ is unevenly distributed.

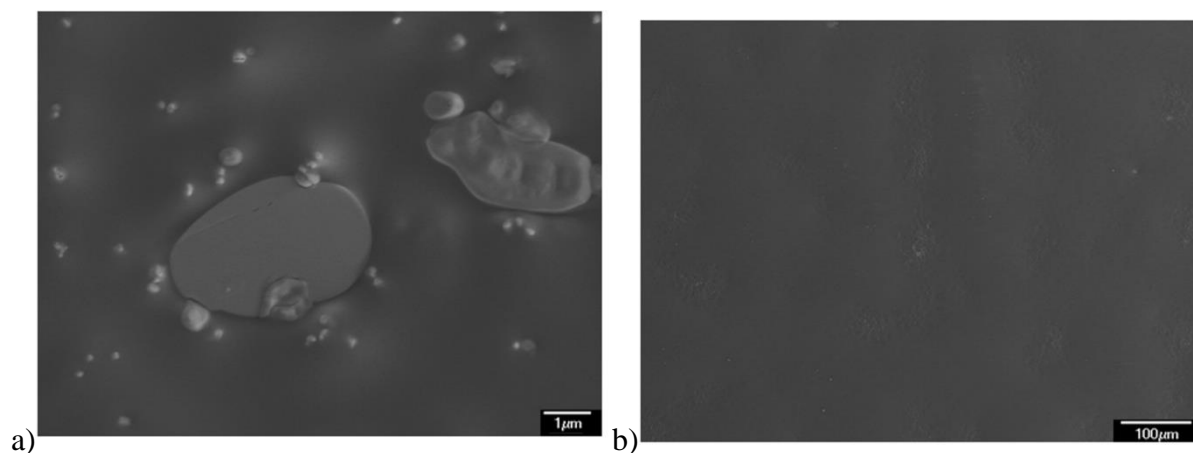


Figure 26 ZrB_2 -30vol%SiC after 10 minute exposure at 1500°C a) at 10,000X b) at 150X. The borosilicate glass has covered the entire surface. Only a few, large regions of ZrO_2 are seen, as in a).

Initial Oxide Composition

XPS was used to clarify the composition of oxide phases forming at short times. XPS results are shown in Table 7 and Figure 27. For the sample oxidized at 1500°C for 10 seconds, the SiO_2 2p peak at 103.3eV was used as a charge reference. The Si 2p peak was deconvoluted into 2 components, Si-O bonds of SiO_2 are seen at 103.3eV and Si-C bonds of SiC are seen at 100.3eV^{73, 74}. The Zr 3d peaks could be identified as a spin-orbit coupling of Zr-O bonds corresponding to ZrO_2 . The first is at 182.9eV ($\text{Zr}_{5/2}$) and the second is at 184.9eV ($\text{Zr}_{3/2}$)⁷⁴. The B 1s peak was deconvoluted into 2 significant peaks, the main peak at 193.7eV corresponds to B-O bonds for B_2O_3 ⁷⁴. A small peak at 190.3eV is consistent with a boride peak energy, which is due to sampling ZrB_2 on the surface⁷³. The C 1s peak shows some remaining SiC on the surface, through the low shoulder peak located at 282.5eV⁷⁴. The rest of the C peak can be attributed to adventitious carbon and other surface contamination. The O 1s peak is deconvoluted into 3 wide peaks. The lowest is at 530.6eV and is attributed to the Zr-O bonds of ZrO_2 , the next at 533.1eV corresponds with the Si-O bond of SiO_2 and the highest peak at 534.2eV corresponds to B-O

bonds of B_2O_3 ⁷⁴. B_2O_3 and SiO_2 are difficult to distinguish using the O 1s peak as they have bonding energies in the same range⁷⁴.

Spint-orbit Doublet	Binding Energy (eV)	Chemical Bonds	Compounds
Zr 3d_{5/2}	182.9	Zr-O	ZrO ₂
Zr3d_{3/2}	184.9	Zr-O	ZrO ₂
Si 2p	100.3 103.3	Si-C Si-O	SiC SiO ₂
O1s	530.6 533.1 534.1	O-Zr O-Si O-B	ZrO ₂ SiO ₂ B ₂ O ₃
C 1s	282.5	C-Si	SiC
B1s	190.3 193.7	B-Zr (?) B-O	ZrB ₂ B ₂ O ₃

Table 7. XPS energy assignments for spectra shown in Figure 27. (?) indicates uncertainty in identification.

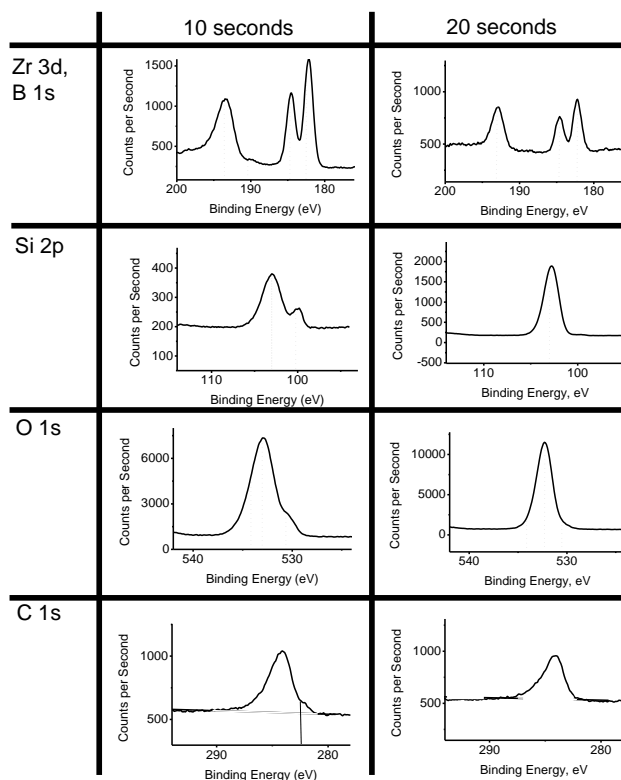


Figure 27. XPS results for as-received ZrB₂-30 vol% SiC oxidized in stagnant air at 1500°C for times of 10 and 20 seconds using standard box furnace. Zr-O, Si-O, and B-O bonds are seen, indicating ZrO₂ and borosilicate glass on the surface.

The sample oxidized at 1500°C for 20 seconds had very similar XPS results. However, several important differences are described below. The C 1s peak no longer has a shoulder on the right for Si-C bonds, nor does the Si 2p peak have a shoulder for these bonds, indicating that SiC is no longer present on the surface after this oxidation treatment. The B 1s peak no longer has a shoulder for boride, indicating all surface ZrB_2 has also been oxidized. The O 1s peak is also smoother, though still wide enough to contain several peaks.

In summary, the XPS results indicate that the glass on the surface after 10 seconds of oxidation at 1500°C is borosilicate glass, as both Si-O and B-O bonds are seen. At 10 seconds, the surface is composed of unoxidized ZrB_2 , and SiC, as well as ZrO_2 and borosilicate glass. After a 20 second exposure, XPS shows that the entire surface is covered by oxide products, both ZrO_2 and borosilicate glass.

Viscous Flow of the Outer Oxide Layer

The oxide layer thickness versus normalized position for a specimen held at an $\sim 45^\circ$ angle at 1500°C for 100 minutes is shown in Figure 28. Measurements were taken for both the borosilicate thickness and the ZrO_2 thickness along the length of the top surface of the specimen from the high end to the low end. As is seen in all other specimens, there is a large scatter in the thicknesses of the oxide layers. It is found with 99% certainty that no correlation exists between oxide thickness and specimen position, indicating macro flow of the borosilicate glass has not occurred under these exposure conditions.

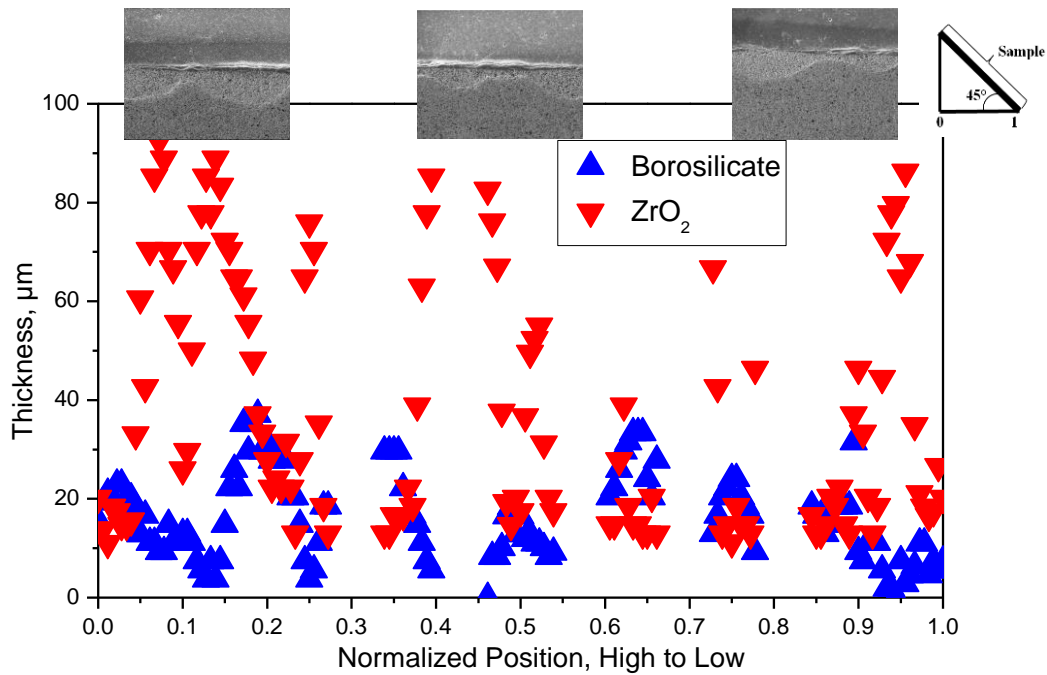


Figure 28. Oxide thickness versus position for a ZrB_2 -30 vol% SiC specimen oxidized at $\sim 45^\circ$ angle for 100 minutes at 1500°C in ambient air in standard box furnace, showing no evidence of glass flow.

Initial Surface Roughness

The oxidation mass change of materials oxidized after polishing to a $0.05\mu\text{m}$ finish were similar to those of the specimens with as-received surface finish already reported and are recorded in Table 6. Figure 29 and Figure 30 show SEM images for specimens with a $0.05\mu\text{m}$ finish after oxidation exposures of 10 and 20 seconds at 1500°C in stagnant ambient air. Figure 31 compares the oxide products formed on the as-received material and the polished material after 20 seconds of oxidation. A significant difference can be seen in the distribution of the oxide phases. After oxidizing the polished material, there was a regular distribution of the two oxidation products, ZrO_2 and borosilicate glass, though again this was seen on a scale much larger than the initial grain size. The borosilicate phase followed the initial SiC grains in some

locations, but additional large areas are seen where borosilicate glass had spread over the surface irrespective of the underlying phase. These larger pools were $13 \pm 8 \mu\text{m}$ in diameter after 10 seconds (Figure 29a) and $33 \pm 20 \mu\text{m}$ after 20 seconds (Figure 30a), however, the area fraction of the glass pools was $\sim 35\%$ on both surfaces. Thus it is reasonable to assume that these pools were thicker at 20 seconds.

The average oxide thickness after exposure at 1500°C for 100 minutes of polished ($41.3 \pm 19.8 \mu\text{m}$) and as-received ($39.6 \pm 26.4 \mu\text{m}$) was statistically insignificantly different. The specific mass gain of the polished specimens were within the standard deviation of the mass gain measured for the as-received specimens oxidized under the same conditions (Table 6). In summary, the surface finish affects short time oxide phase distribution but has no obvious effect on specific mass gain or on oxide morphology after 100 minutes.

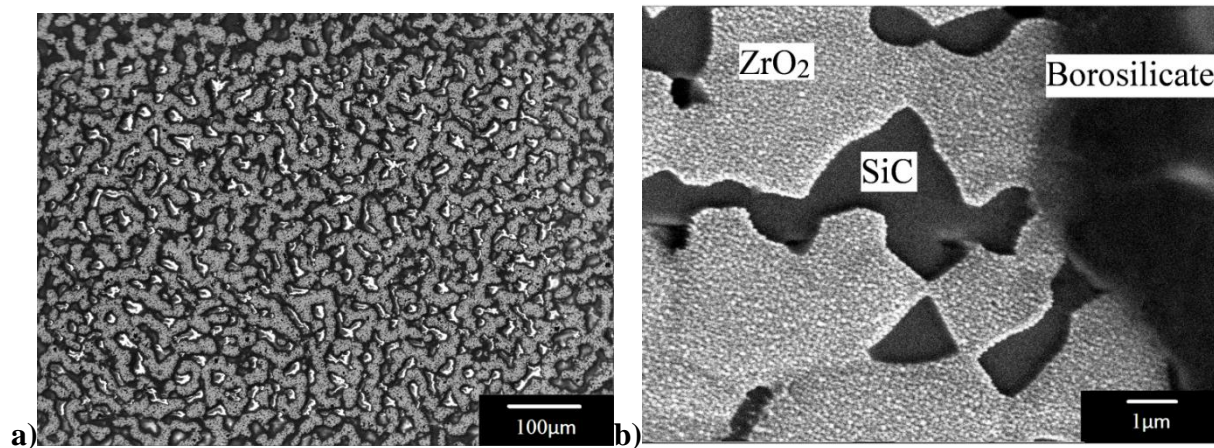


Figure 29. ZrB_2 -30 vol% SiC with $0.05 \mu\text{m}$ surface finish after 10 second exposure at 1500°C in ambient air in standard box furnace, showing the distribution of the borosilicate glass over the surface a) at intermediate magnification b) at high magnification.

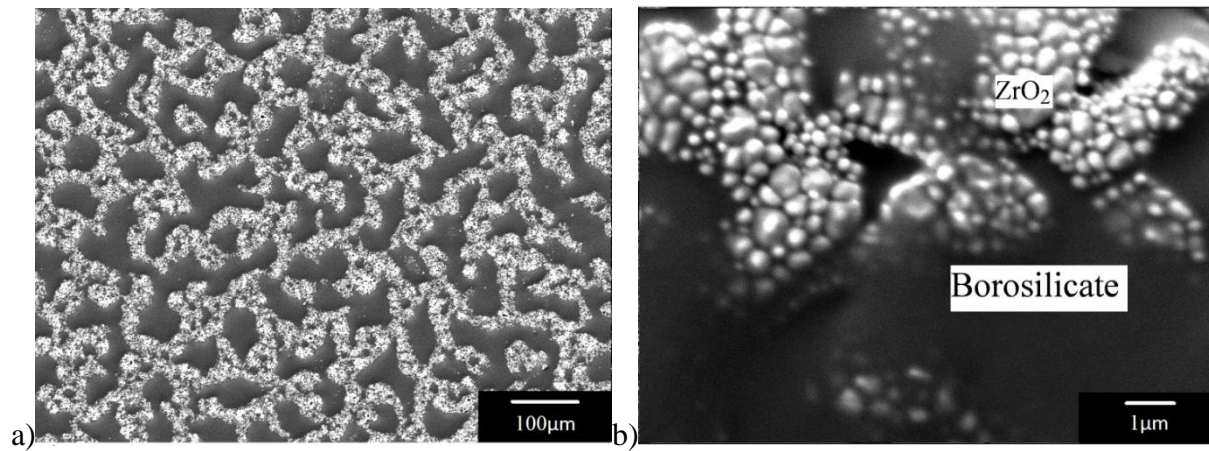


Figure 30. ZrB_2 -30 vol% SiC with a $0.05\mu\text{m}$ polished surface finish after 20 second exposure at 1500°C in ambient air in standard box furnace showing the distribution of the borosilicate glass over the surface a) at intermediate magnification b) at high magnification.

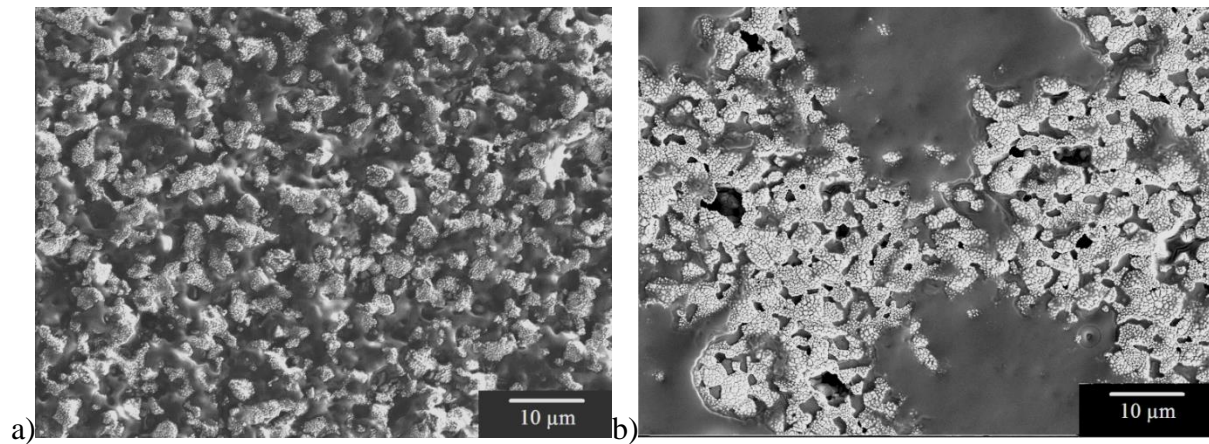


Figure 31. ZrB_2 -30 vol% SiC oxidized for 20 seconds at 1500°C in ambient air in standard box furnace using a) as-received material and b) material with a $0.05\mu\text{m}$ surface finish. Both show uneven distribution of the borosilicate glass over the surface, though the spacing is different.

Glass Pools and Bubble Formation

Observation of the specimens' surfaces after oxidation showed that 'large' pools of glass and bubbles formed on some surfaces in as little as 30 seconds at 1500°C. An example of a pool and evidence of the bubbles for the 30 second exposure condition are shown in Figure 23. These bubbles are dispersed unevenly over the specimen surface and do not appear on all specimens.

Table 8 summarizes observed bubble size and distribution after various oxidation exposures. A large fraction of specimens had no bubbles, demonstrating difficulty in preserving bubbles in post-test specimens. Characterization of specimen cross sections after oxidation in air for 10, 50, and 100 minutes at 1500°C, showed 7 to 12 scallops of differing widths and depths in the ZrO₂ layer, with examples shown in Figure 16. The specimen oxidized for 100 hours also showed 3 scallops. Since the corners of this specimen were highly oxidized, it is possible more scallops had been present earlier in the test. The bottom surfaces of all specimens showed fewer scallops.

Temperature (°C)	Time	Bubble size (μm)	Glass pool size (μm)	Additional information
1500	30 seconds	43-174	--	Bubbles covered 34% of one region (54cm ²), 0% of another region (54cm ²)
	30 seconds	--	13-50	No bubbles
	1 minute	--	61-79	No bubbles
	100 minutes	977	--	1 bubble only
	100 minutes	--	--	No bubbles
	100 minutes	--	--	No bubbles
	100 hours	10-395	--	2 bubbles evident in cross-section
1550	10 minutes	--	--	No bubbles
	50 minutes	--	--	No bubbles
	100 minutes	700	--	1 bubble only

Table 8. Observations of bubbles in the borosilicate glass phase formed during oxidation of ZrB₂-30 vol% SiC in ambient air in standard box furnace.

Discussion

Variability of Oxidation Kinetics

It is important to understand the sources of oxidation variability to accurately predict lifetimes. It is apparent from the series of 100 minute exposures that within a batch of ZrB₂-30 vol% SiC and even within one specimen bar, a large variation in oxidation behavior exists. An inverse correlation between the thickness of the ZrO₂ layer and the borosilicate layer is observed, likely due to the impact of the borosilicate layer on oxidation, as seen in Figure 17. The borosilicate glass acts as an oxygen diffusion barrier, protecting the ZrB₂-SiC, so when the glass is thicker less ZrO₂ forms, while less borosilicate allows for greater growth of ZrO₂. This correlation will be discussed in more detail when bubble formation is addressed. While some variability in oxidation kinetics between different specimens may be due to specimen preparation or variation in oxidation conditions (relative humidity, environmental impurities), the significant amounts of variability within an individual specimen cannot be explained by these mechanisms.

The specific mass gain which would occur if the maximum oxidation depth were achieved over the entire specimen when oxidized at 1500°C for 100 minutes was calculated using the data point represented by a star in Figure 17. Several assumptions were made. (1) The ZrO₂ which forms was assumed to be a fully dense layer. (2) The consumption of ZrB₂ and SiC was assumed equal to the starting mole fraction. (3) The SiO₂ was assumed to form a layer on top of the ZrO₂. (4) All of the C is assumed to form CO(g). (5) 23% of the B₂O₃ formed was assumed to be retained in the glass, whereas the remainder was assumed to vaporize. This value was based on results in which the composition of the glass formed on a ZrB₂-30 vol% SiC specimen during oxidation in air at 1500°C for 100 minutes was determined using Inductively Coupled Plasma Optical Emission Spectrometry (ICP-OES), which will be presented in Chapter

6. Using these five assumptions, the mass gain due to oxygen incorporation in condensed oxide phases and the B and C mass loss due to $B_2O_3(g)$ and $CO(g)$ vaporization was calculated per Zr atom oxidized. The number of moles of Zr in the oxidized volume ($96.5\mu m \times 1cm \times 1cm$) was calculated to be 4.4×10^{-4} . This leads to an estimated maximum specific mass gain of $14.3mg/cm^2$ for 100 minute oxidation at $1500^\circ C$, shown by the star in Figure 18. This predicted mass gain is almost as high as the mass gain after 24 hours at $1500^\circ C$ and will be discussed below.

Included in Table 4 are literature results for mass gain during oxidation for ZrB_2-SiC , and measured k_p . Most studies do not include sufficient quantitative results from the oxidation tests, making comparison between studies difficult; however, as seen in Table 4 the rate constants measured here for oxidation between $1300^\circ C$ and $1550^\circ C$ are of the same order of magnitude as those in the literature, indicating the results obtained in this study are not atypical.

The 24 hour and 100 hour oxidation mass gains were compared to predictions from tests conducted for times ≤ 4 hours in Figure 18. The experimental mass gains of the 24 hour and 100 hour specimens were both greater than the upper 95% confidence interval on k_p , indicating that use of short term oxidation tests (the literature focuses on 10 minutes to 4 hours) is insufficient for prediction of long term results. It is possible that the difference between long duration mass gain and that predicted by shorter term tests indicates a change in mechanism. However, the morphology of the microstructure (grain shape, oxide distribution, presence of scallops) appears to remain the same after long and short term tests (Figure 32.) The 24 hour and 100 hour specimen mass gains both fall between the rate predicted by the maximum oxidation depth calculated above (star data point) and the upper 95% confidence interval calculated from mass change in oxidation exposures <4 hours. These results reinforce the need to consider maximum oxidation depth for life prediction modeling of ZrB_2-SiC .

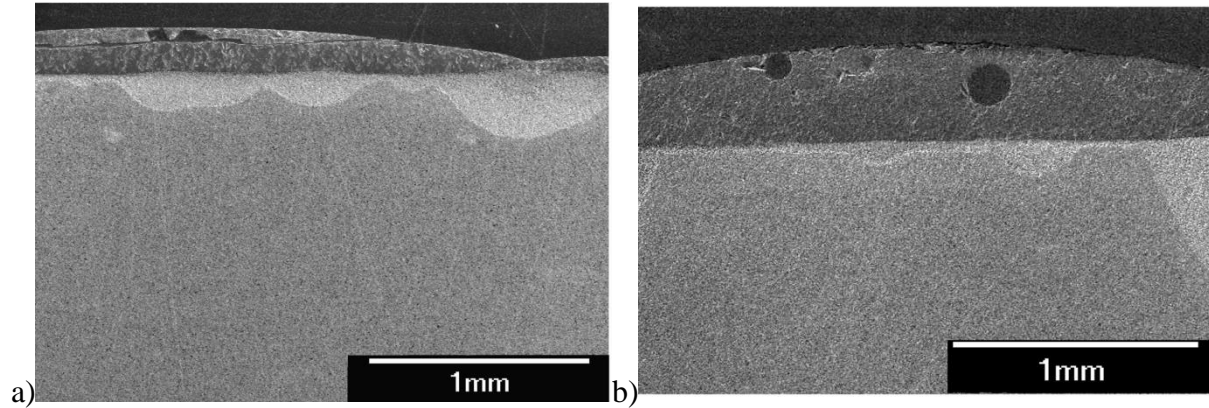


Figure 32. ZrB_2 -30 vol% SiC oxide morphology after oxidation at 1500°C for a) 24 hours b) 100 hours, showing similar morphology to samples oxidized for >4 hours, with both ZrO_2 scallops and bubbles in the borosilicate present.

Initial Stage Oxidation

Short-term oxidation tests were conducted to try to understand the origin of inhomogeneities in oxide morphology observed at long times. These tests showed that even at 10 seconds significant oxidation had already begun on the surface of the specimen. Extrapolating from linear oxidation rate constants found in the literature for pure SiC, in 10 seconds at 1500°C in air only 1.5nm thickness of silica is predicted^{56, 75}. The SEM images clearly show that a much thicker borosilicate layer had formed in some areas of the specimen. The B_2O_3 , which formed upon oxidation of the ZrB_2 grains likely reacted with the native SiO_2 on the SiC to form non-protective borosilicate glass. Due to the very large volumetric expansion during the oxidation of SiC to SiO_2 (118%) and the smaller expansion due to oxidation of ZrB_2 to ZrO_2 (17%), the borosilicate glass flowed over the surrounding ZrO_2 surface. Uneven spreading of the glass during short times (<20 seconds) may lead to regions where bubble formation is more likely to occur, although a continuous borosilicate layer had formed on the specimen surface in as little as 30 seconds.

ZrO₂ grain growth over time was observed. Larger grains are observed under borosilicate bubbles which have burst (Figure 23c) and in cross sections of specimens oxidized for longer times. The apparent ZrO₂ grain size in plan view is difficult to interpret accurately due to uneven coverage of the borosilicate glass, so that the ZrO₂ grains appeared to be smaller at 10 minutes than at shorter times. Karlsdottir and Halloran have suggested that “convection cells” operate in the oxide scale, allowing the borosilicate liquid to move from the base material/oxide interface, towards the surface where B₂O₃ volatilizes, decreasing the B content of the glass. When this happens, they propose that the solubility of ZrO₂ in the glass is lowered and ZrO₂ “flowers” precipitate out, explaining their presence on the surface of the oxide^{23, 44, 76}. It is uncertain whether the ZrO₂ observed in the current study on the surface after 10 and 50 minutes are the result of such convection flow or remain from the initial ZrO₂ island formation. It is also possible that the ZrO₂ grains formed upon cooling, as the solubility of ZrO₂ in the borosilicate glass decreases rapidly with temperature⁷⁷.

Viscous Flow of the Outer Oxide Layer

From the results of the specimen oxidized at an ~45° angle, it can be seen that no measureable macroscopic flow of the borosilicate glass occurred along the surface at 1500°C. Surface tension must prevail over gravity in determining the flow of the borosilicate glass and viscous flow on a macro scale is not responsible for variable oxidation kinetics at 1500°C. It should be noted, however, that viscosity of the glass will decrease with increasing temperature and that viscous flow may influence the oxidation behavior at temperatures above 1500°C³².

Initial Surface Roughness

The continued inhomogeneous distribution of oxide products on the surface of polished specimens indicates that roughness is not the overriding cause of variability, though a smoother surface appears to allow for easier spreading of the borosilicate glass at short times. On the rougher specimens, the borosilicate glass appeared to fill in “valleys” on the surface before fully covering the surface. The specimens polished prior to oxidation showed larger pools, presumably since there are no “valleys” to fill. However, after 30 seconds, both surface preparations showed full coverage, as more borosilicate glass forms than can fill low-lying areas. It is important to note that the 100 minute oxidation mass gain results showed no statistical difference for as-received and polished surfaces, confirming that surface roughness is not the primary mechanism for oxidation variability

Humidity

Wet atmospheres increase the oxidation kinetics of SiC. The solubility of H_2O in SiO_2 is greater than that of O_2 , increasing the k_p ⁵⁵. In addition, H_2O may bring impurities to the surface, also increasing k_p , through opening of the SiO_2 network resulting in less protective silicate scales^{78, 79}. Kuriakose and Margrave found that during oxidation of ZrB_2 at 1056°C the presence of water vapor in the flowing oxygen had no impact⁴¹. Work by Brown, on the other hand, showed an increase in mass gain for ZrB_2 from 27 to 42% when changing from dry to untreated air at 650°C , showing a strong impact of moisture at lower temperatures⁴². Nguyen et al. report that 90% water/10% air low velocity vapor does not have a significant impact on oxidation behavior of ZrB_2 -SiC in comparison to stagnant air oxidation when oxidized between 1200°C and 1400°C ⁸⁰. While both B_2O_3 and SiO_2 are known to be unstable in the presence of water, and therefore high humidity could impact the overall mass change results in this work, it seems unlikely that it

could impact the thickness of the developed oxide differently in different regions of the same specimen, and therefore cannot explain the large variations in oxidation behavior ⁸¹.

Glass Pools and Bubble Formation

Bubbles formed in the continuous glass layer in 30 seconds for specimens oxidized at 1500°C in stagnant air, much quicker than the 350 minutes reported by Gangireddy et al. ³⁶.

Bubble formation due to generation of gaseous oxidation products was assumed as the most likely source of oxidation variability, based off the microstructure and oxide products discussed in the literature ^{19, 22, 26, 36}. Formation of bubbles in the glassy phase could be due to CO(g) formed during SiC oxidation (Reaction 1.3) or B₂O₃(g) volatilizing due to its high vapor pressure (Reaction 1.2) according to the literature. However, as the borosilicate glass is below its boiling temperature when oxidized at 1500°C, B₂O₃(g) is neglected as a source of bubble formation.

FactSage was used to calculate the partial pressures of the gasses that form upon oxidation of ZrB₂-SiC at 1500°C. The equilibrium constant for Reaction 1.1, determined using the Reaction module is 2.022x10³⁹. Using:

$$K_{eq} = \frac{a_{ZrO_2} a_{B_2O_3(l)}}{a_{ZrB_2} P_{O_2}^{5/2}} \quad [4.1]$$

and assuming that the activity of all solids and liquids is unity, the equilibrium partial pressure of oxygen at the ZrB₂/ZrO₂ interface was calculated to be 1.9x10⁻¹⁶atm. Using the Equilibrium module, inputting ZrB₂-SiC, and holding the activity of oxygen at the equilibrium value of P_{O₂}, the partial pressure of other gasses formed were calculated. The three dominant gas partial pressures were as follows: P_{CO}= 9.97x10⁻¹atm, P_{CO₂}= 9.07x10⁻⁵atm and P_{SiO}= 3.25x10⁻³atm. At 1500°C, B₂O₃(g) has a partial pressure of 2.6x10⁻³atm, independent of P_{O₂}. CO(g) has the highest partial pressure and with a partial pressure of almost 1atm, it is reasonable that CO(g) will form bubbles in the borosilicate glass. It must be noted that rigorous microscopy has shown that not all

of the C oxidizes at temperatures below 1627°C, as will be discussed in Chapter 5. This means that another species besides CO(g) may be responsible for the bubble formation.

Figure 33 illustrates a mechanism by which oxidation behavior (both ZrO₂ oxidation depth and thus mass gain) is affected by bubble formation in the borosilicate glass. In this mechanism, borosilicate glass covers the surface after 30 seconds, at which point bubbles begin to form, due to trapped gasses. When bubbles burst, exposing underlying material, increased oxidation is allowed in the region. The mechanism presented in Figure 33 is consistent with observations of Gangireddy et al.³⁶ for ZrB₂-15 vol% SiC material oxidized between 1450° and 1650°C and Carney et al. for ZrB₂-20 vol% SiC material oxidized for 150 minutes at 1600°C³². The formation and bursting of bubbles was attributed there to the pressure of the gaseous products and viscosity of the glass layer. The data reported in Figure 17 support the proposed mechanism. When the borosilicate layer is thick, underlying layers of ZrO₂ are thin, due to greater oxidation resistance provided by the silica-rich glass. When the borosilicate layer is thin, the region shows a large range of ZrO₂ layers thicknesses. This large distribution of ZrO₂ thicknesses with thin glass layers suggest bubble generation and rupture over a range of oxidation times.

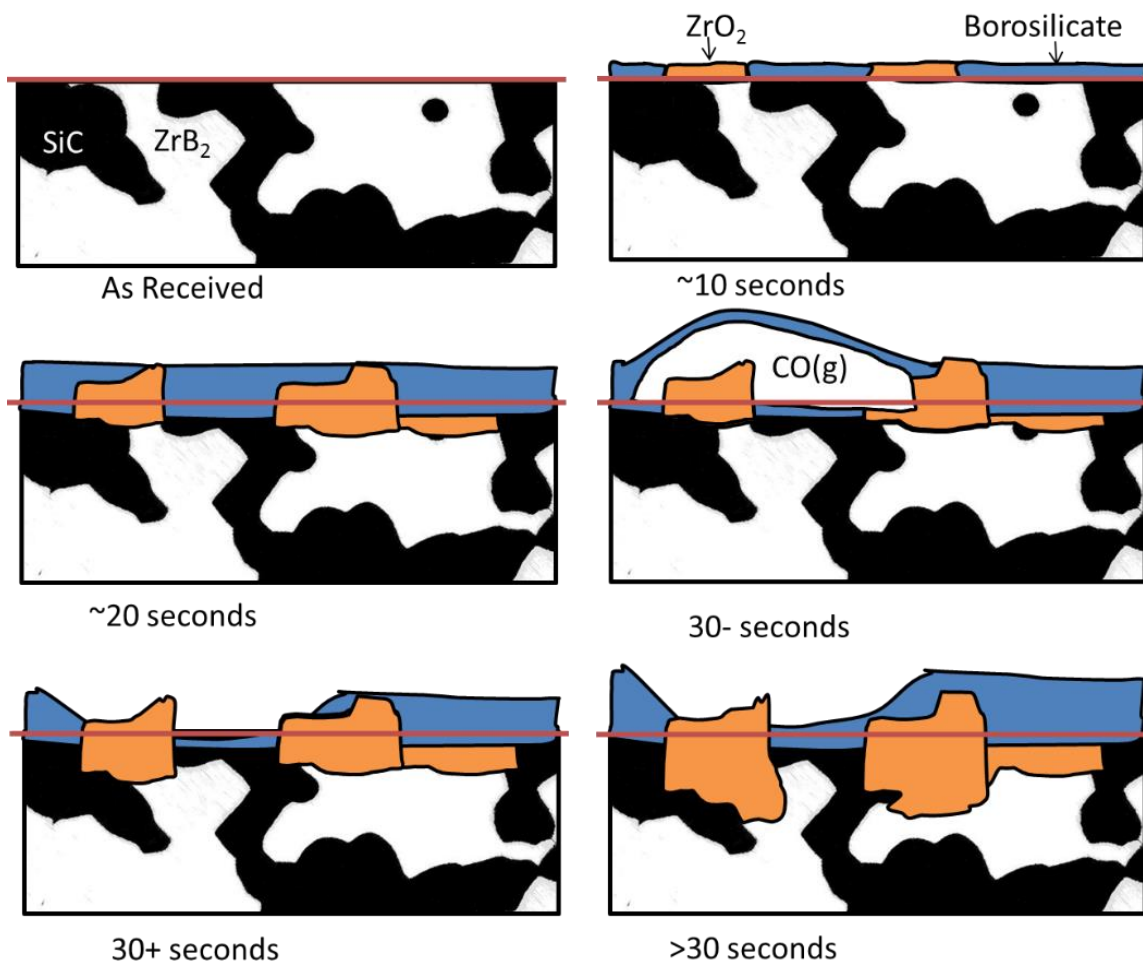


Figure 33. Proposed mechanism for ZrB₂-30 vol% SiC oxidation variability due to the formation and bursting of bubbles in the borosilicate glass.

Limitations

Limitations to this study and the proposed mechanism include the following. This study was conducted on bars cut from a series of hot pressed billets; variations due to processing differences were not identified. However, the variation in results observed herein are similar to those reported in the literature^{11, 43, 45, 80}. Viscous flow of the glass phase is likely to be more important as gas velocities and temperatures rise. Different volume fractions of SiC will result in more or less silica-rich scales, potentially affecting oxidation results. Bubbles were not observed in the glass phase of all specimens (Table 8), however, previous work by Gangireddy et al. has shown the time between formation and bursting is one minute, making them difficult to preserve in post-test specimens³⁶. Further study of bubble formation is required to confirm this proposed mechanism for a wider range of materials and oxidation conditions. The continued presence of C between the ZrO₂ grains as discussed in Chapter 5, instead of the borosilicate glass reported in the literature^{19, 22, 26, 27}, must also be reconciled with this mechanism.

Conclusions

A statistical analysis of ZrB₂-30 vol% SiC oxidation under well-defined/controlled conditions has been performed. ZrB₂-30 vol% SiC showed variable oxidation kinetics. Variable oxide thickness and oxide phase distribution formed on the surface of the specimen likely explains scatter in measured mass change among different specimens. The specific mass gain in air at temperatures between 1300° and 1550°C and exposure times between 30 seconds and 100 minutes varied up to a factor of 2.4, even when well-controlled testing parameters are used. The oxide thickness formed on any one specimen showed variations in thickness up to 80% of the average thickness. This work shows that using the average value for mass gains obtained for times of 4 hours and less to determine a 95% confidence interval on the parabolic oxidation rate constant is not sufficient for predicting material recession due to oxidation at longer times. First, there are regions where the depth of attack is much greater than average and, second, short-term oxidation tests are not good predictors for long-term tests. Consideration of a maximum attack rate is needed to conservatively determine the capability of this material to maintain sufficient load-bearing cross-section during exposures to ultra-high temperature oxidizing environments.

Viscous glass flow and surface roughness have been eliminated as primary causes for the observed variability in oxidation kinetics at 1500°C. Regardless of surface roughness, the uneven distribution of the borosilicate glass formed within the first 30 seconds of oxidation results in localized bubble formation. The borosilicate glass slows oxygen diffusion in areas where it is present. When glass bubbles burst leaving areas with thin or no borosilicate coverage increased oxidation rates occur locally, further increasing inhomogeneity in the oxide scale with resulting variability in long-term oxidation kinetics.

Recommendations for Future Work

1. A systematic in-situ study of bubble formation as a function of SiC content, temperature and time would verify the proposed mechanism for oxidation variability. This verification would also require an analysis of the percentage of C that remains between the ZrO_2 grains.
2. Increased mass gain was observed at 1400°C in comparison to 1300°C and 1500°C, but was not studied in great detail. This anomaly may be due to the different temperature dependencies of oxide formation and volatility. A detailed determination of the temperature dependence of oxidation and volatility is needed to elucidate the observed maximum in the oxidation rate at 1400°C.
3. This study only considered the viscous flow of the borosilicate glass at 1500°C due to the maximum temperature capability of the box furnace. However, application of this material could involve higher temperatures and almost certainly high gas velocities. A study of the viscous flow as a function of temperature and gas velocity is important before this material could be put in use.

Chapter 5 Task 2- Oxide Morphology

Objective

The objective of this task was to provide a more thorough understanding of the two oxidation regimes observed (low temperature oxidation below 1627°C and high temperature oxidation at and above 1627°C.) It also aimed to establish the necessary conditions to form SiC depletion during oxidation of ZrB₂-30 vol% SiC. Thermodynamic and kinetic explanations for the transition to SiC depletion and the growth of SiC depletion were sought.

Results

Oxide Growth Kinetics

Oxidation kinetics for ZrB₂-SiC are often determined using mass gain/surface area versus time, as was done in Chapter 4^{20, 24}. For specimens oxidized using resistive heating, kinetics cannot be determined using mass change, as the entire specimen was not at temperature throughout the test. In addition, the borosilicate oxide layer has inconsistent thickness due to severe bubbling as oxidation temperature increased above 1627°C. Therefore, oxidation growth kinetics for tests performed in the resistive heating system were determined using ZrO₂ oxide thickness measurements. Results are given in Table 9 and compared to box furnace results. A comparison to literature values can be found in Chapter 4. While large variation is seen for the ZrO₂ growth rates at all temperatures leading to some uncertainty in the reported parabolic growth rate constants (as represented by the low R² values for fit to the data), a distinct jump in the k_p calculated for oxides grown at temperatures of 1650°C and above is observed compared to oxides grown at temperatures of 1500°C and below. This change in k_p corresponds to observed changes in the microstructure, as discussed below. Figure 34 displays log(k_p) versus inverse time, clearly showing the change in activation energy between oxidation regimes.

Temperature (°C)	Mass gain k_p ($\text{mg}^2/\text{cm}^4\text{h}$)	ZrO ₂ growth k_p ($\mu\text{m}^2/\text{h}$)	R ² for ZrO ₂ growth k_p fit line
1300	4.0	295	0.91
1400	7.4	280	0.61
1500	4.4	390	0.94
1650		8,500	0.21
1700		28,000	0.21
1800		42,000	0.52

Table 9. Experimental results for oxidation kinetics of ZrB₂-30 vol% SiC. Note the large R² values due to scatter in the data.

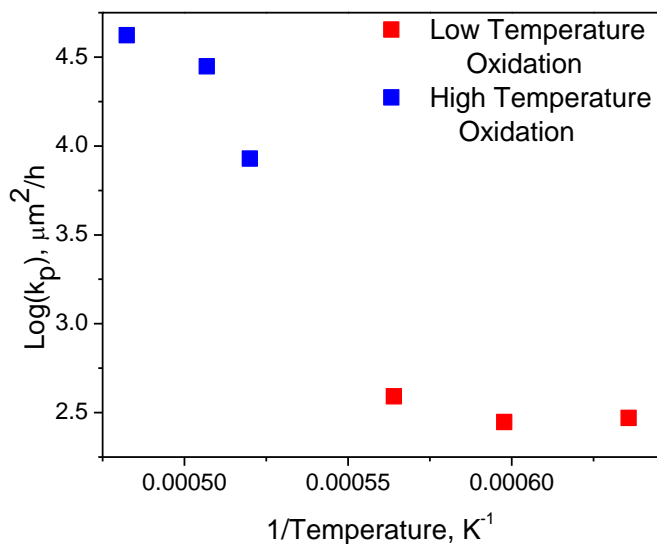


Figure 34. $\text{Log}(k_p)$ vs $1/T$ for ZrO₂ layer growth showing clear change in activation energy between oxidation regimes. This is explained by increased CO(g) production at temperatures $\geq 1627^\circ\text{C}$.

Oxide Morphology Regime I: Temperatures <1627°C

At temperatures below 1627°C, specimens showed two distinct layers after oxidation. The top layer was borosilicate glass with an underlying layer consisting of spherical ZrO₂ grains +C, as shown schematically in Figure 35a, Figure 36, and Figure 37. At early times in the oxidation such as 1500°C for 20 minutes, both SiC and C grains were interspersed between the ZrO₂ grains as in Figure 36. It is important to note that the observed ZrO₂+C oxidation products is not an artifact of resistive heating. The oxides observed for both box furnace and resistive heating at 1500°C for 20 minutes show the presence of C. However, as time and/or temperature was increased, minimal Si remained between the ZrO₂ grains, though large amounts of C were present, as in Figure 37 for an exposure at 1600°C for 55 minutes. It is also important to note that no porous layer forms in the ZrB₂ base material at oxidation temperatures below 1627°C for ZrB₂-30 vol% SiC.

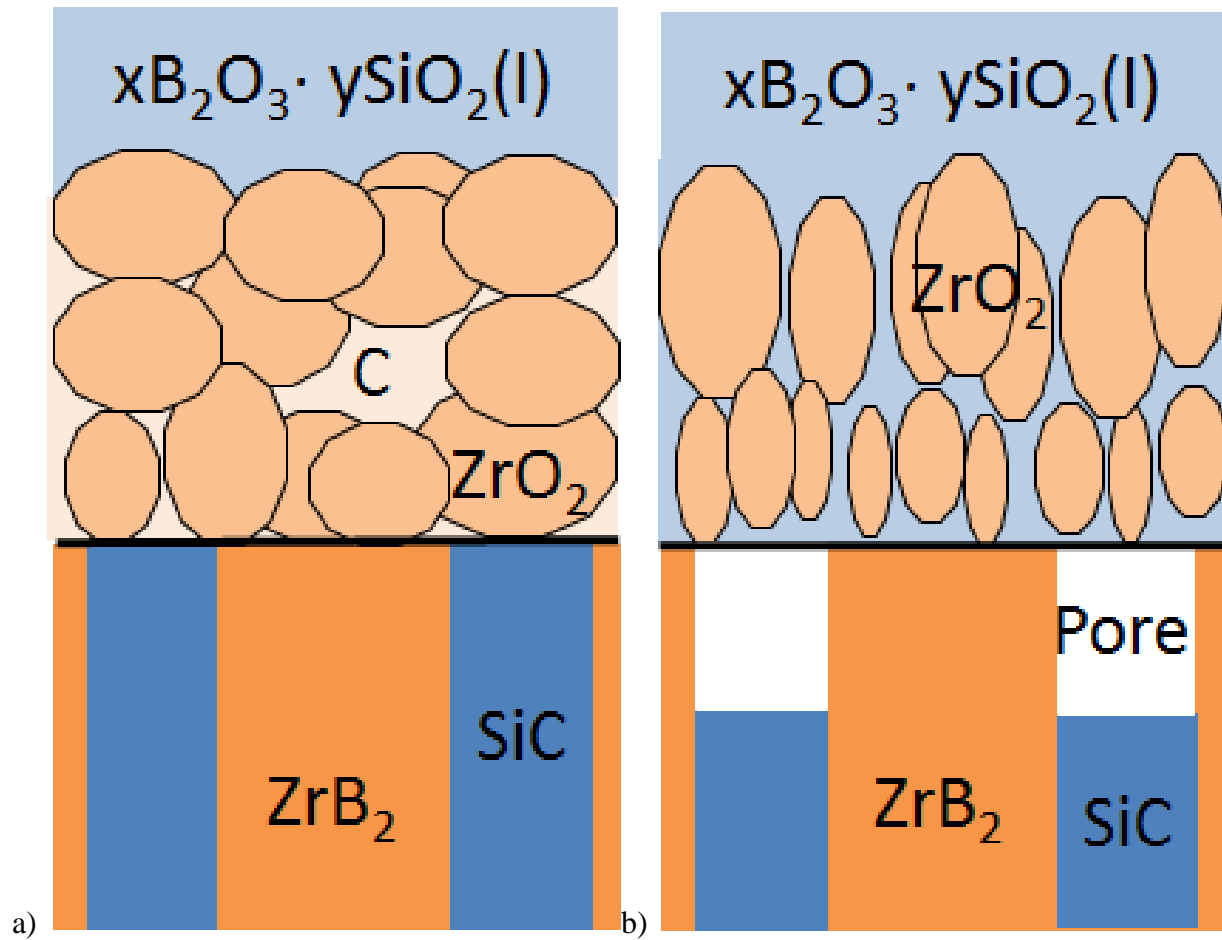


Figure 35. Standard morphology of oxide scales on ZrB_2 - SiC oxidized at temperatures a) below 1627°C, showing two layers of oxidation products b) above 1627°C, showing three layers of oxidation products.

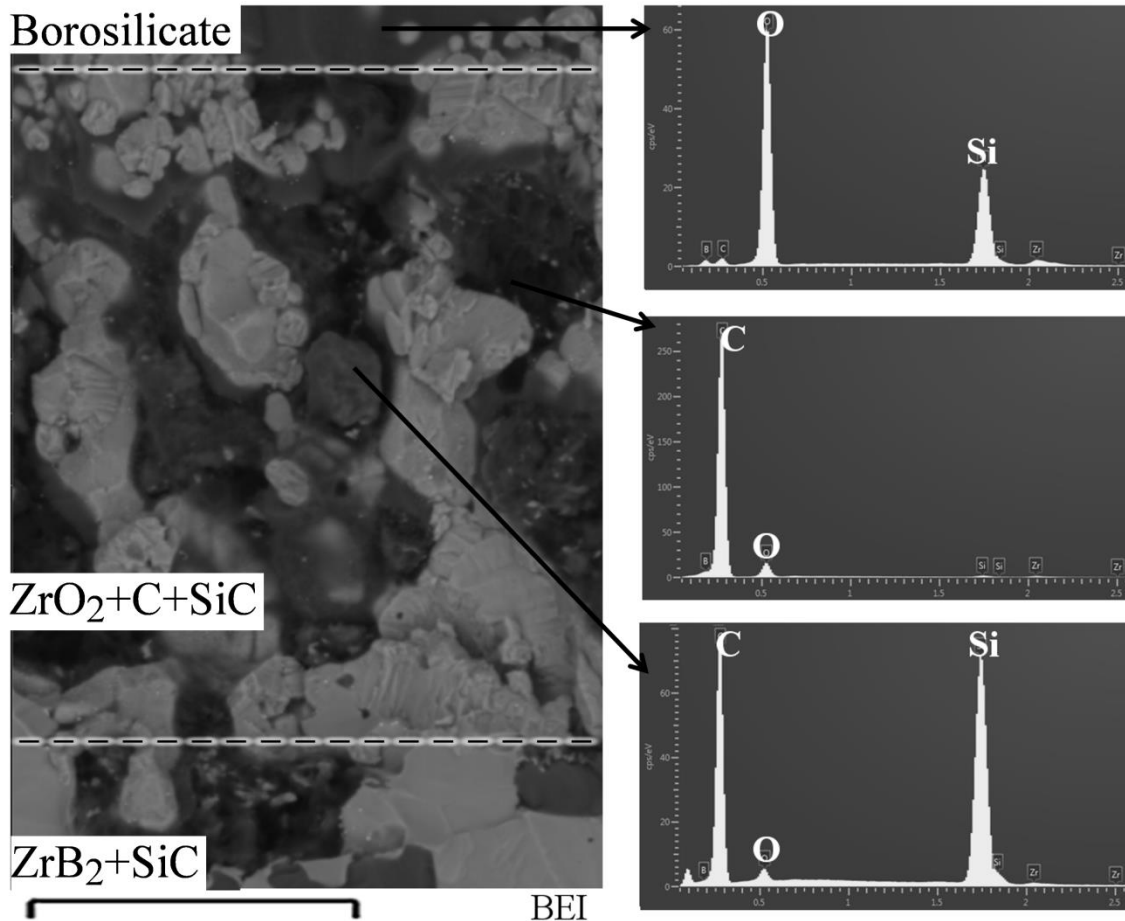


Figure 36. EDS indicating the presence of both C and SiC particles in the ZrO₂ layer of a ZrB₂-30 vol% SiC fracture section after oxidation at 1500°C for 20 minutes in flowing O₂ using resistive heating. Scale marker indicates 5μm.

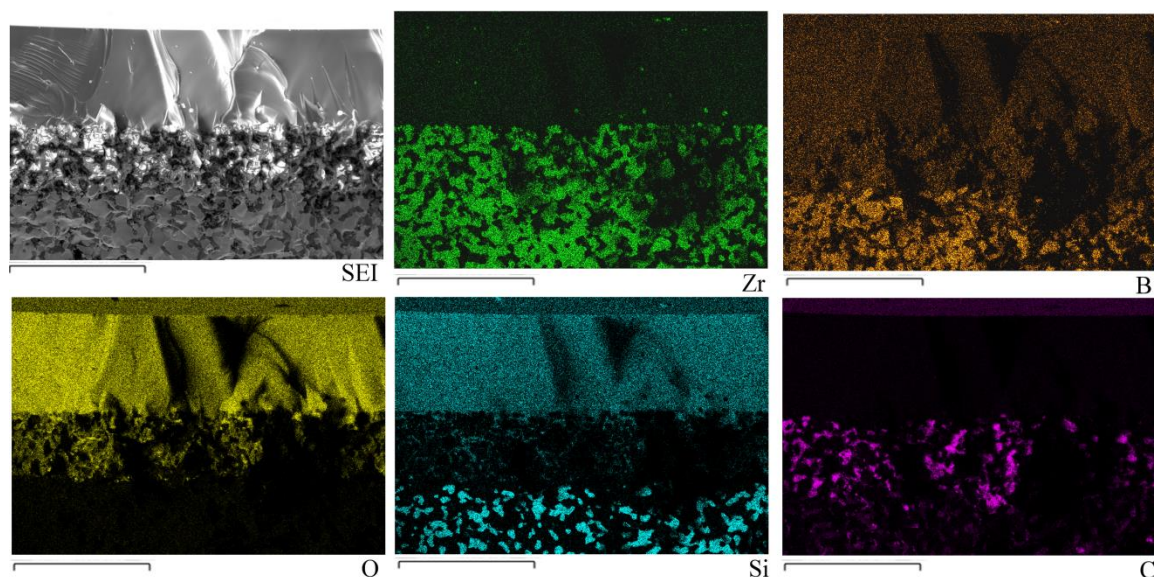


Figure 37. SE image and EDS maps of ZrB₂-30 vol% SiC fracture section after oxidation at 1600°C for 55 minutes in flowing O₂ using resistive heating. C between ZrO₂ grains is clear. Scale markers indicate 10μm.

Oxide Morphology Regime II: Temperatures $\geq 1627^{\circ}\text{C}$

At temperatures of 1627°C and above, specimens showed three distinct layers after oxidation. A top layer of borosilicate glass was observed over a middle layer consisting of columnar ZrO₂ grains filled in with borosilicate glass. Beneath these two layers was a third layer which consisted of ZrB₂ grains and porosity resulting from SiC depletion, Figure 35b. Figure 38 is an EDS map of a specimen oxidized at 1650°C for 50 minutes, which clearly shows a region containing only Zr and B, with no Si or C signal, beneath the O containing layers. Figure 39 provides a closer look at the ZrO₂/ZrB₂ interface for the same specimen.

The necessary time-temperature conditions for SiC depletion to occur in ZrB₂-30 vol% SiC have been mapped in Figure 40. For temperatures below ~1627°C, no SiC depletion formed regardless of the time of oxidation. Maximum exposure times were 100 hours and 55 minutes at 1500°C and 1600°C respectively. As the temperature increased, partial depletion was observed where some SiC grains were partially consumed (Figure 41). After 10 minutes of oxidation at

1650°C, C grains are seen between the ZrO₂ grains (Figure 42.) As time is increased to 20 minutes at 1650°C there are indications that C grains depleted in Si and SiC depletion co-existed, as seen in Figure 43. This is the only set of conditions tested that showed both types of SiC oxidation and captures the microstructural dependence of the transition temperature, as will be discussed below. At longer times and higher temperatures, only SiC depletion is seen. The 1650°C 10 and 20 minute oxidation specimens capture the time dependence of the transition between oxidation regimes. The incubation time for complete depletion of SiC to form porosity within a layer decreased with increasing temperature.

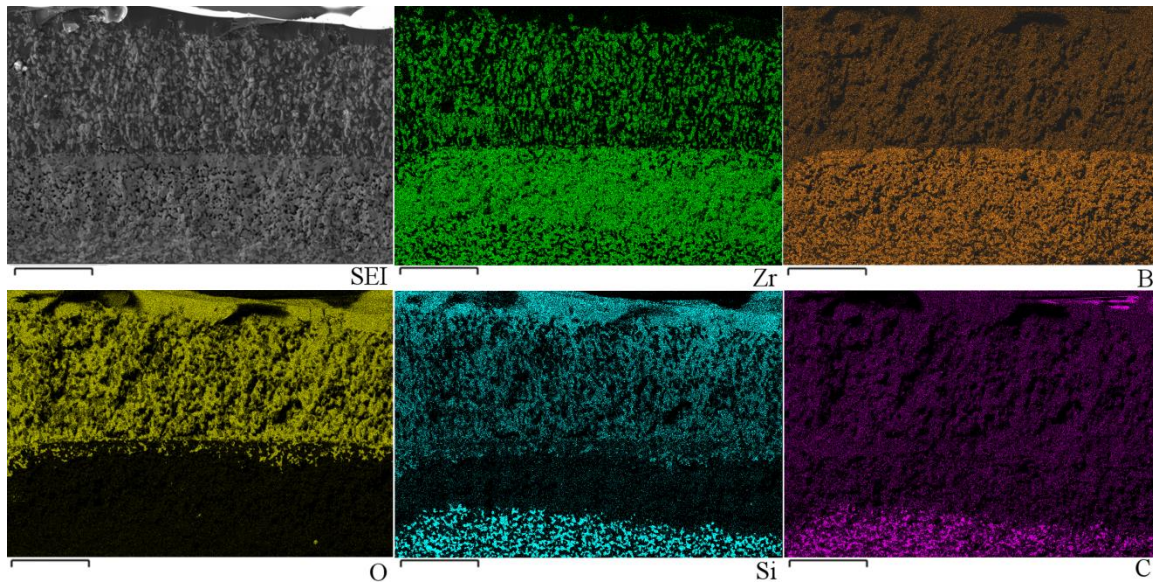


Figure 38. SE image and EDS maps of ZrB₂-30 vol% SiC fracture section after oxidation at 1650°C for 50 minutes in flowing O₂ using resistive heating. SiC depletion under ZrO₂ and borosilicate layers is clear. Scale marker indicates 50μm.

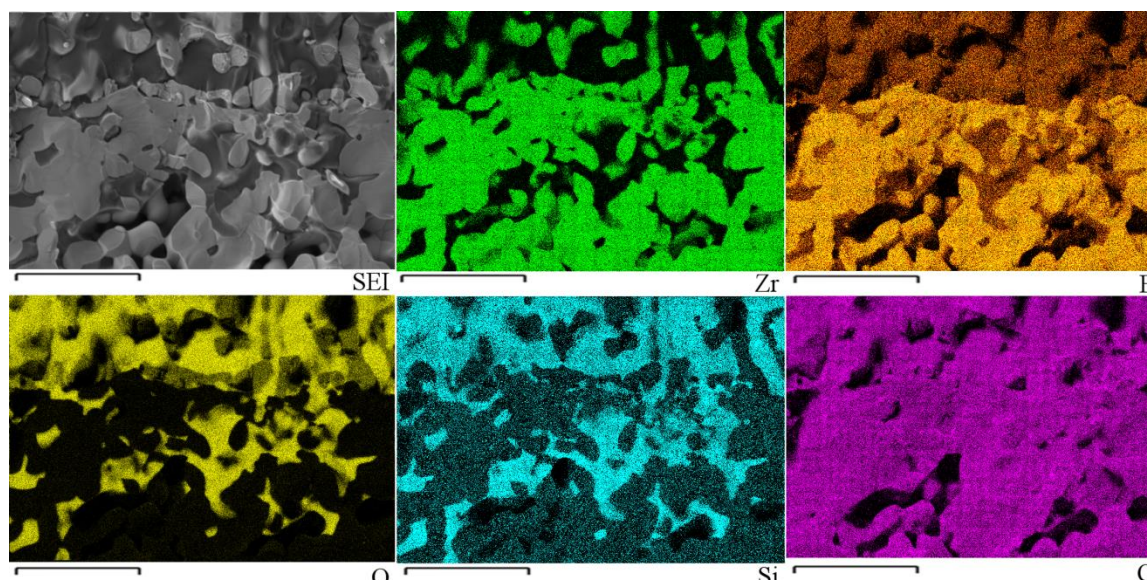


Figure 39. SE image and EDS maps of ZrB₂-30 vol% SiC fracture section after oxidation at 1650°C for 50 minutes in flowing O₂ using resistive heating showing borosilicate glass beneath the ZrO₂/ZrB₂ interface. Scale marker indicates 10μm.

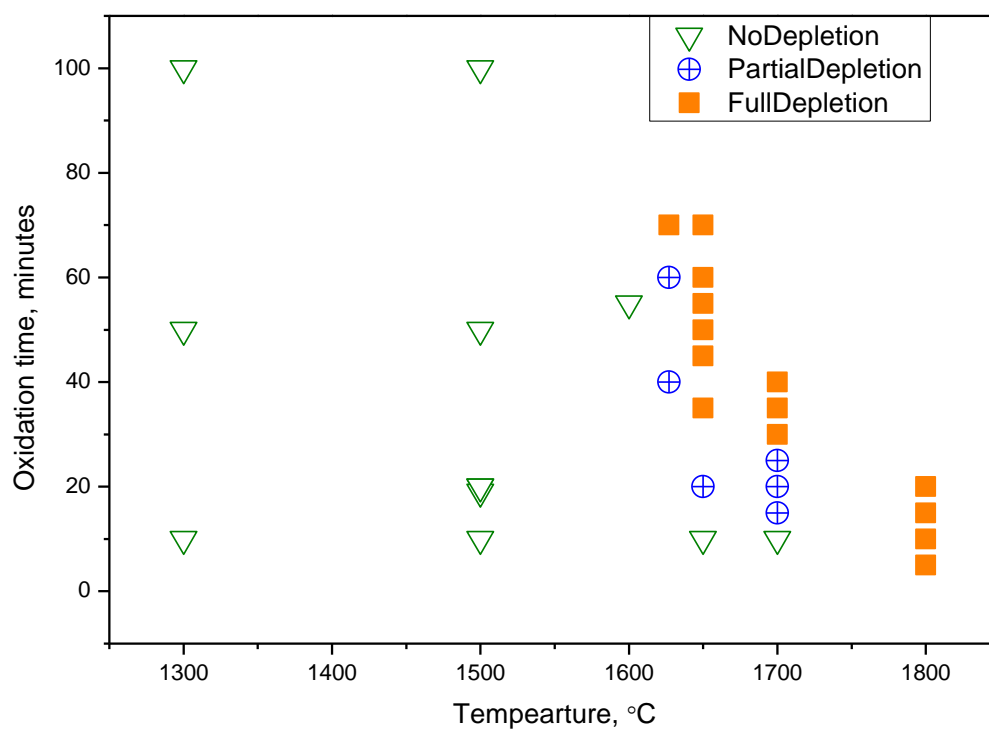


Figure 40. Oxidation conditions for SiC depletion in ZrB₂-30 vol% SiC. All exposures T≤1550°C were conducted in stagnant air. All exposures T>1550°C were conducted in 900sccm flowing O₂.

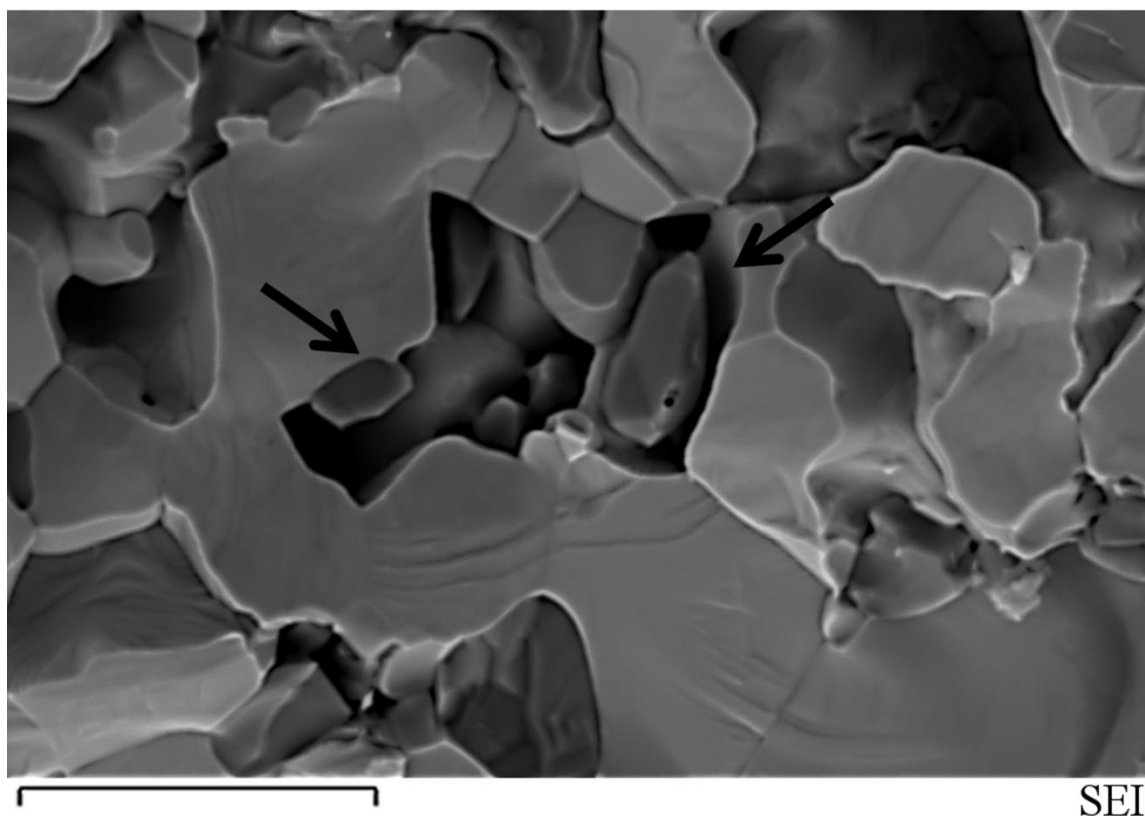


Figure 41. Fracture section of ZrB_2 -30 vol% SiC oxidized at 1650°C for 45 minutes in flowing O_2 using resistive heating system showing partially removed SiC grains (arrows) surrounded by ZrB_2 grains, in the SiC depletion layer (base material is below the imaged region.) This indicates SiC depletion forms due to active oxidation of SiC to $\text{SiO}(\text{g})$ and $\text{CO}(\text{g})$. Scale marker indicates $4\mu\text{m}$.

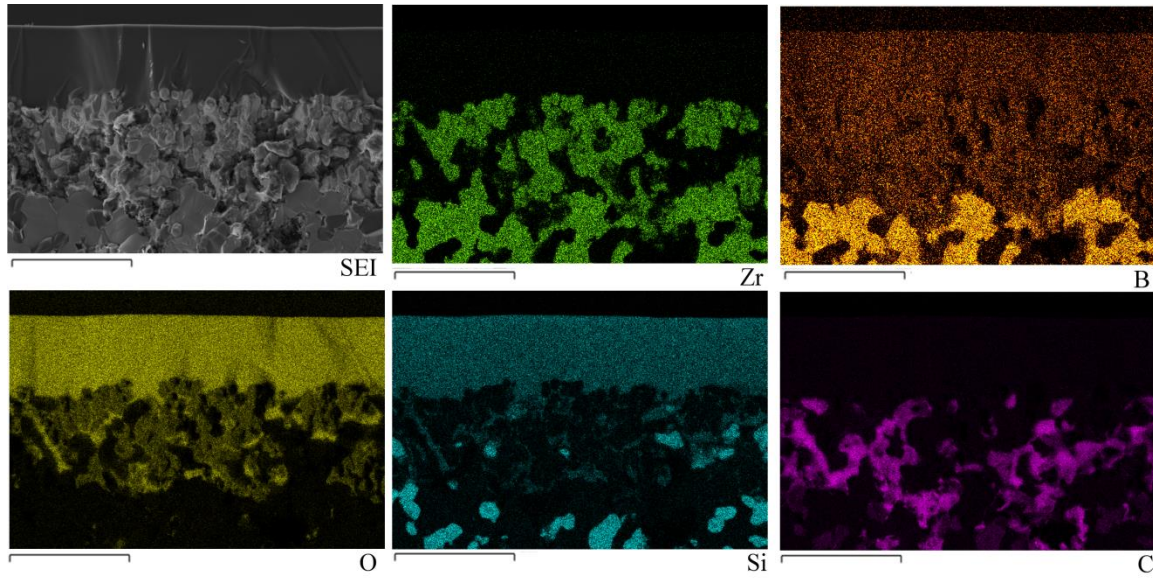


Figure 42. SE image and EDS maps of ZrB_2 -30 vol% SiC fracture section after oxidation at 1650°C for 10 minutes in flowing O_2 using resistive heating. C is seen between ZrO_2 grains and SiC depletion has not begun. This indicates a time dependence to the transition between oxidation regimes. Scale marker indicates $10\mu\text{m}$.

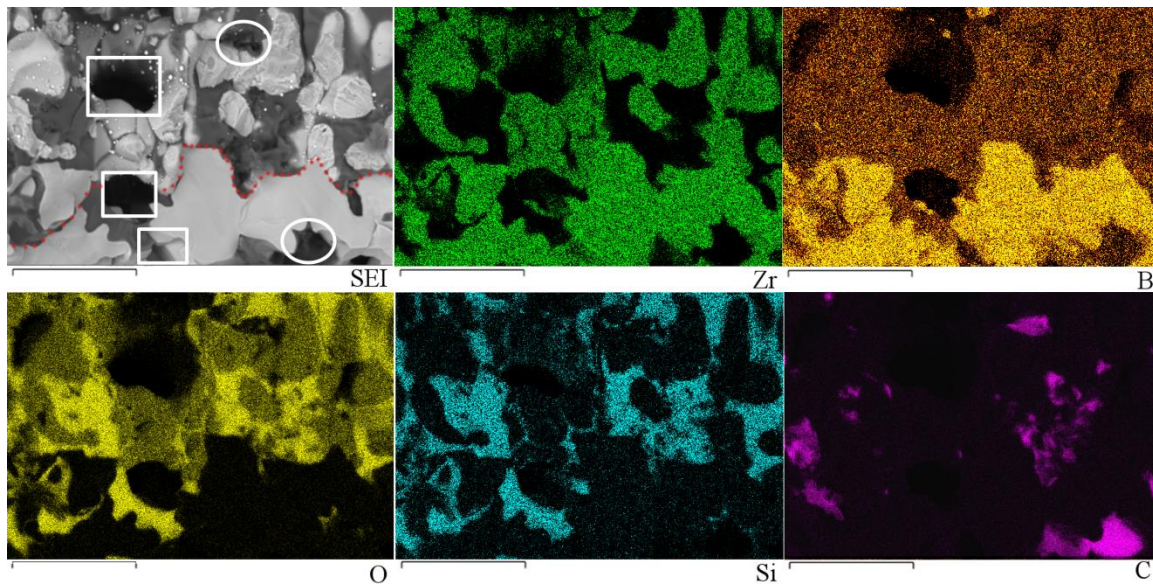


Figure 43. High magnification SE image and EDS maps of ZrB_2 -30 vol% SiC fracture section after oxidation at 1650°C for 20 minutes in flowing O_2 using resistive heating. Squares mark pores left by SiC depletion. Circles mark C remaining after oxidation of Si. Red dotted line marks boundary between ZrO_2 and ZrB_2 . This supports a time and microstructural dependence to the transition between oxidation regimes. Scale marker indicates $5\mu\text{m}$.

SiC Depletion Growth Kinetics

Figure 44 shows cross-sectional views of specimens oxidized at 1800°C for increasing times of 5, 15 and 20 minutes. The growth of the SiC depletion layer with time is clear. Figure 45 plots the depletion layer thickness versus oxidation time for all tests. The depletion layer clearly grew over time at the depletion layer/base material interface. Due to the significant scatter in the time dependence for depletion layer growth a clear rate law is not obvious. The depletion layer growth was therefore fit to both linear and parabolic rate laws to examine the temperature dependence. The parabolic rates, k_l and k_p , were determined by plotting the thickness of the depletion layer in μm versus minutes (linear) or minutes^{1/2} (parabolic.) These results are shown in Figure 46, where it is clear minimal temperature dependence is observed regardless of assumed rate law. The 1627°C tests were not included in the k_p plot due to insufficient data. The top of the depletion layer occasionally shows some SiO₂ below the ZrO₂/depletion layer interface, indicating that oxidation of the SiO(g) to SiO₂ occurs near the ZrO₂/ZrB₂ interface (Figure 39, Reaction 2.1.)

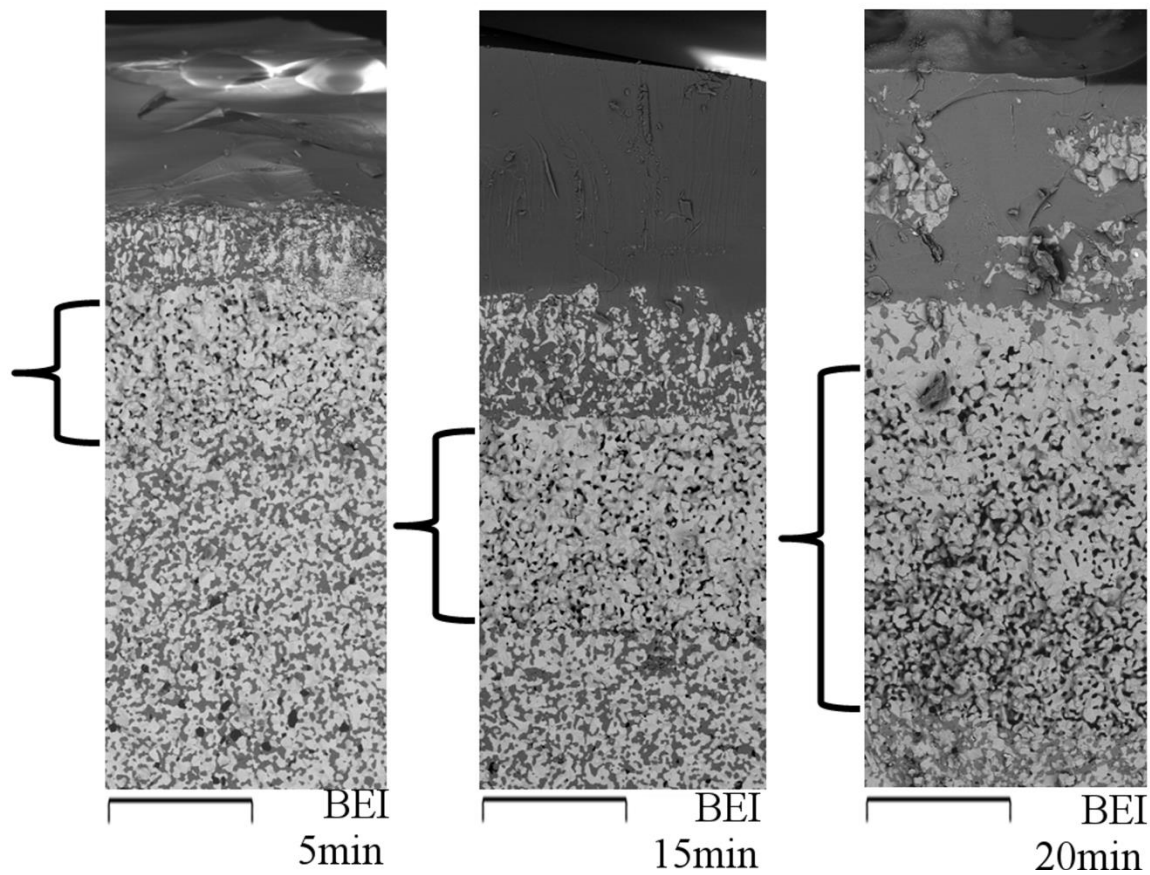


Figure 44. ZrB_2 -30 vol% SiC oxidized at 1800°C for a series of times (5-20 minutes), showing growth of the SiC depletion layer. The bracket highlights the porous layer. 5 minutes has $43\pm 10\mu\text{m}$, 15 minutes has $74\pm 6\mu\text{m}$, and 20 minutes has $104\pm 8\mu\text{m}$ of SiC depletion. Scale maker indicates $50\mu\text{m}$.

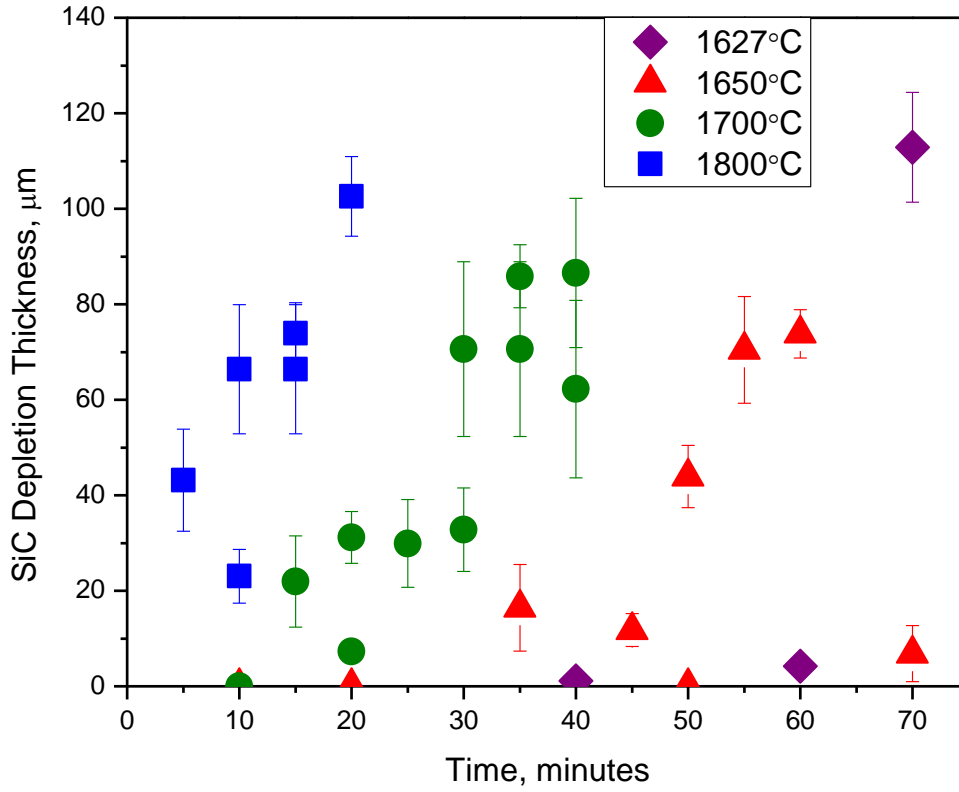


Figure 45. SiC depletion depth versus time in minutes for oxidized ZrB₂-30 vol% SiC.

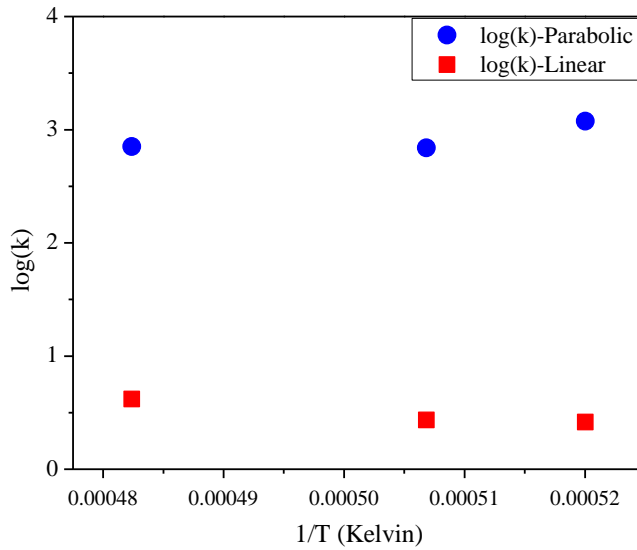


Figure 46. Log(k) versus 1/T for both linear and parabolic growth of the SiC depletion layer in oxidized ZrB₂-30 vol% SiC. k_l is $\mu\text{m}/\text{min}$ and k_p is $\mu\text{m}/\text{min}^{1/2}$. No temperature dependence is evident, indicating gas phase diffusion is rate limiting for growth of the SiC depletion layer.

Discussion

Temperature Considerations for Resistive Heating Technique

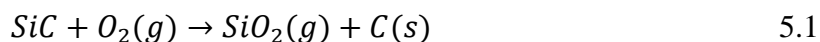
The use of an emissivity-correcting pyrometer and the rapid oxidation kinetics should lead to steady state emissivities and relatively accurate measurement of the temperature^{82, 83}. However, fluctuations in the temperature reading of the pyrometer occurred during testing with standard deviations of 4-64°C (Appendix 2). This standard deviation is consistent with the melting point calibration, which deviated -28°C and -16°C for Pt and Pd, respectively. The fluctuating temperature readings can be attributed to bubbling of the borosilicate making temperature measurement difficult. It may also be due in part to difficulties in maintaining the precise current needed for constant temperature. Given this temperature measurement uncertainty, the 1627°C transition temperature between oxidation regimes would be more accurately expressed as 1627°C±25. This temperature range is however supported by results in the literature^{15, 18, 24, 25, 84}.

Oxide Morphology Regime I: Temperatures <1627°C

Due to the low hardness of the ZrO₂+C oxide layer relative to the borosilicate layer and ZrB₂+SiC base material, pullout of the C between the ZrO₂ grains during polishing can be easily mistaken for porosity. In addition, the presence of C is difficult to distinguish from epoxy for specimens mounted and impregnated for cross-sectional characterization. Fracture sections avoid both complications, enabling the definitive identification of C as in Figure 36 through Figure 38, and Figure 43.

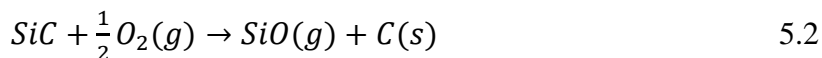
The preferential oxidation of the Si from SiC leaving C is attributed to the low partial pressure of oxygen under the borosilicate scale. Cooper and coworkers also observed the

formation of C due to the oxidation of SiC fibers in glass ceramic composites^{85, 86}. They called this phenomena “carbon-condensed oxidation” as given by the displacement Reaction 5.1.



Their work suggested that at low oxygen activities the more stable oxide, SiO₂, formed rather than CO(g). They also proposed that direct formation of SiO₂ adjacent to the C which required diffusion of Si through C. It was not possible to reproduce their thermodynamic calculations and the source of their thermodynamic data is unclear. Related behavior is also seen within samples which contain BN and SiC, wherein SiO₂ and CO(g) form, while the BN remains unoxidized, due to limited oxygen within the sample and B₂O₃ being less thermodynamically stable than SiO₂ and CO(g)⁸⁷.

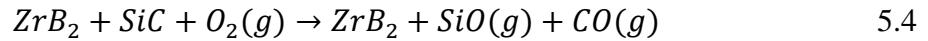
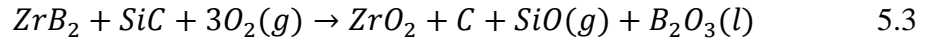
An alternate reaction to that of Cooper et al. is proposed here, considering oxidation of ZrB₂-SiC at low partial pressures of oxygen, given by Reaction 5.2.



This new finding of C in the ZrO₂ scale indicates CO(g) production below 1627°C cannot form at sufficient pressures to produce bubbles in the borosilicate scale, contrary to the bubble formation model proposed in Chapter 4 to describe oxidation variability. Work by Katsui et al. has suggested that oxidation controlled by CO(g) diffusion through SiO₂ during oxidation of SiC would result in both a C layer and bubbling within the SiO₂, and a similar dependence could be responsible for the behavior seen here⁸⁸. However, according to Zheng et al. CO(g) molecules are small and unlikely to limit diffusion⁶⁰. In addition, Katsui et al. showed no change in their log(k) vs. 1/T slope, which would be necessary for the transition from O₂(g) diffusion limited to CO(g) diffusion limited they claim.

Transition from C Condensed Oxidation to SiC Depletion

Reaction 5.3 represents the observed phases at the oxide/base material interface for temperatures $<1627^{\circ}\text{C}$. Similarly, Reaction 5.4 represents the observed phases at the depletion layer/base material interface for temperatures $\geq 1627^{\circ}\text{C}$. Note that ZrB_2 is only included in Reaction 5.4 to represent the observed interface and phases for comparison to Reaction 5.3, but does not enter in the reaction.



Reactions 5.3 and 5.4 are rewritten in Table 10 balanced for various vol% SiC and 1 mole of $\text{O}_2(\text{g})$ and shown in Figure 47. Figure 47 is an Ellingham diagram, including Reactions 5.3 and 5.4, plotted using data from FactSage calculations. Note that the slopes of the lines in Figure 47 reflect the negative of the entropy of each reaction⁸⁹. For Reaction 5.3 there is a net loss of two gas molecules, reflecting a significant decrease in entropy. The free energy of formation therefore increases with temperature (positive slope). For Reaction 5.4, in which there is a net production of one gas molecule (increase in entropy), the slope is negative. These slope differences necessitate a transition from Reaction 5.3a to Reaction 5.4a at high temperatures since the lower Gibbs energy reaction will be favored. Note that the transition temperature calculated for Reactions 5.3a and 5.4a with 30 vol% SiC occurs at a temperature higher than observed experimentally. If however, the ZrB_2/SiC mole ratio is varied, the net change in gas molecules/mole of O_2 varies for Reaction 5.3, whereas Reaction 5.4 is unaffected. As the mole fraction of SiC increases, the slope of ΔG for Reaction 5.3 decreases and the transition temperature to form the oxidation products $\text{C}+\text{ZrO}_2+\text{SiO}(\text{g})+\text{B}_2\text{O}_3$ (Reaction 5.3) versus $\text{SiO}(\text{g})+\text{CO}(\text{g})$ (Reaction 5.4) moves to lower temperatures. The computed transition temperature

occurs between 1610°C and 1630°C, in agreement with the experimental temperature, for ZrB₂-60 vol% SiC and ZrB₂-65 vol% SiC. Thus, thermodynamics of locally SiC-rich microstructures better reflect the observed transition temperature from ZrO₂+C oxide layer formation to SiC depletion as temperature is increased.

The change in stable oxidation products from ZrO₂+C to SiC depletion corresponds with the significant jump in ZrO₂ oxide thickness, as documented in Table 9. As the oxidation mechanism changes from Reaction 5.3 to Reaction 5.4, the C oxidizes to CO(g), generating more gas products. The additional gas products result in increased bubbling of the borosilicate glass, which was observed in post-test analysis (Figure 48.) Increased bubbling would reduce the thickness of the protective glass layer, allowing ingress of oxygen to the ZrB₂, thereby increasing the ZrO₂ growth rates.

Reaction	% Vol SiC	Balanced reaction for 1 mole O ₂ (mol%)	Transition temperature (°C)
5.3a	30	0.35ZrB ₂ +0.22SiC+O ₂ = 0.35ZrO ₂ (s)+0.22C(s)+0.22SiO(g)+0.35B ₂ O ₃ (l)	1725
5.3b	60	0.2865ZrB ₂ +0.657SiC+O ₂ = 0.2865ZrO ₂ (s)+0.657C(s)+0.657SiO(g)+0.2865B ₂ O ₃ (l)	1630
5.3c	65	0.2549ZrB ₂ +0.725SiC+O ₂ = 0.2549ZrO ₂ (s)+0.725C(s)+0.725SiO(g)+0.2549B ₂ O ₃ (l)	1610
5.4a	30	1.564ZrB ₂ +SiC+O ₂ = 1.564ZrB ₂ +SiO(g)+CO(g)	N/A

Table 10. Balanced reactions for transition in ZrB₂-SiC oxidation behavior.

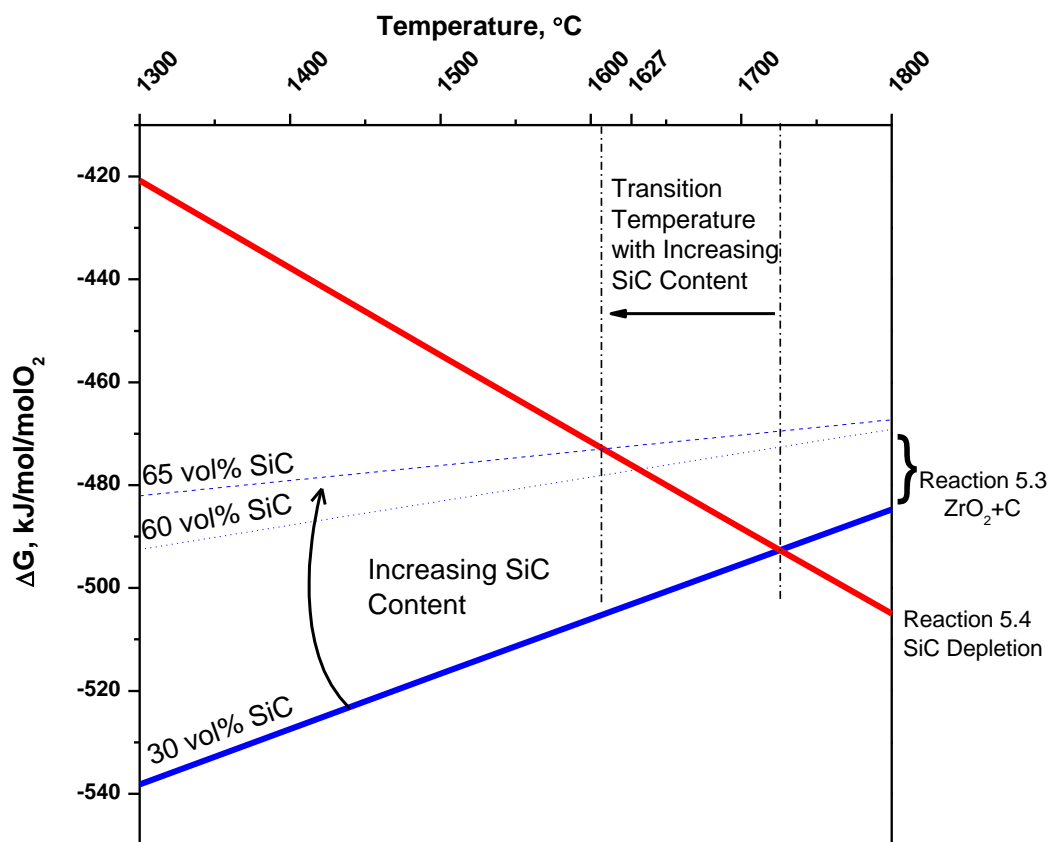


Figure 47. Ellingham diagram, plotted using FactSage, showing reactions of ZrB₂-SiC with 1 mole of O₂. This diagram explains the transition between oxidation regimes.

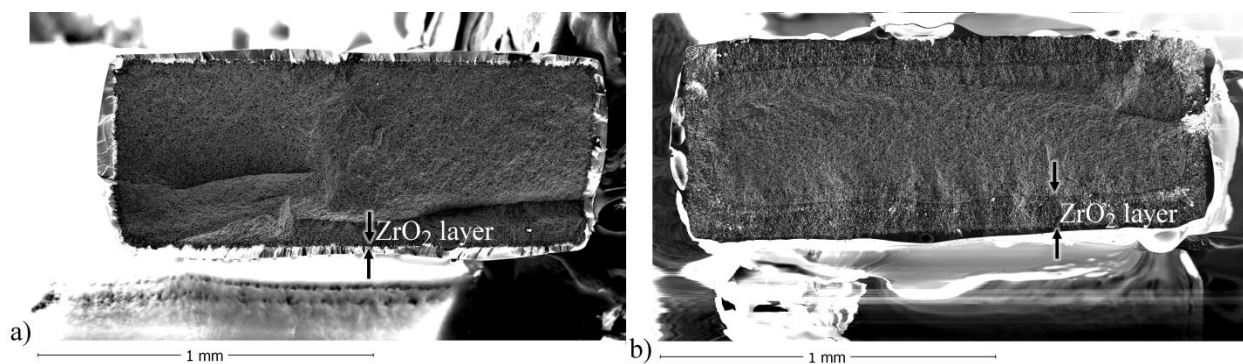


Figure 48. Fracture section of ZrB₂-30 vol% SiC oxidized in flowing O₂ using resistive heating system at a) 1600°C for 55 minutes b) 1650°C for 50 minutes, showing increased bubbling and ZrO₂ in b).

Oxide Morphology Regime II: Temperatures $\geq 1627^\circ\text{C}$

The presence of partially oxidized SiC grains at the SiC depletion layer/base material interface is a strong indication of active oxidation (Figure 41). The PO_2 at the $\text{ZrO}_2/\text{ZrB}_2$ interface must be low enough that $\text{SiO}(\text{g})$ is more stable than $\text{SiO}_2(\text{s,l})$. The equilibrium PO_2 at the $\text{ZrO}_2/\text{ZrB}_2$ interface (Reaction 1.1) was calculated to be 5.3×10^{-20} atm, assuming that the activity of all condensed phases are unity. However, SiO_2 is also present at this interface as shown in Figure 39 and schematically in Figure 49. Under such low partial pressures, SiO_2 would reduce to $\text{SiO}(\text{g})$ at a pressure of 2.7×10^{-6} atm and $\text{O}_2(\text{g})$ at a pressure of 1.1×10^{-6} atm by the reverse of Reaction 2.1, providing a source of oxygen for further active oxidation of SiC. This again requires consideration of local equilibrium thermodynamics with large oxygen potential gradients to explain the observed microstructures containing $\text{ZrB}_2/\text{ZrO}_2/\text{SiO}_2$ junctions. The $\text{O}_2(\text{g})$ generated by reduction of SiO_2 adjacent to the $\text{ZrO}_2/\text{ZrB}_2$ interface diffuses through the pores to enable rapid active oxidation of SiC to greater depths in the ZrB_2 , as shown schematically in Figure 49. The literature suggests $\text{CO}/\text{CO}_2(\text{g})$ counter-current diffusion could also be used to explain the source of $\text{O}_2(\text{g})$ for further active oxidation of the SiC^{26, 90}.

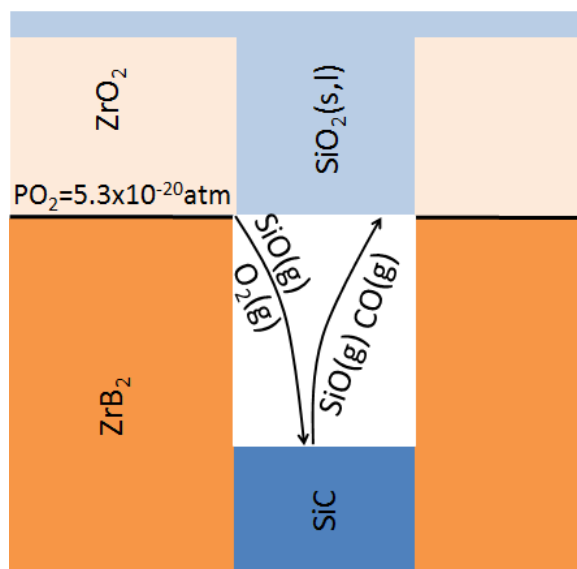


Figure 49. Diagram illustrating disassociation of SiO_2 to $\text{SiO}(\text{g})$ and $\text{O}_2(\text{g})$, which provides a source of $\text{O}_2(\text{g})$ for continued growth of the SiC depletion layer, limited by gas phase diffusion.

Depletion Kinetics

Figure 46 shows that the temperature dependence of observed depletion layer growth is minimal, suggesting that gas phase diffusion is rate limiting. If the depletion layer growth rate limiting step involved a bond breaking reaction or solid-state diffusion, there would be a strong temperature dependence (such as was seen in Figure 34 for ZrO_2 growth.) Linear growth is rejected as it would require a constant diffusion length for the oxygen, and this work has shown that the depletion layer grows with time, increasing the diffusion length for $\text{O}_2(\text{g})$ inward or $\text{SiO}(\text{g})$ outward (Figure 44 and Figure 45.) It is concluded that parabolic, gas phase diffusion limited growth of the depletion layer best explains the observed results for SiC depletion during oxidation of ZrB_2 -30 vol% SiC at temperatures of 1627°C and above. This mechanism is consistent with tracer diffusion results, which will be reported in Chapter 6. As in the case of the transition from C formation to SiC depletion, it was again necessary to consider thermodynamics

at the local microstructural $\text{ZrB}_2/\text{ZrO}_2/\text{SiO}_2$ junction to explain how $\text{O}_2(\text{g})$ diffusion can be the rate limiting mechanism.

Conclusions

ZrB_2 -30 vol% SiC oxidation behavior has been characterized at temperatures of 1300°C to 1800°C. For temperatures below 1627°C, a two layer oxide is formed with ZrO_2+C below a borosilicate glass layer. For temperatures of 1627°C and above, a three layer oxidation/depletion morphology was observed, with SiC depletion occurring in the ZrB_2 beneath the ZrO_2 and borosilicate oxide layers. The growth of the SiC depletion layer is best explained assuming parabolic gas diffusion limited active oxidation of SiC to $\text{SiO}(\text{g})$. Consideration of local microstructural equilibrium was required to explain the C formation and SiC depletion behavior observed below and above 1627°C.

Recommendations for Future Work

1. Further analysis of the SiC depletion growth at more times and temperatures, as well as more repeated tests, may lead to a firmer understanding of the temperature dependence of the growth rate.
2. The transition temperature proposed here should be investigated more rigorously. Work in the literature only addresses $\leq 1500^\circ$ and $\geq 1627^\circ\text{C}$; no previous work has been done at intermediate temperatures. This work used box furnace tests show ZrO_2+C at the highest testing temperature (1550°C) and resistive heating tests to show the same behavior up to 1600°. Further tests at 1600°C-1650°C, with a very reliable temperature calibration, would assist in setting the exact transition temperature and incubation time.
3. The specimen oxidized at 1650°C for 20 minutes, showed very interesting oxidation behavior with both C and pores appearing in the oxide. This has supported the

microstructural dependence of the transition temperature. A more systematic microstructural analysis of the sample could result in further revelations.

4. Observations of ZrO_2+SiC are reported at 1327°C . This could indicate that another low temperature oxidation mechanism exists. The temperature and time for transition from ZrO_2+SiC to ZrO_2+C should be investigated. However, these low use temperatures (1327°C) are not relevant for TPS, so are more of an academic curiosity.

Chapter 6 Task 3- Oxygen Diffusion Mechanism

Objective

The objective of this task was to determine oxygen diffusion pathways and mechanisms in the complex oxide scales formed on ZrB₂-30 vol% SiC using ¹⁶O₂-¹⁸O₂ double oxidation experiments. The composition of the borosilicate layer was first characterized since oxygen diffusion is known to vary dramatically with boron content of the glass ³⁰.

Results

B₂O₃ Concentration in the Borosilicate Glass Layer

The average borosilicate composition formed on ZrB₂-30 vol% SiC was determined for specimens oxidized between 1300°C and 1500°C for times between 100 and 221 minutes in stagnant air using ICP-OES. More detailed compositional analysis was performed on specimens oxidized at 1500°C for 10 and 100 minutes. B compositional depth profiles were obtained by XPS and estimated by performing EDS at varying accelerating voltages.

Average Borosilicate Composition

Borosilicate glass was dissolved off oxidized specimens using a three step dissolution process (H₂O, H₂O, HF) as described in Chapter 3. SEM and EDS results are given in Figure 50, showing that trial 1, which used a borosilicate glass dissolution step of 3ml HF for 24hrs, removed all of the glass and ZrB₂, leaving only SiC. Trial 2 used more dilute HF acid to dissolve the glass layer, leaving some ZrO₂ grains on the specimen surface, which were not found in trial 1. However, the results do confirm that nearly all of the glass phase was removed for all trials. These results demonstrate that the assumption that all the glass was removed in the water and HF dissolution procedure is reasonable. The ICP-OES compositional results of solutions from the stepwise dissolution are assumed to account for all of the borosilicate glass formed during

oxidation. Note that SiC is not soluble in H₂O or HF as confirmed by SEM (Figure 50) so that Si content in the solutions must be attributed to SiO₂.

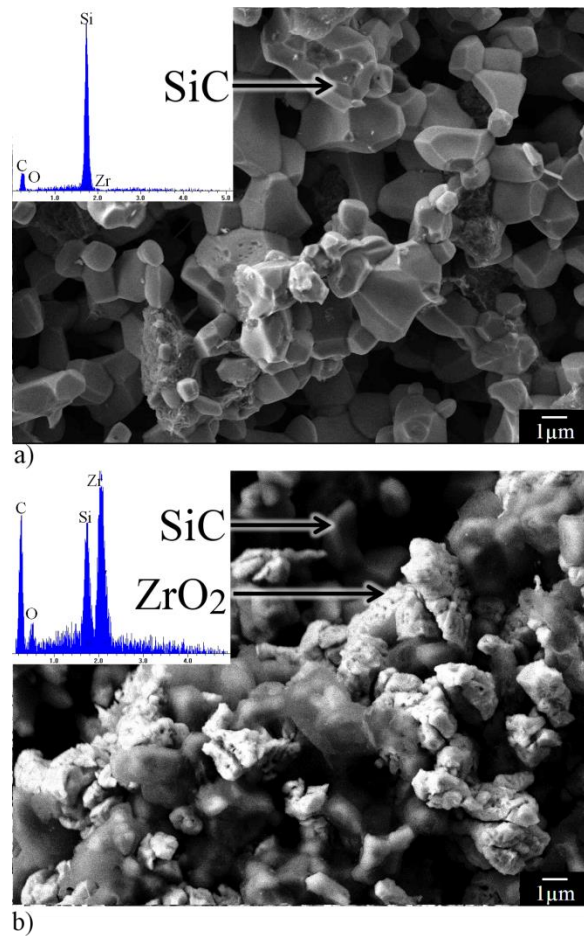


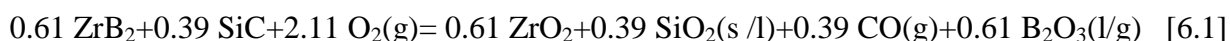
Figure 50. SEM/EDS results for ZrB₂-30 vol% SiC oxidized at 1500°C for 100 minutes in stagnant air after two DI H₂O soaks and dissolution in a) 3ml of HF solution at 35°C for 24 hours b) 3ml of HF solution diluted with 12mL of DI H₂O at 35°C for 24 hours, showing the area with the most products left behind after dissolution.

Condition	Trial #	Mass change – oxidation (+mg/cm ²)	Average (+mg/cm ²)	Mass change – leaching (-mg/cm ²)	Average (-mg/cm ²)
1500 °C 100 minutes	1	2.811	2.902±0.263	0.703	0.910±0.278
	2	3.199		1.226	
	3	2.697		0.801	
1400 °C 128 minutes	1	3.847	4.554±0.684	1.129	2.069±1.049
	2	5.212		3.200	
	3	4.602		1.878	
1300 °C 221 minutes	1	3.456	4.614±1.055	2.392	2.380±0.374
	2	5.522		2.748	
	3	4.864		2.000	
1400 °C 221 minutes	1	6.284	7.104±1.038	4.292	3.942±0.453
	2	8.271		4.105	
	3	6.757		3.430	
1500 °C 221 minutes	1	4.384	4.913±0.493	1.479	2.019±0.743
	2	4.996		1.712	
	3	5.359		2.867	

Table 11. Mass change data for ZrB₂-30 vol% SiC oxidized under stagnant air in a standard box furnace after oxidation and after H₂O soak (leaching).

The specific mass change from the three oxidation trials and the B₂O₃ leaching process are reported in Table 11. The “Mass change-oxidation” is the measured change in mass of the specimen after oxidation under the stated conditions. The “Mass change-leaching” is the mass of material removed after both of the H₂O soaks. This was determined by subtracting the specimen mass after the H₂O baths from the mass after oxidation and was expected to be composed of mostly B₂O₃ with trace amounts of SiO₂.

Since B₂O₃ has a high vapor pressure at temperatures of interest, significant amounts are expected to volatilize, depleting the scale in B₂O₃. The B₂O₃ retained in the glass layer after oxidation was calculated assuming: 1) an equal rate of consumption of the ZrB₂ and SiC in the base material during oxidation, 2) the water leaching steps removed all of the B from the glass layer⁷⁰, and 3) all of the Si from the glass layer was removed in the H₂O and HF acid soaks. The validity of these assumptions is discussed later. For this calculation, the concentration of B and Si in the glass layers of each specimen was determined by ICP in mg/L and then multiplied by 0.015L, the volume of each solution. This yielded the mass in mg of dissolved B and Si, which was then easily converted to moles. Since the SiO₂ does not volatilize in this temperature range, multiplication of the amount of Si in moles by the stoichiometric ratio of B to Si expected from:



(where 39 mol% corresponds to the 30 vol% used in this study) yields the total amount of B expected if none volatilizes (see Appendix 4 for an example calculation.) Comparison of the B concentration found from ICP-OES to the total amount oxidized from ZrB₂ according to the above calculations gives the percent of retained B in the oxide relative to the borosilicate composition expected in the absence of volatilization. Table 12 provides a summary of these calculations.

	Condition	Trial #	B ₂ O ₃ content of glass (mol%)	Average B ₂ O ₃ content	% of Total B retained in glass (mol%)	Average B retained
“Constant” Oxide Thickness	1500 °C 100 minutes	1	27.25	27.25±4.10	23.9	22.6±4.68
		2	29.21		26.4	
		3	21.33		17.3	
	1400 °C 128 minutes	1	31.86	36.79±5.71	28.5	37.3±10.09
		2	43.05		48.3	
		3	35.47		35.1	
	1300 °C 221 minutes	1	43.23	42.85±1.63	43.3	46.2±3.98
		2	44.26		50.8	
		3	41.07		44.6	
“Constant” Time	1400 °C 221 minutes	1	34.20	36.85±2.43	37.3	38.8±1.86
		2	38.99		40.9	
		3	37.35		38.1	
	1500 °C 221 minutes	1	27.32	28.19±1.96	24	25.1±2.46
		2	26.83		23.4	
		3	30.43		28	

Table 12. Summary of B retained in the borosilicate scale after oxidation of ZrB₂-30 vol% SiC under stagnant air conditions. A high percentage of the B does not volatilize under the conditions tested, leading to a high B₂O₃ concentration in the borosilicate glass.

Figure 51 is a plot of the total mass of oxides generated versus temperature for specimens which were oxidized with the goal of attaining the same amount of oxidation. The total mass of generated oxides includes the mass gained during oxidation and the calculated mass of $B_2O_3(g)$ and $CO(g)$ which have formed and vaporized (assuming all C has oxidized.) The similar mass results for the three temperatures and three trials show that the chosen times to provide similar quantities of oxidation, allowing comparison between these tests. Figure 52 is a plot of total mass of generated oxides versus temperature for specimens all oxidized for 221 minutes, showing with 80% confidence an increase in the amount of oxide formed with increasing temperature.

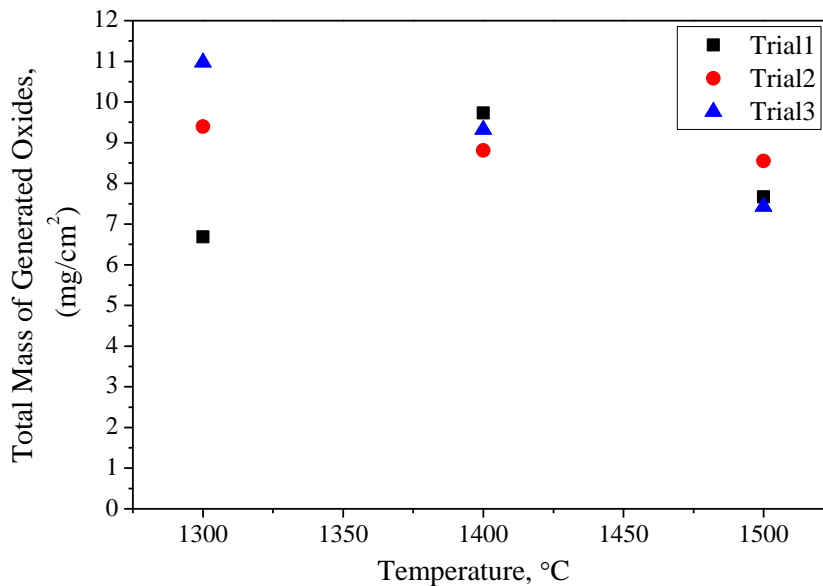


Figure 51. Total mass of generated oxides versus temperature for ZrB_2 -30 vol% SiC specimens oxidized to generate the same oxide thickness. 1300°C specimens oxidized for 221 minutes, 1400°C specimens oxidized for 128 minutes, and 1500°C specimens oxidized for 100 minutes. Similar mass gain indicates correct choice of oxidation times for generating the same quantity of oxide products.

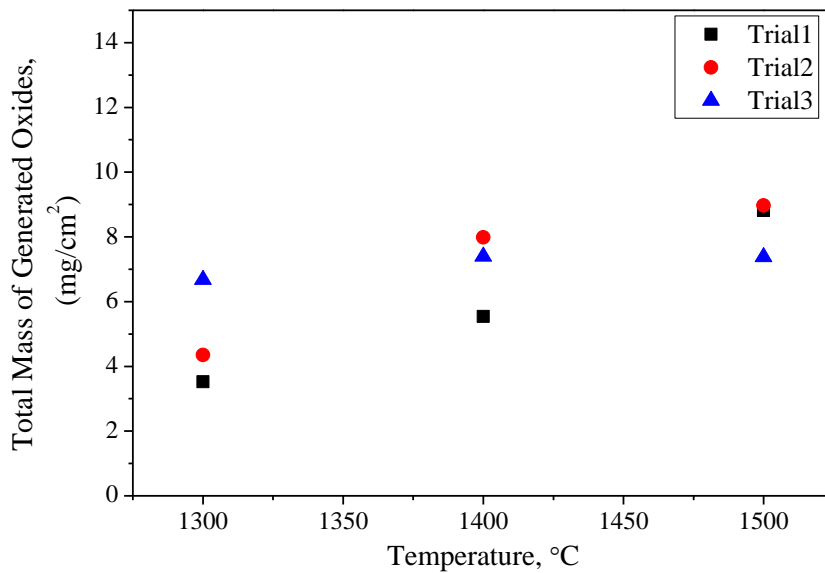


Figure 52. Total mass of generated oxides versus temperature for ZrB_2 -30 vol% SiC specimens oxidized for 221 minutes, showing an increase in oxide formation with increasing temperature.

Surface Concentration of B in Borosilicate Glass

XPS results of oxidized specimen surfaces are given in Figure 53. For both 10 and 100 minute exposures, less than 1% B was evident on the surface, but after sputtering 50nm, the B content became measureable and steadily increased with depth to 150nm into the surface, the deepest sputter depth analyzed. The B content measured by XPS after 100 minutes oxidation was about 5% lower than it was after 10 minutes oxidation, while the Si content increased 5%. The O and Zr values were equivalent and constant for the two scales.

Estimated B Concentration Profile Using EDS

EDS was performed on the surface of a specimen oxidized at 1500°C for 100 minutes, at a series of accelerating voltages (5kV, 10kV, and 20kV.) The Casino simulation program was used to determine the depth of the sampling volume for each accelerating voltage. These values are given in Table 13. A detailed description of the simulation results are provided in Appendix 3. Estimated B concentrations from the EDS results are plotted along with XPS data in Figure 54.

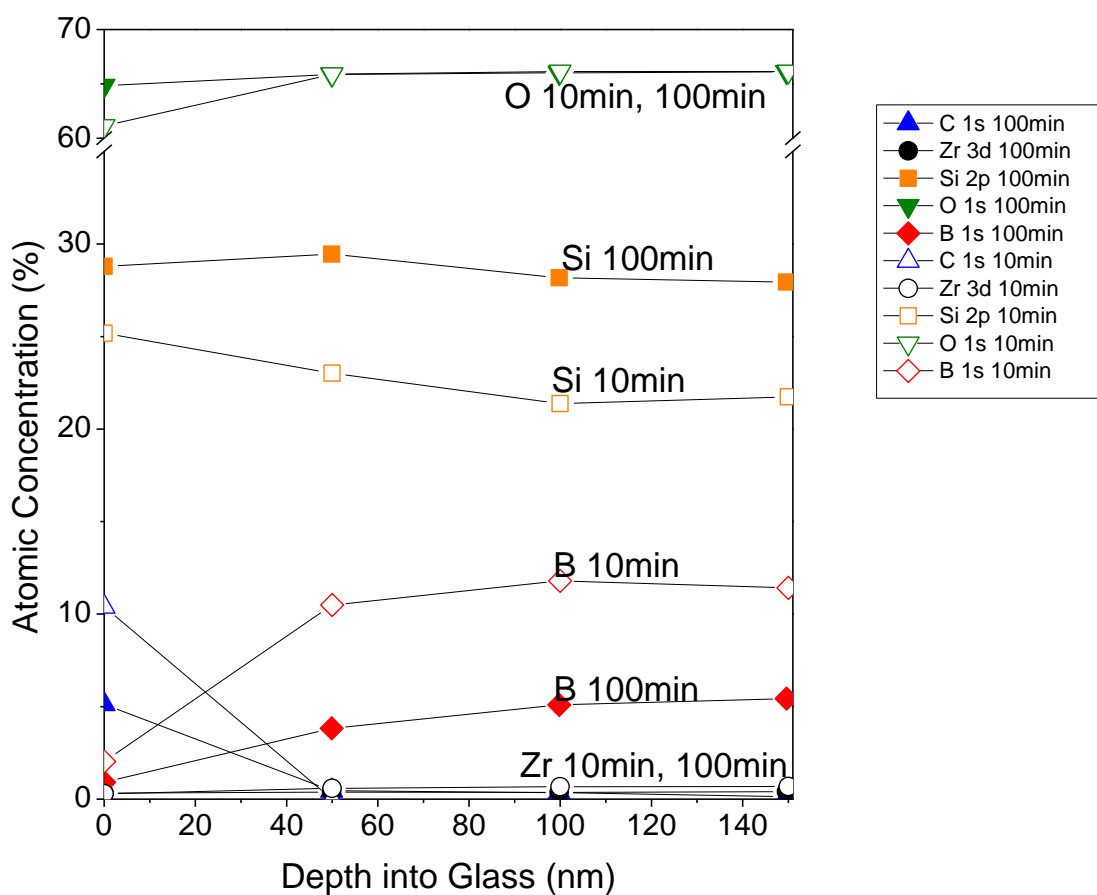


Figure 53. XPS results for ZrB₂-30 vol% SiC oxidized at 1500°C for 10 (open symbols) and 100 (closed symbols) minutes in stagnant air. Both conditions showed lower B content at the surface then inside the borosilicate scale. 100 minutes of oxidation showed decreased quantities of B with a corresponding increase in Si compared to oxidation for 10 minutes.

Accelerating voltage (kV)	B concentration (at%)	B ₂ O ₃ concentration (mol%)	Simulated average sampling depth (nm)
5	7.6	12.98	220
10	11	18.67	770
20	18.5	30.96	2900

Table 13. Concentration results from EDS performed at varying accelerating voltages, showing increased B concentration deeper in the borosilicate scale.

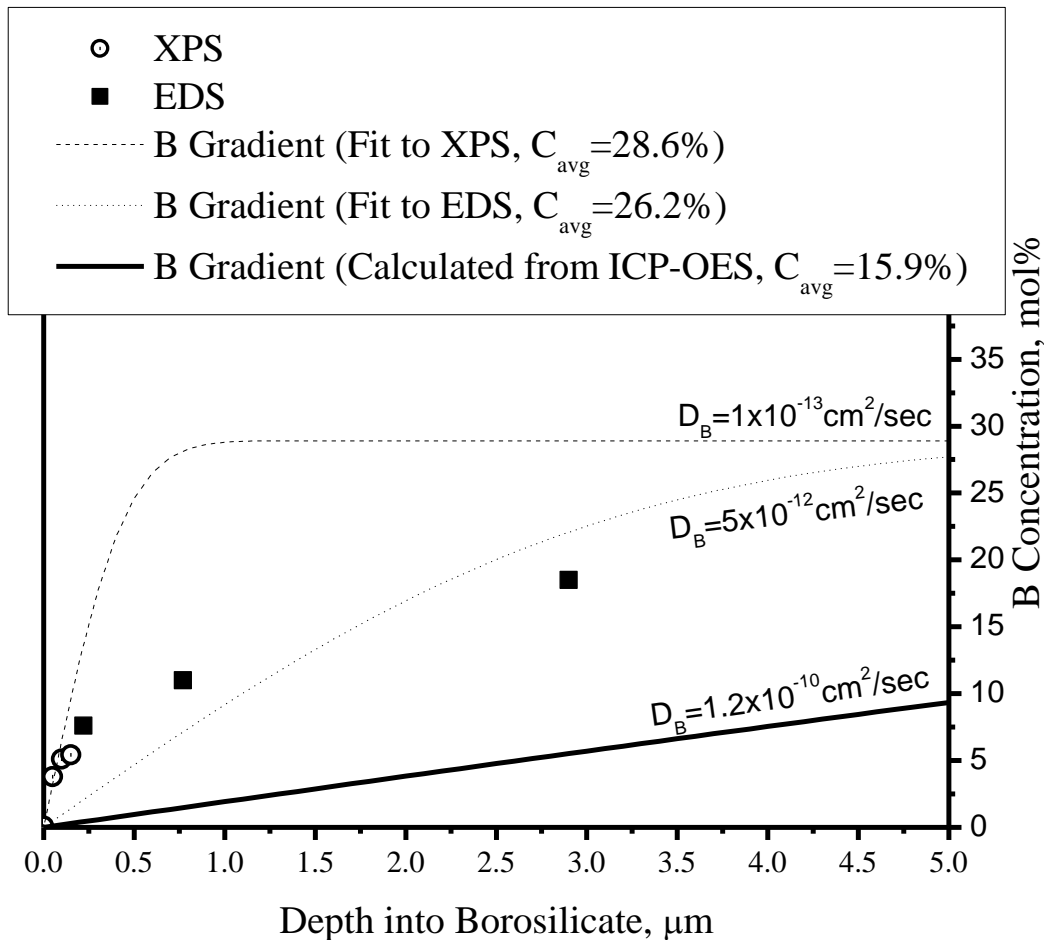


Figure 54. XPS and EDS results showing increased B deeper into the borosilicate glass for a specimen oxidized at 1500°C for 100 minutes in stagnant air, showing the first 5μm of the scale. Dotted line indicates B concentration using B diffusion coefficient from best fit to EDS results. Dashed line indicates B concentration using B diffusion coefficient from best fit to XPS results. Solid line indicates B concentration using calculated B diffusion coefficient from ICP-OES results.

Calculated B Concentration Gradient

The borosilicate glass layer formed after oxidation of ZrB₂-30 vol% SiC was approximated as a binary, semi-infinite system, and the error function solution to Fick's 2nd Law was used to calculate the B concentration gradient ⁹¹:

$$C_B = C_{\infty} \text{erf}(\eta) \quad [6.1]$$

$$\eta = \frac{x}{\sqrt{4Dt}} \quad [6.2]$$

$$\text{erf}(\eta) = \frac{2}{\sqrt{\pi}} \int_0^{\eta} e^{-\lambda^2} d\lambda \quad [6.3]$$

where C_B is the concentration of B at distance x into the borosilicate glass from the gas interface, C_{∞} is the equilibrium concentration of B at the oxide/base material interface, D is the diffusion coefficient of B in the borosilicate glass, and t is time. The following boundary conditions were used:

$$\text{BC1: } C_B=0 \text{ at } x=0$$

$$\text{BC2: } C_{\infty}=0.289 \text{ mole fraction (fixed by stoichiometry of ZrB}_2\text{-30 vol\% SiC) at } x=20.2\mu\text{m}$$

These boundary conditions are reasonable as XPS shows a very low B concentration (<1%) on the surface, and O₂(g) diffuses through the borosilicate and forms new oxide rapidly in comparison to B diffusion outward, so the concentration of B at the borosilicate glass/base material interface is constant. Choosing a fixed time, the B diffusion coefficient was determined using:

$$D_B = \frac{\left[\left(1 - \frac{C_{av}}{C_{\infty}} \right) \frac{\sqrt{\pi} x_I}{2} \right]^2}{t} \quad [6.4]$$

Solutions were obtained for a specimen oxidized at 1500°C after 100 minutes, which forms a borosilicate layer 20.2μm thick (BC2), since ICP-OES, XPS, and EDS compositional information are available for this oxidation condition. The average B concentration in the borosilicate glass after this oxidation treatment given by ICP-OES was 15.387 mol%, and the

concentration at the oxide/base material interface is assumed to be equal to that given by equilibrium, 28.9 mol% (BC2). The B diffusion coefficient was found to be $\sim 1.2 \times 10^{-10} \text{ cm}^2/\text{sec}$. This diffusion coefficient represents an average B diffusion coefficient in borosilicate glass resulting from ZrB_2 -30 vol% SiC oxidation at 1500°C for 100 minutes. B diffusion coefficients were also calculated which provided best fits to the XPS data and the EDS data and were $1 \times 10^{-13} \text{ cm}^2/\text{sec}$ and $5 \times 10^{-12} \text{ cm}^2/\text{sec}$, respectively. The D_B values will be discussed below. Resulting B concentration profiles are shown in Figure 54.

$^{16}\text{O}_2$ - $^{18}\text{O}_2$ Double Oxidation Experiments: ToF-SIMS/EDS/SEM Characterization

1500°C

SEM/ToF-SIMS results for a specimen oxidized at 1500°C for 10 minutes in $^{16}\text{O}_2$ and 9 minutes in $^{18}\text{O}_2$ are given in Figure 55. ^{18}O was present throughout both the borosilicate and ZrO_2+C layer. Figure 56 shows a line scan of the ^{18}O demonstrating relatively constant concentration of ^{18}O throughout the scale. Figure 57 compares ToF-SIMS ^{18}O and EDS compositional mapping to demonstrate that ^{18}O is found in ZrO_2 grains at the $\text{ZrO}_2/\text{ZrB}_2$ interface. The O_2 exchange rate at 1500°C in ZrO_2 was estimated, assuming that $^{18}\text{O}_2$ permeates through the borosilicate and between the ZrO_2 grains quickly. After 19 minutes of oxidation at 1500°C , ZrO_2 grains near the $\text{ZrO}_2/\text{ZrB}_2$ interface were approximately $3\mu\text{m}$ in diameter, so $^{18}\text{O}_2$ needed to diffuse at least $1.5\mu\text{m}$ for the grain to be fully exchanged. The $^{18}\text{O}_2$ exposure was 9 minutes, providing a lower limit of the diffusion rate on the order of $10^{-10} \text{ cm}^2/\text{sec}$.

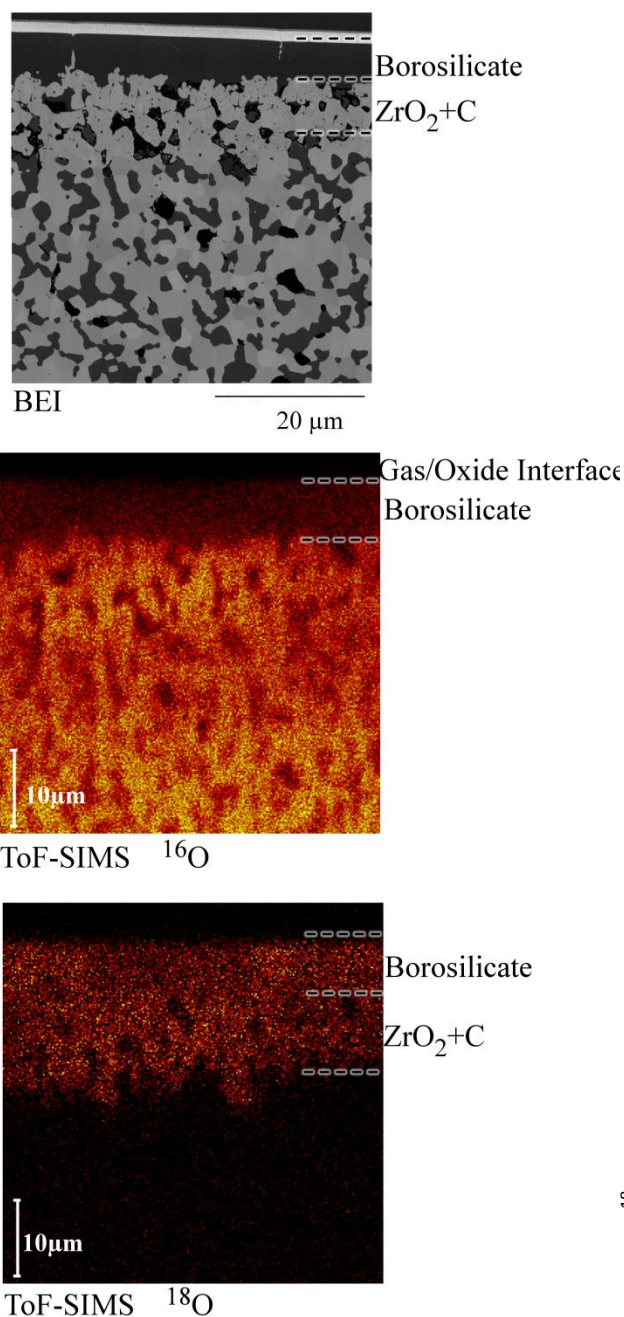


Figure 55. SEM/ToF-SIMS results for ZrB₂-30 vol% SiC oxidized at 1500°C for 10 minutes in ¹⁶O₂ and 9 minutes in ¹⁸O₂. ¹⁸O₂ is found throughout both the borosilicate glass and the ZrO₂+C layer.

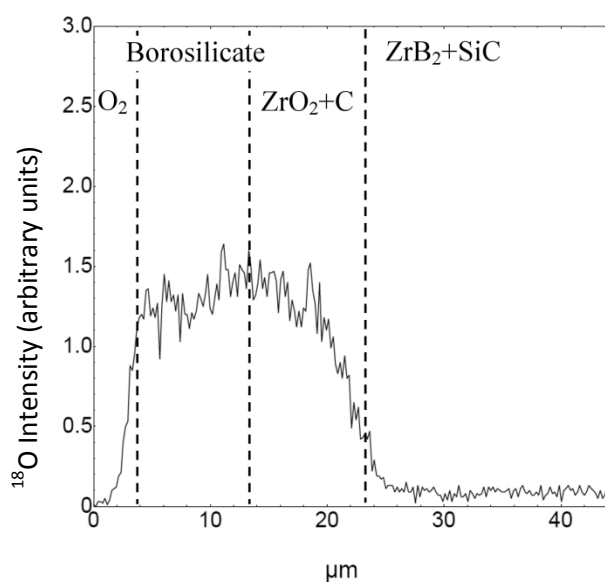


Figure 56. Line scan of ¹⁸O through oxide formed on ZrB₂-30 vol% SiC exposed at 1500°C for 10 minutes in ¹⁶O₂ and 9 minutes in ¹⁸O₂. Dashed lines mark approximate location of interfaces. ¹⁸O₂ is found to be relatively constant through borosilicate glass. ¹⁸O₂ gradient in ZrO₂+C layer may be artifact of line scan thickness.

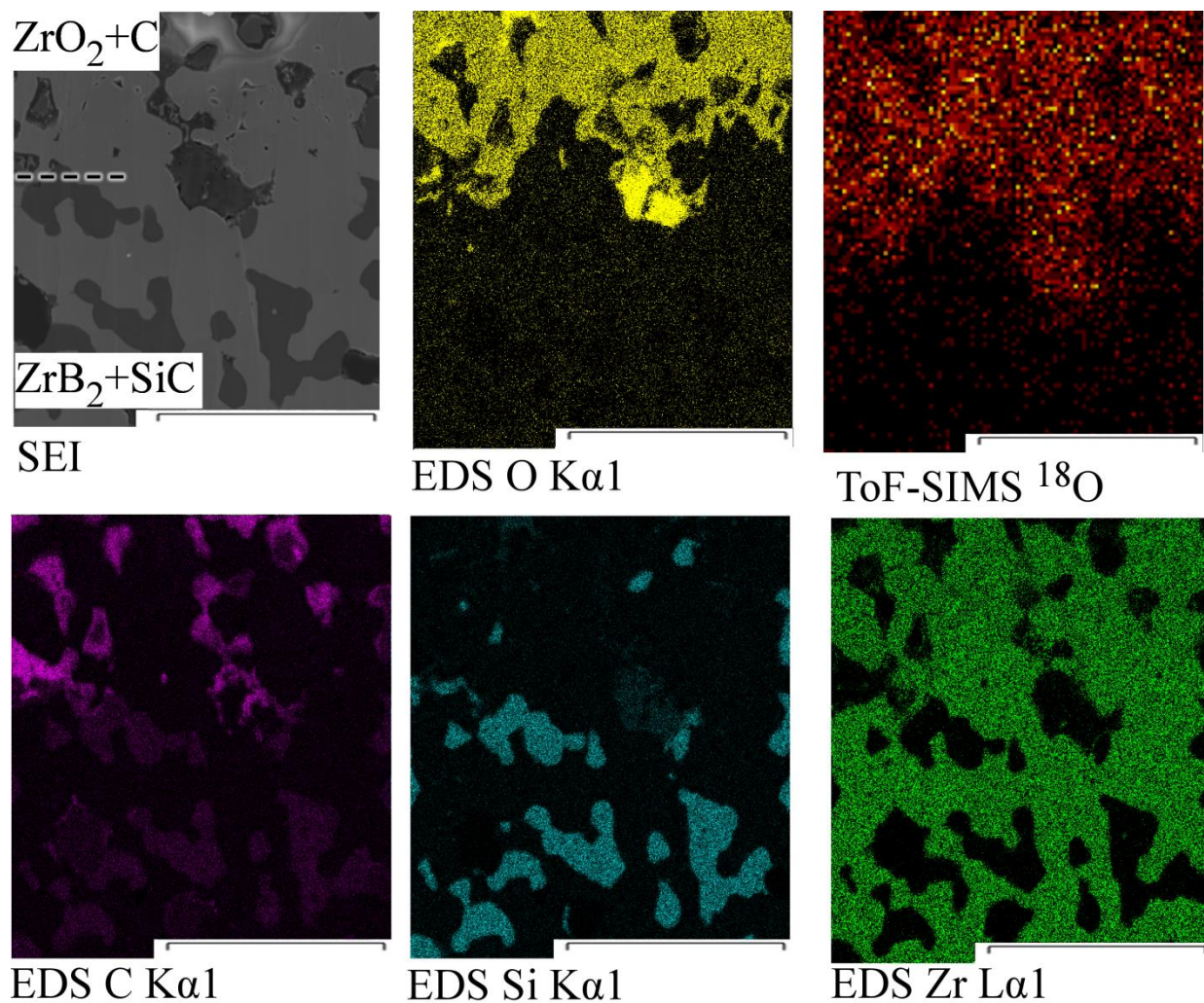


Figure 57. SEM/ToF-SIMS/EDS results for ZrB_2 -30 vol% SiC oxidized at 1500°C for 10 minutes in $^{16}\text{O}_2$ and 9 minutes in $^{18}\text{O}_2$, showing ^{18}O throughout the ZrO_2 grains even at the $\text{ZrO}_2/\text{ZrB}_2$ interface. Scale bar indicates $10\mu\text{m}$.

1650°C

SEM/ToF-SIMS results for a specimen oxidized at 1650°C for 29 minutes in $^{16}\text{O}_2$ and 45 seconds in $^{18}\text{O}_2$ are given in Figure 58 . These maps clearly show ^{18}O present at the gas/borosilicate glass interface, as well as at the borosilicate glass/depletion layer interface. The ^{18}O in the surface borosilicate layer was not evenly distributed, though SEM/EDS analysis did not detect any microstructural/compositional variations between ^{18}O rich areas and ^{16}O areas. Figure 59 shows the region oxidized with ^{18}O near the depletion layer, demonstrating the ^{18}O was located in the borosilicate glass, which at that location was surrounded by ZrB_2 grains. There was no evidence in this specimen of ^{18}O in ZrO_2 grains. This microstructure is very localized at the depletion layer and will be discussed in more detail later.

SEM/ToF-SIMS results for a specimen oxidized at 1650°C for 45 minutes in $^{16}\text{O}_2$ and 5 minutes in $^{18}\text{O}_2$ are given in Figure 60 and Figure 61. As observed in the 1500°C (10+9 minutes) specimen, ^{18}O was seen throughout the borosilicate layer and the ZrO_2 grains. The O_2 exchange rate at 1650°C in ZrO_2 was also estimated, again assuming $^{18}\text{O}_2$ diffusion to the edge of the grains is rapid. After 50 minutes of oxidation at 1650°C, ZrO_2 grains near the $\text{ZrO}_2/\text{ZrB}_2$ interface were approximately $5\mu\text{m}$ in diameter, so $^{18}\text{O}_2$ needed to diffuse at least $2.5\mu\text{m}$ for the grain to be fully exchanged. The $^{18}\text{O}_2$ exposure was 5 minutes, providing a lower limit to the diffusion rate on the order of $10^{-11}\text{cm}^2/\text{sec}$.

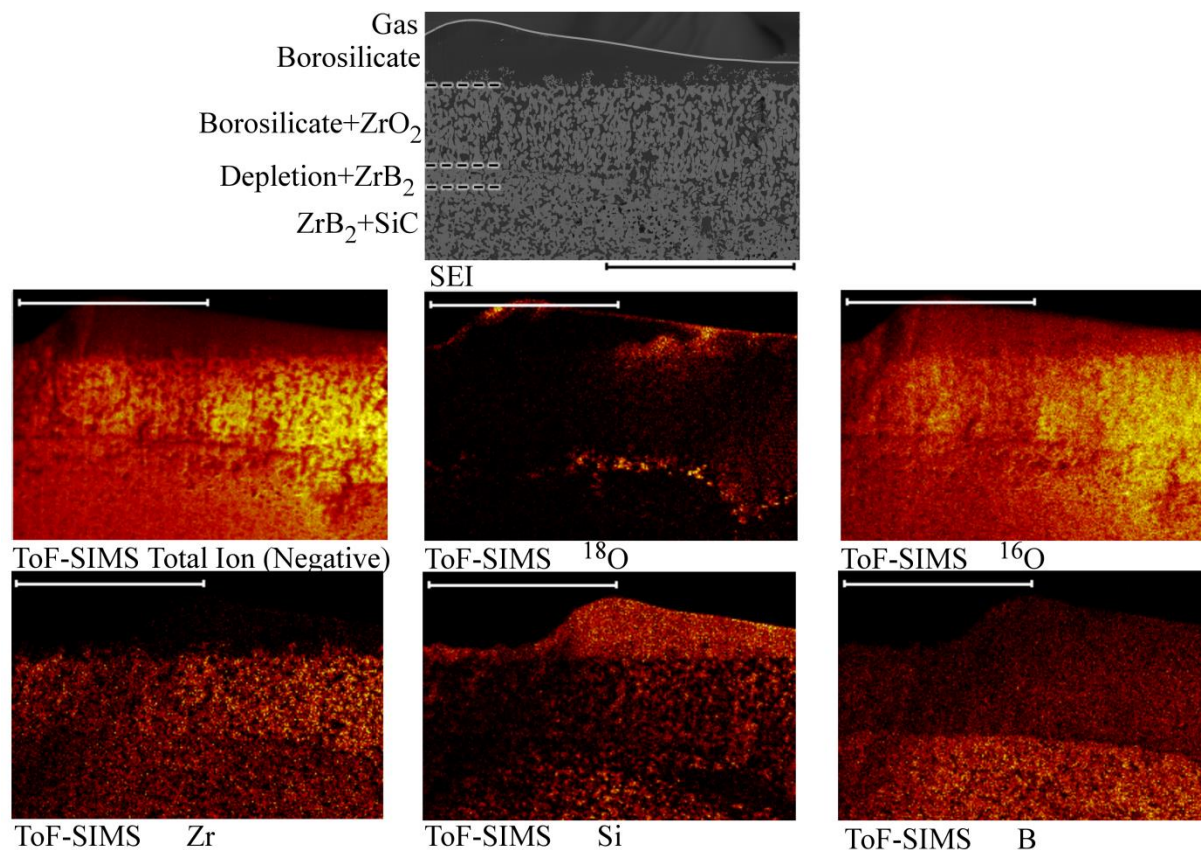


Figure 58. ToF-SIMS/SEM results for ZrB_2 -30 vol% SiC oxidized at 1650°C for 29 minutes in $^{16}\text{O}_2$ and 45 seconds in $^{18}\text{O}_2$. $^{18}\text{O}_2$ has exchanged with $^{16}\text{O}_2$ in initial borosilicate scale, and permeated through the borosilicate glass and formed new Si^{18}O_2 at the borosilicate glass/SiC depletion layer interface. Scale bar indicates $100\mu\text{m}$.

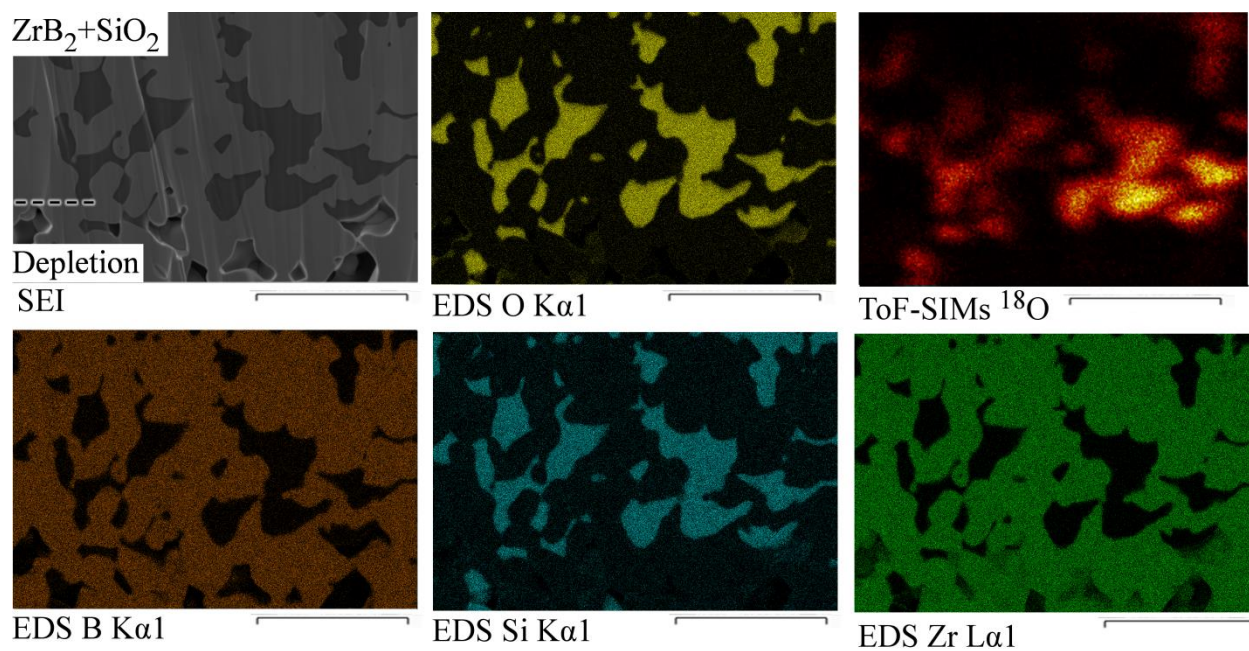


Figure 59. High magnification of ZrB_2 -30 vol% SiC oxidized at 1650°C for 29 minutes in $^{16}\text{O}_2$ and 45 seconds in $^{18}\text{O}_2$, showing ^{18}O in SiO_2 at the no depletion/SiC depletion interface. Scale bar indicates $10\mu\text{m}$.

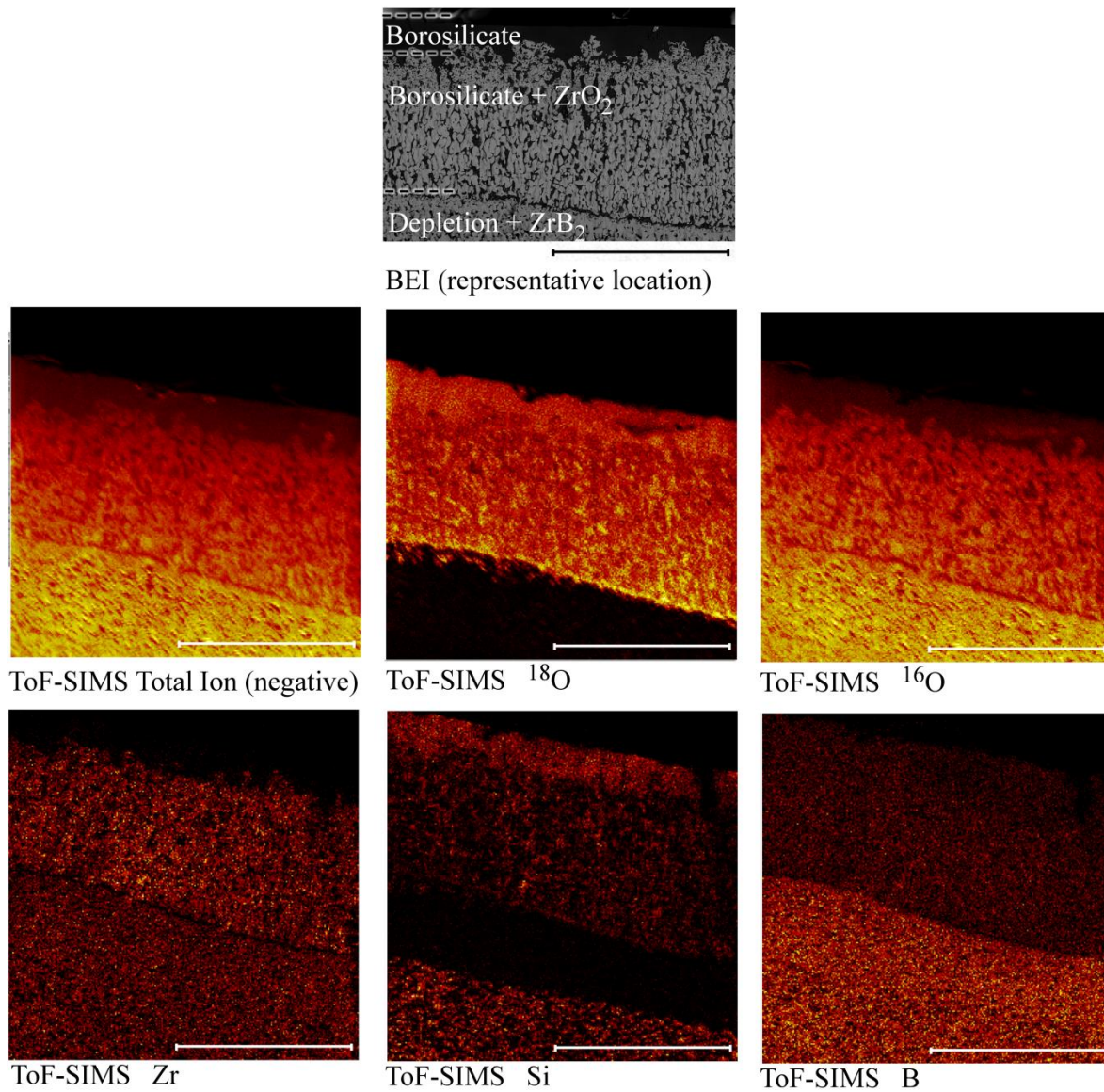


Figure 60. SEM/ToF-SIMS results for ZrB_2 -30 vol% SiC oxidized at 1650°C for 45 minutes in $^{16}\text{O}_2$ and 5 minutes in $^{18}\text{O}_2$. $^{18}\text{O}_2$ was found throughout the borosilicate glass and ZrO_2 grains. Scale bar indicates 100µm.

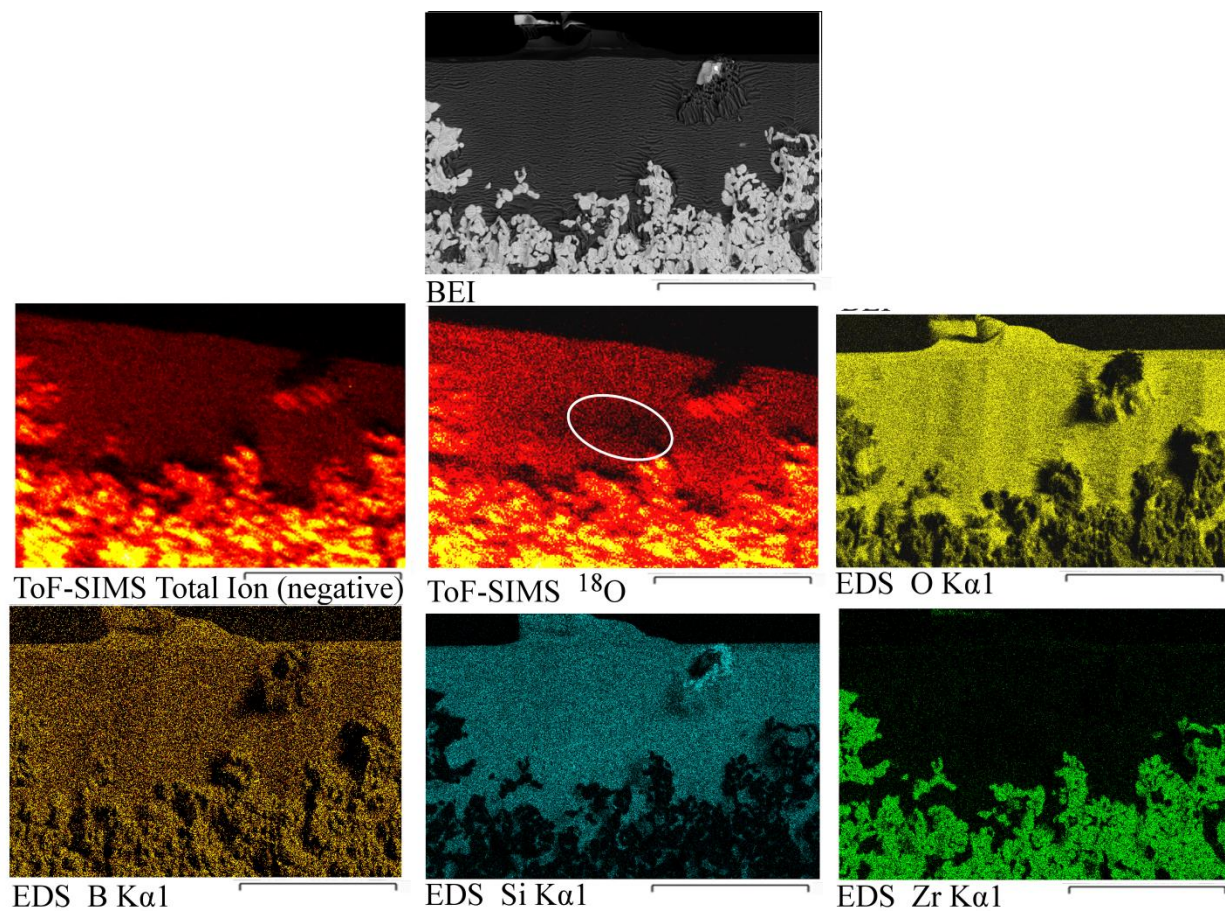


Figure 61. SEM/EDS/ToF-SIMS results for ZrB_2 -30 vol% SiC oxidized at 1650°C for 45 minutes in $^{16}\text{O}_2$ and 5 minutes in $^{18}\text{O}_2$. The circle marks an area in ^{18}O map showing less ^{18}O in in borosilicate glass. Scale bar indicates $20\mu\text{m}$.

Discussion

B₂O₃ Concentration in Borosilicate Glass

Assuming a linear concentration gradient from 0.289 mol% B (0.61 mole fraction B₂O₃) at the glass/zirconium diboride interface (which corresponds to ZrB₂-30 vol% SiC) to zero at the gas/borosilicate glass interface, the average B₂O₃ mole fraction is 0.305 which is intermediate to the results obtained at 1400°C and 1500°C, shown in Table 12. This suggests that the ICP-OES results are reasonable. The ICP-OES results confirm a higher depletion of B₂O₃ at 1500°C relative to 1300°C, consistent with expected B₂O₃ volatility. Comparing the mass gain behavior of the specimens (Table 11) to the total mass generated by the oxides in Figure 51 corroborates this B₂O₃ volatility.

B Concentration Profile

The B diffusion coefficient is expected to vary with borosilicate composition and will therefore vary with position in the oxide scale. The coefficient determined for the average composition from ICP-OES after oxidation at 1500°C for 100 minutes was $1.2 \times 10^{-10} \text{ cm}^2/\text{sec}$. The estimated EDS data, which is nearer to the surface and thus lower in B content, was best fit with a boron diffusion coefficient of $5 \times 10^{-12} \text{ cm}^2/\text{sec}$. The compositional data from the XPS represents the lowest B concentration due to proximity to the surface and was best fit with a boron diffusion coefficient of $1 \times 10^{-13} \text{ cm}^2/\text{sec}$. All of these diffusion coefficients are higher than previous measured values for B diffusion through borosilicate, which are on the order of $10^{-14} \text{ cm}^2/\text{sec}$ when extrapolated to 1500°C^{47, 49, 92}. The higher values of D_B are explained by the very high B₂O₃ concentration (average of 27mol%). The high values of the B diffusion coefficient estimated in this work are reasonable since borosilicate glass with 27mol% B₂O₃ is liquid at 1500°C as shown in the SiO₂-B₂O₃ phase diagram in Chapter 1 (Figure 2.) The estimated B

diffusion coefficient of $1 \times 10^{-13} \text{ cm}^2/\text{sec}$, obtained from best fit to the XPS data is reasonable as these data were taken near the surface where less B is present. The glass here will be more viscous and lower diffusion rates are predicted. Figure 54 compares B concentration profiles based on best fit for the ICP-OES average composition, XPS data, and EDS estimates.

Note also that the average B concentration determined by ICP-OES is a lower bound for B concentration. Bruckner⁷⁰ states that 95% of B_2O_3 is removed from borosilicate glasses by a warm water leach, however Adams and Evans⁹³ state that only 30% is removed. It is not possible to confirm the extent of B_2O_3 leaching in warm water at this time since ZrB_2 dissolves in HF. If B leaching in H_2O is incomplete, the average B composition in the borosilicate scale would be higher and the calculated B concentration would increase, bringing it in closer agreement with the XPS and EDS results in Figure 54.

A B_2O_3 concentration gradient in the borosilicate layer is proposed in Figure 62, for the first time providing compositional information about this layer. The $\text{B}_2\text{O}_3/\text{SiO}_2$ ratio at the oxide/substrate interface is assigned to be equal to the B/Si ratio in the base material. This is justified by two observations. First, XPS analysis showed that B-O and Si-O bonds are both observed on the oxidized surface after only 10 seconds, indicating both oxides are forming simultaneously at the start of oxidation (Chapter 4.) Second, a nearly uniform oxidation front is observed between ZrB_2/SiC and the oxides, as shown in Figure 63. The presence of the ZrO_2+C layer between the glass layer and the base material is neglected in Figure 62 and is not thought to affect the B/Si boundary condition at the interior glass interface. The B_2O_3 gradient in the plot was calculated by converting the B concentration gradient estimated from ICP-OES in Figure 54 to oxide. The discontinuity at the borosilicate/ ZrB_2+SiC interface results from the use of the average B concentration determined by ICP-OES to calculate an average diffusion coefficient.

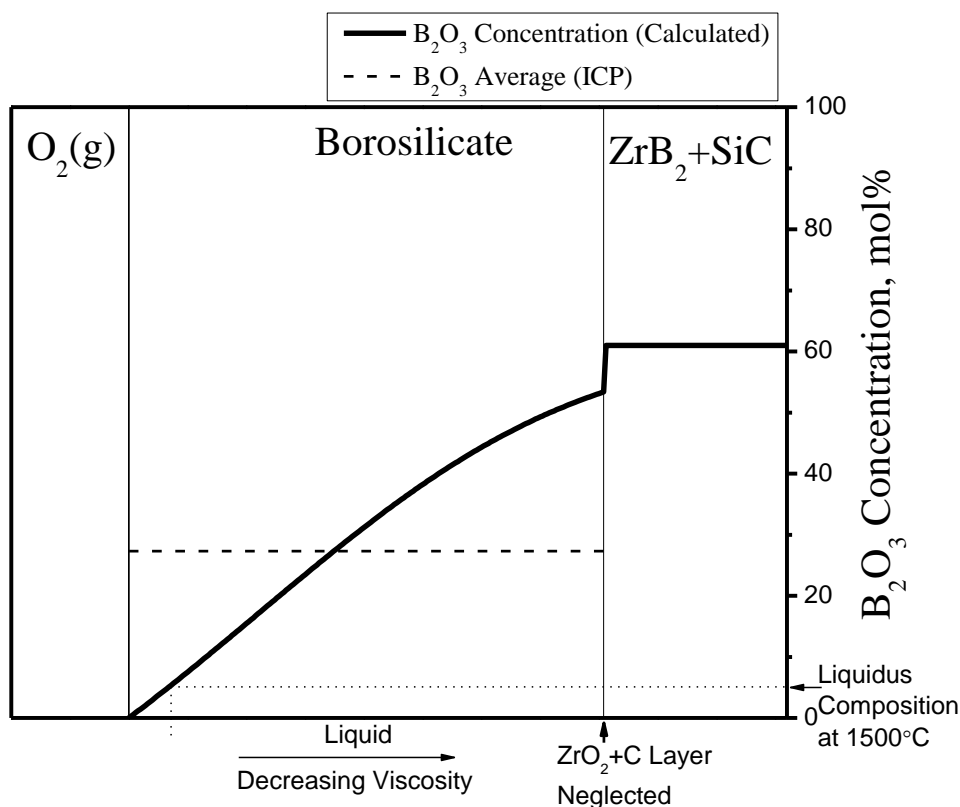


Figure 62. Approximate B_2O_3 concentration (mol%) throughout borosilicate glass scale formed during oxidation of ZrB_2 -30 vol% SiC. (Values given are for specimen oxidized at 1500°C for 100 minutes in stagnant air, using average B concentration (ICP-OES) to determine the average diffusion coefficient.) A majority of the borosilicate glass is shown to have sufficient B_2O_3 concentration to be liquid at the oxidation temperature.

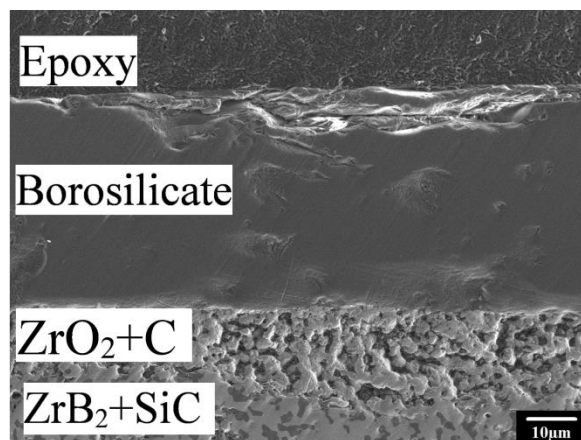


Figure 63. Cross-sectional view of ZrB_2 -30 vol% SiC oxidized at 1500°C for 100 minutes in stagnant air with a nearly uniform oxidation front between ZrB_2/SiC and the oxides.

Implications for Oxidation

It is emphasized here that considerable B_2O_3 is retained in the glass layer which has important effects on oxidation, assuming the rate limiting step is oxygen diffusion in the borosilicate glass layer^{19, 30}. Chapter 1 shows the B_2O_3 - SiO_2 phase diagram (Figure 2)⁹⁴. At 1500°C, the liquidus curve lies at approximately 95 mol% SiO_2 . The surface of the glass layer depleted in B_2O_3 will be solid whereas the interior of the glass layer with higher B_2O_3 content will be liquid of decreasing viscosity towards the base material. The calculated average B diffusion coefficient is much lower than the $10^{-6} \text{ cm}^2/\text{sec}$ for O_2 diffusion through borosilicate glass obtained by extrapolating Schlichting's results to 1500°C³⁰. Temperature effects on oxygen transport will thus be very complex. Increasing temperature depletes the borosilicate glass in B_2O_3 , slowing oxygen transport by compositional effects at the surface, but at the same time increases oxygen transport since it is an activated process. The apparent activation energy then reflects some combination of B_2O_3 vaporization, B_2O_3 transport outward due to the driving force induced by the B_2O_3 concentration gradient, and oxygen transport inwards in the non-uniform glass structure.

Oxygen Diffusion Pathways- Double Oxidation Experiments

1500°C

After oxidation at 1500°C for 10 minutes in $^{16}O_2$ and 9 minutes in $^{18}O_2$, the tracer ion is seen throughout the borosilicate scale. This result indicates that either network diffusion in the borosilicate glass is responsible for oxygen transport or that a combined permeation/exchange process occurs. $^{18}O_2$ is also seen in the ZrO_2 grains in the ZrO_2+C layer (Figure 57), indicating that $^{16}O_2$ in the ZrO_2 has also exchanged with the $^{18}O_2$. Exchange in the ZrO_2 grains throughout the scale thickness indicates oxygen transport in ZrO_2 is significant at this temperature, on the order of $10^{-10} \text{ cm}^2/\text{sec}$. However, no new ZrO_2 oxide enriched with $^{18}O_2$ was observed, indicating

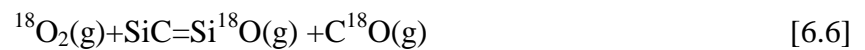
electronic transport may limit oxide growth. This result agrees with the current model of ZrB₂-SiC oxidation, which assumes that the oxygen transport in ZrO₂ can be neglected for <100ppm dopants and only diffusion through the borosilicate glass and pores is allowed^{26, 34, 95}. For >100ppm of dopants, oxygen diffusion is known to be rapid, though electronic transport is still slow⁹⁵. The lack of a gradient in the ¹⁸O₂ throughout the oxide further supports exchange within both the borosilicate and ZrO₂ grains.

1650°C

After oxidation at 1650°C for 29 minutes in ¹⁶O₂ and 45 seconds in ¹⁸O₂, the ¹⁸O₂ was found on the very outside of the borosilicate layer and along the base material/oxide interface. This indicated that a combination of network exchange at the surface and permeation through the borosilicate glass control the oxygen diffusion, in agreement with the literature for SiC oxidation^{55, 59, 60}. In addition, extrapolation of Schlichting's oxygen diffusion rate to 1650°C (5x10⁻⁶cm²/sec), does allow for ¹⁸O₂ to have permeated through 100µm of oxide in 45 seconds³⁰. The presence of the ¹⁸O₂ in the borosilicate glass at the interface with the depletion layer is consistent with this borosilicate forming when the SiC grains at the bottom of the depletion layer actively oxidized to SiO(g) (Reaction 2b), which then permeated up through the pores. This is shown schematically in Chapter 5 (Figure 49.) Figure 64 provides a schematic of two possible reactions for incorporation of ¹⁸O₂ into the borosilicate formed just above the depletion layer. Either ¹⁸O₂ reacts with SiO(g) to form SiO₂ via:



Or ¹⁸O₂ is responsible for the active oxidation reaction via:



And the SiO(g) subsequently reacts with O₂(g) to form SiO₂ (Reaction 2.1.)

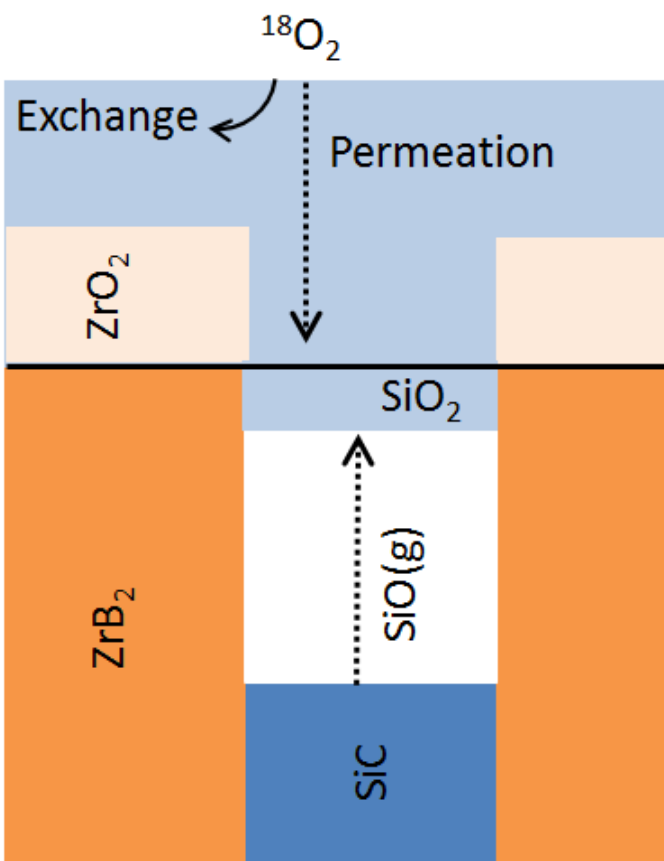


Figure 64. Schematic of $^{18}\text{O}_2$ diffusion through the borosilicate glass to form new SiO_2 at the $\text{ZrO}_2/\text{ZrB}_2$ interface.

The ^{18}O distribution in the borosilicate glass was found to be non-uniform after both the short and long $^{18}\text{O}_2$ exposures (Figure 58 and Figure 61.) While this could be an artifact of the technique, the uniformity of the total ion count suggests that surface roughness does not account for the differing ^{18}O intensities observed in some locations. If the ^{18}O concentration in the borosilicate glass is actually non-uniform, regions of the glass must have a higher exchange rate of oxygen. Karlsdottir et al. suggest compositional variations in the borosilicate glass occur due to localized formation of B_2O_3 and varying ZrO_2 solubility in borosilicate glass with B_2O_3 content⁷⁶. Variation in B_2O_3 content of the borosilicate glass has been shown already with

changes of depth into the oxide, as described above. B_2O_3 content has also been shown to have a high impact on oxygen diffusion rates through borosilicate glass³⁰. Thus, glass regions higher in B content would have more ready access to $^{18}O_2$ and would likely exchange with $^{18}O_2$ earlier than silica rich regions. However, ^{18}O -rich regions of the borosilicate glass were not found to contain more B relative to ^{18}O -poor regions within the sensitivity of EDS.

By careful observation of the intensities of ^{18}O throughout the oxide layers of the specimen oxidized at 1650°C for 45 minutes in $^{16}O_2$ and 5 minutes in $^{18}O_2$, a qualitative change in tracer concentration between the borosilicate glass and the ZrO_2 phases is noted, Figure 65. The ToF-SIMS map taken near the top of the oxide scale shows a higher ^{18}O intensity in the ZrO_2 grains relative to the borosilicate glass. The ToF-SIMS map taken near the depletion region/bottom of the oxide scale shows a lower ^{18}O intensity in the ZrO_2 relative to the borosilicate glass. This indicates that the ZrO_2 grains lower in the scale have undergone less complete exchange than the ZrO_2 grains at the surface. This reveals that $^{18}O_2$ exchange with ZrO_2 is not as rapid as that of the borosilicate glass.

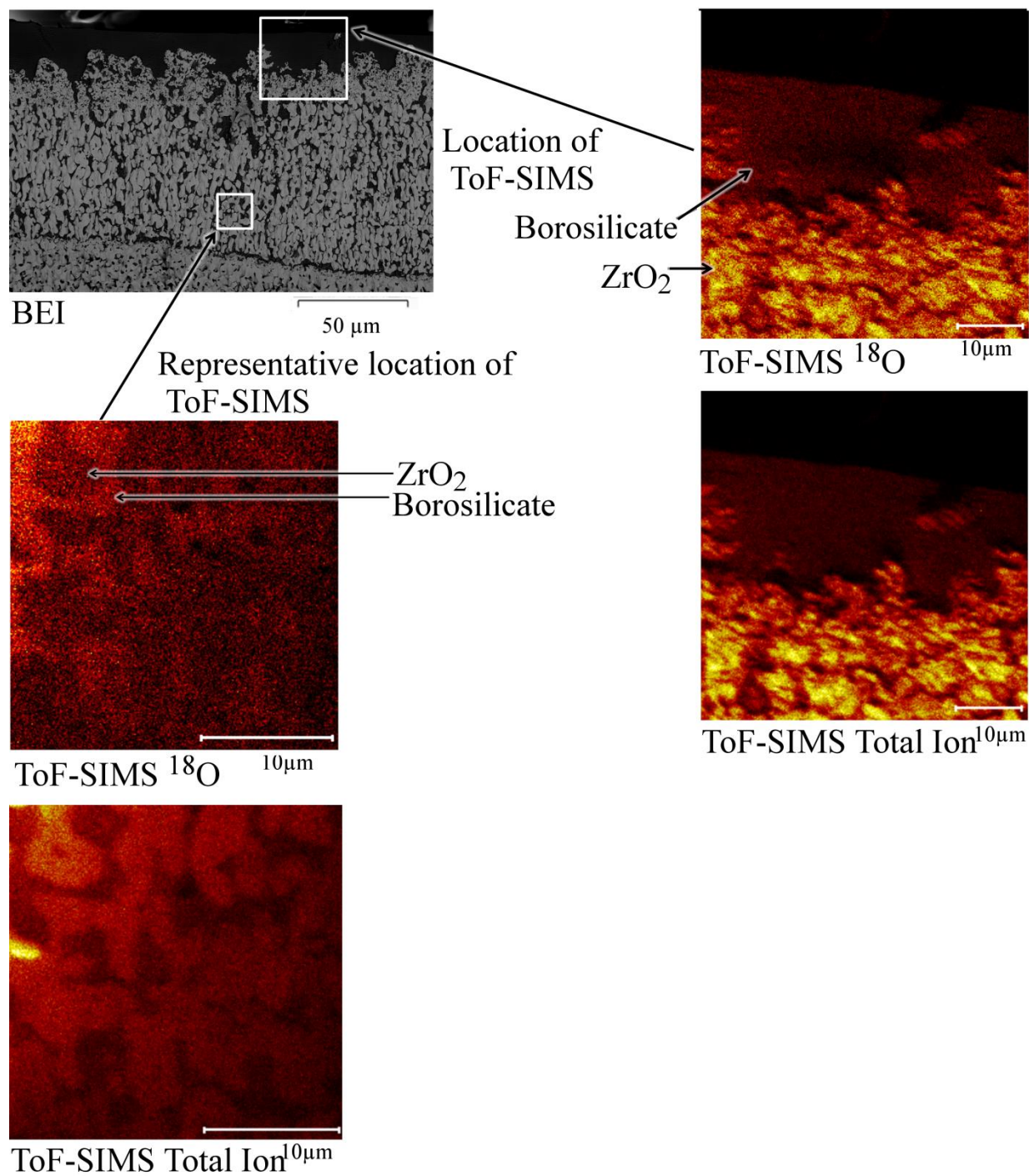


Figure 65. SEM/ToF-SIMS results for ZrB₂-30 vol% SiC oxidized at 1650°C for 45 minutes in ¹⁶O₂ and 5 minutes in ¹⁸O₂, showing change of ¹⁸O contrast from brighter in ZrO₂ near surface to brighter in borosilicate near ZrO₂/ZrB₂ interface. The total ion count is included to show lack of microstructural influence.

Conclusions:

Significant B_2O_3 remains (27-43mol%) in the borosilicate scale formed during oxidation of ZrB_2 -30 vol% SiC at temperatures between 1300°C and 1500°C. Borosilicate compositions measured using ICP-OES (average value), EDS & XPS were used to estimate B diffusion coefficients in the borosilicate ranging from $10^{-10} \text{ cm}^2/\text{sec}$ to $10^{-13} \text{ cm}^2/\text{sec}$ for B_2O_3 rich and SiO_2 rich portions of the scale. The variation in B concentration across the oxide scale implies variations in T_m , D_B , and D_O through the thickness of the scale and a resulting complex temperature dependence for oxygen permeation leading to oxidation of ZrB_2 -SiC.

ToF-SIMS results after $^{16}O_2$ - $^{18}O_2$ double oxidation experiments have shown that oxygen exchange and diffusion is rapid in both the borosilicate glass and the ZrO_2 grains at 1500°C (10 minutes, 9 minutes oxidation). At 1650°C, 45 seconds exposure to $^{18}O_2$ after $^{16}O_2$ oxidation demonstrated that permeation was more rapid than exchange. Oxygen exchange with the borosilicate glass may be compositionally dependent, but further work is required to confirm this. Oxygen transport was shown to be non-negligible in ZrO_2 and should be considered in ZrB_2 -SiC oxidation models.

Recommendations for Future Work:

1. Further investigation of the borosilicate glass composition, especially at temperatures above 1500°C, is important for high-temperature application of this material. This study was limited by the small size of the hot zone during resistive heating, which did not provide sufficient borosilicate glass formed at a constant temperature for ICP-OES analysis.
2. A more systematic study of the oxygen diffusion pathways using $^{16}O_2$ - $^{18}O_2$ double oxidation experiments is required. This work was limited by available time on the ToF-

SIMS and access to the necessary sectioning tools. With extended time on both systems, a more thorough analysis of the diffusion pathways could be obtained. The question of uneven distribution of the $^{18}\text{O}_2$ through the borosilicate glass which could be due to a compositional variation in the borosilicate glass still remains. In addition, no ZrO_2 grains at the $\text{ZrO}_2/\text{ZrB}_2$ interface containing high concentrations of $^{18}\text{O}_2$, as would be expected for new oxide growth, were seen under any of the tested conditions. Suggested experiments include:

- a. 1500°C for 19 minutes $^{16}\text{O}_2$ and 45 seconds $^{18}\text{O}_2$, to differentiate between exchange and permeation at 1500°C
 - b. 1500°C for 45 minutes and 2 minutes, to observe ZrO_2 grains before they have fully exchanged with the $^{18}\text{O}_2$ at 1500°C
 - c. 1500°C for 30 minutes and 10 minutes to observe the growth of new ZrO_2 grains and resolve the diffusion pathway through the ZrO_2+C layer at 1500°C
 - d. 1650°C for 45 minutes and 2 minutes to observe ZrO_2 grains before they have fully exchanged with the $^{18}\text{O}_2$ at 1650°C
 - e. 1650°C for 30 minutes and 10 minutes to observe the growth of new ZrO_2 grains at 1650°C
3. Separate work is needed to determine the solubility of B_2O_3 in warm water, as the literature has conflicting results. This could be done using free standing sol-gel derived borosilicate glasses. However, this work would not be entirely conclusive since structural differences may exist between thermally grown and sol-gel derived borosilicate glasses.

Chapter 7 Considerations for Future Modeling and Application of ZrB₂-SiC

Comparison of Findings to Assumptions in Existing Life Prediction Models

The most rigorous life prediction model for ZrB₂-SiC in the literature was produced by Parthasarathy et al. and uses a number of assumptions based upon available data in the literature for oxidation of this material ²⁶. The validity of each of the assumptions is discussed with regards to the new findings of this work.

1. The microstructure assumed is the same as that presented in Chapter 5 for oxidation above 1627°C, with borosilicate glass filling in the regions between ZrO₂ grains. This work has shown a different, second microstructure is found when oxidation occurs below 1627°C, and this must be accounted for in future models.
2. ZrO₂ grains are assumed to be impermeable to oxygen when less than 100ppm of dopants are present. This work has shown oxygen permeation through ZrO₂ at a rate of at least 10⁻¹¹ cm²/sec (on the same order as B diffusion through the borosilicate glass), though the dopant concentration is not known.
3. Molecular oxygen is assumed to diffuse and permeate through the borosilicate glass. The ToF-SIMS results for oxidation in ¹⁸O₂ for 45 seconds after ¹⁶O₂ oxidation at 1650°C support this assumption.
4. CO(g) is assumed to diffuse or bubble out through the borosilicate glass and not be rate limiting for oxidation. This work also suggests that CO(g) bubbles through the borosilicate glass at T>1627°C.
5. The monoclinic to tetragonal transition of ZrO₂ is assumed to impact oxidation behavior. This transition occurs at ~1205°C, below the temperatures studied here.

6. The borosilicate glass thickness is assumed to be affected by viscous flow. This work only addressed glass viscosity at 1500°C, where viscous flow on a macro-scale was found to be negligible.
7. The model assumed an infinitesimal amount of oxide to exist at an infinitesimal start time. The short term exposure tests performed here support this assumption, having shown both ZrO₂ and borosilicate glass on the surface in as little as 10 seconds at 1500°C.
8. The concentration of B₂O₃ on the surface of the borosilicate glass is assumed to be a constant fraction of the interior composition. This work has shown that the B₂O₃ on the surface at 1500°C changes with oxidation time (10 minutes versus 100 minutes), although the average concentration is similar after tests of 100 minutes and 221 minutes. In addition, temperature dependence of borosilicate composition should be considered.

Considerations for Future Application

This work has quantified a number of degradation mechanisms of ZrB₂-30 vol% SiC due to oxidation at high temperatures, that decrease its usefulness in long term hypersonic applications. Based on the new results and information in the literature strategies for improving oxidation resistance of ZrB₂-SiC are evaluated.

1. SiC depletion was found in ZrB₂-30 vol% SiC after oxidation at temperatures of 1627°C and higher. The formation of a porous depletion layer due to active oxidation of SiC will lead to a decrease in mechanical properties when use temperatures exceed 1627°C. A lower SiC content could be used, which would decrease the interconnectivity of the SiC grains, preventing SiC depletion^{13, 35}. However, this would increase the B₂O₃ content of

the borosilicate glass, increasing oxygen diffusion through the protective outer oxide scale.

2. Higher concentrations of B_2O_3 increase oxygen diffusion through borosilicate glass. To decrease the B_2O_3 content of the borosilicate glass, starting materials such as $ZrC+SiC$ or $ZrN+SiC$ could be used ¹⁴. However, this would increase the gas formation ($CO(g)$ and $N_2(g)$), decreasing the protective abilities of the silicate scale.
3. Oxygen permeation through ZrO_2 was found to be non-negligible. Doping with 5+ cations (Ta and Nb) would decrease oxygen vacancies in the ZrO_2 , thus decreasing oxygen permeation ¹⁵. However, this would create oxides with lower melting points (Ta_2O_5 $T_m=1872^\circ C$, Nb_2O_5 $T_m=1512^\circ C$), decreasing the use temperature of the material.
4. The borosilicate glass has been found to provide insufficient oxidation protection. ZrB_2+WO_3 could be used with no SiC addition ⁹⁶. This material would result in a denser ZrO_2 scale due to liquid phase sintering. However, while this may give a slight increase in application temperatures, the self-healing ability of the borosilicate scale would be lost. In addition, the D_O in ZrO_2 is still too high for long term oxidation protection.

Thus, overall this material is not suitable for long term applications at ultra-high temperatures, but still is of interest for short term single-use applications.

Chapter 8 Conclusions

This work has dramatically improved the understanding of the oxidation mechanisms and kinetics of ZrB_2 -30 vol% SiC at temperatures of 1300°C to 1800°C. A quantitative study of the oxidation behavior was performed in order to improve life prediction modeling. Oxidation was quantified by mass change and oxidation product layer thicknesses. A combination of scanning electron microscopy, energy dispersive spectroscopy, x-ray diffraction, x-ray photoelectron spectroscopy, inductively coupled plasma optical emission spectrometry, and time of flight secondary ion mass spectrometry was used to characterize the oxidation products.

Two oxidation regimes were identified, low temperature oxidation below 1627°C and high temperature oxidation at and above 1627°C; this transition is not considered in current oxidation models. Transition between the low and high temperature oxidation regimes is explained here using thermodynamics considering a locally SiC-rich microstructure.

Low temperature oxidation ($T < 1627^\circ\text{C}$) of ZrB_2 -30 vol% SiC formed a two layer oxide which consisted of a borosilicate glass layer above a $\text{ZrO}_2 + \text{C}$ layer. Variation in oxidation kinetics was observed and several mechanisms were explored to explain the variability. Viscous flow on a macro-scale and surface roughness were found to have minimal impact on oxidation at 1500°C. The initial stages of oxidation at 1500°C were explored for the first time to try to understand any relationship to the variable performance oxidation observed at longer times. It was shown that borosilicate glass and ZrO_2 formation began as early as 10 seconds when oxidation was performed at 1500°C but initial stage oxidation did not have a clear impact on distribution of oxide phases observed at longer times. A mechanism linking bubble formation in the borosilicate glass to oxide variability was proposed. In addition, it was shown that oxidation

tests >4 hours did not accurately predict material recession at longer times and a maximum attack rate should be considered for future life prediction models.

The composition of the borosilicate glass formed at temperatures of 1300°C to 1500°C was determined and found to contain significant amounts of B₂O₃ (27-43mol%), except at the very surface of the oxide. The effects of high B₂O₃ contents on oxygen transport inward must be considered in life prediction models. Double oxidation experiments using ¹⁶O₂ and an ¹⁸O₂ tracer indicated oxygen exchanged with both the borosilicate glass and the ZrO₂ grains. Both the presence of C in the ZrO₂ layer, instead of the expected borosilicate glass, and the oxygen diffusion in tetragonal ZrO₂ grains must be considered in life prediction models for ZrB₂-SiC.

High temperature oxidation ($T \geq 1627^\circ\text{C}$) of ZrB₂-30 vol% SiC resulted in a three layer microstructure. A borosilicate glass layer was found above a layer with ZrO₂ and borosilicate glass. Beneath these was a porous layer of ZrB₂ resulting from SiC depletion due to active oxidation to SiO(g). This oxidation regime was found to have much more rapid ZrO₂ oxide layer growth than the low temperature regime, attributed to a less protective glass layer. The time and temperature conditions for the formation of the porous layer due to SiC depletion were determined. The growth of the depletion layer was explained using parabolic gas diffusion limited active oxidation of SiC, again considering local thermodynamics. Double oxidation experiments using ¹⁶O₂ and an ¹⁸O₂ tracer indicated that the oxygen initially permeated through and then exchanged with the borosilicate glass and exchanged with the ZrO₂ grains in this oxidation regime as well. Variation in the composition of the borosilicate glass is proposed to explain uneven exchange of the ¹⁸O₂ through the scale, though this requires confirmation.

Through this better understanding of the oxidation mechanisms of ZrB₂-30 vol% SiC and the thermodynamics and kinetics of the oxidation reactions, improved life prediction modeling is

possible. It is concluded that the poor oxidation resistance of ZrB_2 -30 vol% SiC and related UHTCs limits long term reusable application of this class of materials.

Appendices:

Appendix 1: Resistive Heating System

Obstacles Overcome

While this experimental set up is based off the “ribbon method” designed by Karlsdottir, a number of design changes have been made and difficulties overcome during setup³¹. The main design change was to enclose the heating system in a small chamber (outside dimensions 7cm x 7cm x 7cm) to allow for control of the environment and minimize use of $^{18}\text{O}_2$ during double oxidation experiments.

To begin with, both ends of the specimen sat inside an inset in copper pieces attached to the current feedthroughs. These insets were lined with silver foil and the specimen either remained in place due to gravity and pressure from the sides or was held down with silver foil over top, see Figure 66a. However, this design led to cracking along the bottom edges of the specimen, most likely due to thermal expansion of the copper holder and specimen during test runs. This holder was then replaced with flat copper blocks, Figure 66b and c. The specimen was first held in place by silver foil clamped around the specimen, which did not work due to the heating of the screws. Then the specimen was held by Maycor clamps, however these stiffer clamps required precise alignment of the copper blocks to prevent torque on the specimen as the clamps were tightened into place. When the copper was misaligned, the torque caused the thin bridge of the specimens to snap. Next, the copper blocks were replaced by wire braid, to which the specimen could be clamped using alligator clips, and which did not put any pressure on the corners or torque on the bridge. Initially, the braid used was tin plated copper; however this was found to melt during test runs and was replaced with pure copper braid. At higher temperatures and longer times, the copper braid oxidized too greatly to conduct electricity, and had to be

replaced with copper wire (12AWG) which was flattened to 1.05mm thick x2.85mm wide using a rolling mill. This was found to be the most successful holding method (Figure 67.)

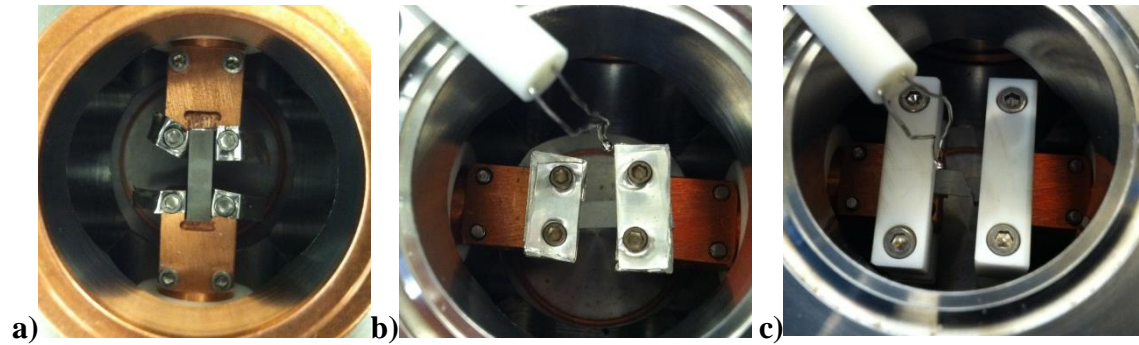


Figure 66 a) Initial specimen holder using copper blocks with insets. b) Flat copper specimen holder with silver foil clamps. c) Flat copper specimen holder with Maycor clamps.

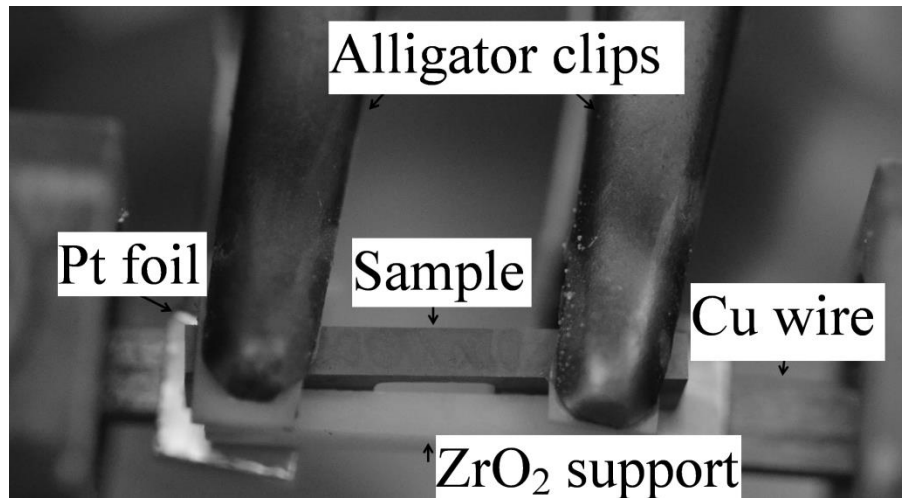


Figure 67. Final holding arrangement for ZrB_2 -30 vol% SiC bridge specimen in resistive heating system. Cu wire feeds the current into the system, Pt foil prevents reaction of copper wire with hot specimen, ZrO_2 supports prevents specimen snapping upon insertion due to torque. Specimen is held in place using alligator clips.

Issues of melting were also encountered with the silver foil which, following Karlsdottir, was placed between the specimen and copper specimen holder to prevent oxidation of the copper. Due to the heat load on the thicker ends of the specimens, the silver foil melted in tests exceeding $\sim 1200^{\circ}\text{C}$ in this lab, and led to the melting of the copper braid. The silver foil was therefore replaced with platinum foil, with the higher melting temperature of 1768°C .

In order to provide greater stability against torque caused by the weight of the alligator clips, a ZrO_2 support was superglued to the side of the bridge specimens, connecting the two legs, and not touching the thin bridge section. This allowed for more consistent insertion into the system without breaking. It also seemed to decrease shifting of the specimen during the test, which lead to dropping emissivity and possibly incorrect temperature readings.

Another issue frequently faced in the design of these experiments was good electrical contact for the specimen. This was the reason for initially using the copper with niches and then trying different clamps for the flat copper pieces. Upon switching to the copper braid, alligator clips were used to hold the specimen in place. However, the small flat mouthed alligator clips used for the first few runs heated up during tests and lose their clamping abilities. These were therefore replaced with larger clips, which had teeth. The larger size prevented loosening due to heating, but the teeth caused uneven pressure and therefore uneven electrical contact along the specimen. Therefore, the teeth were ground off to provide the best contact. The clips still overheated due to electrical current running through them. To prevent this, 0.8mm thick sheets of Maycor (a glass-mica ceramic, McMaster-Carr, Robbinsville, NJ) or stabilized ZrO_2 (Ceramic Technologies, Inc, Houston, TX) were super glued to both inner sides of the alligator clips.

To begin with, the specimens were machined to be 15mm long x 4mm wide x 3mm tall, with a 0.5mm thick bridge 3.5mm long. However, after solving the issues of holding, melting

and electrical contact, it was found that a maximum temperature of $\sim 1200^{\circ}\text{C}$ could be achieved for these specimens with the full current capabilities ($\sim 120\text{Amps}$) of the control unit and transformer. As increasing the current was not feasible, the bridge specimens were cut in half lengthwise to $\sim 1.5\text{mm}$ wide, decreasing the cross-section of material through which the current passed. This allowed temperatures as high as 2200°C to be achieved.

Once it was shown that ultra-high temperatures could be achieved in this system, the control unit was programmed to output the correct current to achieve a quick temperature rise and then a steady hold temperature, without excessive overshoot. This was done using the auto-tune function of the PID controller. Several testing iterations were made, first using NiCr wire, then $\text{ZrB}_2\text{-30vol\%SiC}$ which was 4mm wide and then with the desired specimens of $\text{ZrB}_2\text{-SiC}$. It was found that the best heating to temperatures of 1500° and below was performed with a Proportional Band of 1040, Integral Time of 3 seconds, and the Derivative Time turned off. For higher temperatures, a Proportional Band of 2496, Integral Time of 15 seconds, and the Derivative Time turned off, worked better. Both Low and High Cutback were left to auto settings for all tests.

Condensation of $\text{B}_2\text{O}_3(\text{g})$ on the viewing window of the chamber was another obstacle. When the specimens were heated above $\sim 1200^{\circ}\text{C}$, B_2O_3 volatilized out of the material and a white film formed on the window, preventing accurate reading by the pyrometer. This was prevented by flowing $\text{O}_2(\text{g})$ through the chamber at a rate of 900sccm. The $\text{O}_2(\text{g})$ flowed through drierite (CaSO_4) to minimize possible effects from humidity.

Pyrometry

A note should be made here about the temperature reading of the pyrometer. The pyrometer used is a Pyrofiber Lab Pyrometer which uses emissivity values measured during testing to correct the temperature reading. When observing the emissivity values throughout the tests, for some tests the emissivity stayed fairly constant in the 0.80-0.99 range, while for other tests it dropped during the test, in some cases as low as 0.05-0.20. This drop in emissivity seemed to correlate with tests where the oxide thickness results were slightly different and was likely due to a twisting of the specimen inside of the system. Consistent positioning of the specimen and strengthening using the ZrO_2 support assisted in preventing this.

It is also well known that pyrometer temperature readings are not as well trusted as those of thermocouples⁸³. Standard one-color pyrometers are greatly affected by changing emissivity values. Two-color pyrometers, which are designed to account for some changing emissivity, are still found to be up to 100°C off from thermocouple readings during initial oxide formation when the oxide layer is <2µm thick⁸². The use of an emissivity-correcting pyrometer here, and the knowledge that the oxide layer quickly reaches thicknesses greater than 2µm, should lead to more accurate measurement of the temperature. This is reinforced by the similar behavior seen between box furnace and resistive heating results at 1500°C, as is discussed in Chapter 3.

Appendix 2: Resistive Heating Testing Conditions

Specimen	Time (minutes)	Notes	Set temperature (°C)	Average actual temperature (°C)	Standard deviation of temperature (°C)	Emissivity behavior
Bridge 18	10		1300	1296	4	steady
Bridge 19	10		1500	1499	14	dropping
Bridge 57	10		1500	1499	22	wide spread
Bridge 58	10		1500	1499	5	steady
Bridge 46	20		1500	1506	14	steady
Bridge 53	19	10 ¹⁶ O ₂ 9 ¹⁶ O ₂	1500	1507 1503	15 13	steady
Bridge 76	19	10 ¹⁶ O ₂ 9 ¹⁸ O ₂	1500	1503 1501	14 19	steady
Bridge 80	20	15 ¹⁶ O ₂ 5 ¹⁸ O ₂	1500	1505 1498	12 16	steady
Bridge 89	20	19 ¹⁶ O ₂ 1 ¹⁸ O ₂	1500	1500 1503	20 14	steady
Bridge 67	55		1600	1614	24	steady
Bridge 49	40		1627	1638	27	wide spread
Bridge 52	60		1627	1636	30	wide spread
Bridge 50	70		1627	1625	10	steady
Bridge 74	10		1650	1671	43	wide spread
Bridge 84	10		1650	1648	17	dropping
Bridge 85	20		1650	1656	21	wide spread
Bridge 93	30	29 ¹⁶ O ₂ .75 ¹⁸ O ₂	1650	1653 1607	19 64	steady
Bridge 81	35		1650	1651	23	dropping
Bridge 68	45		1650	1659	26	steady
Bridge 69	50		1650	1666	28	steady
Bridge 79	50	45 ¹⁶ O ₂ 5 ¹⁸ O ₂	1650	1649 1648	11 13	dropping
Bridge 63	55		1650	1651	15	dropping
Bridge 73	60		1650	1649	13	wide spread
Bridge 72	70		1650	1659	28	steady
Bridge 20	10		1700	1699	25	dropping
Bridge 38	15		1700	1702	30	steady
Bridge 28	20		1700	1698	37	dropping
Bridge 45	20		1700	1700	22	steady
Bridge 37	25		1700	1701	26	steady
Bridge 32	30		1700	1699	14	steady

Bridge 61	30		1700	1702	16	dropping
Bridge 42	35		1700	1699	15	steady
Bridge 56	35		1700	1699	23	steady
Bridge 25	40		1700	1698	13	steady
Bridge 70	40		1700	1699	10	steady
Bridge 41	5		1800	1797	53	wide spread
Bridge 33	10		1800	1798	52	wide spread
Bridge 54	10		1800	1815	58	increasing
Bridge 43	15		1800	1814	41	steady
Bridge 62	15		1800	1819	38	steady
Bridge 36	20		1800	1797	24	steady

Note 1: all tests performed in $^{16}\text{O}_2$ flowing at a rate of 900sccm unless otherwise noted.
Note 2: steady indicates emissivity constant around 0.90 (± 0.09), wide spread indicates emissivity ranged from 0.60 to 0.99 throughout test, dropping indicates emissivity continuously fell throughout test.

Table 14. Resistive heating test conditions.

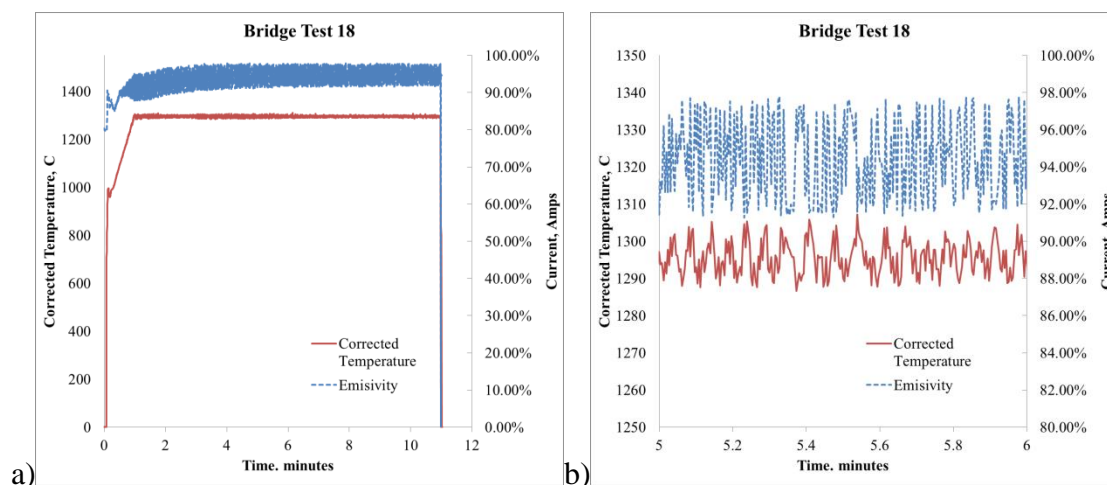


Figure 68. Plot of emissivity and temperature versus current for ZrB_2 -30 vol% SiC specimen oxidized at 1300°C for 10 minutes a) at full scale b) showing the scatter in the temperature and emissivity measurements.

Appendix 3: Casino Simulation for B Concentration Determined by Energy Dispersive Spectroscopy (Performed by Siying Liu)

The Casino simulation program was used to determine the EDS sampling depth into the borosilicate glass formed during oxidation of ZrB₂-30 vol% SiC at 1500°C for 100 minutes. A series of layers were built using the compositional data determined both from XPS and EDS and the density data from Bruckner et al ⁷⁰.

The sampling volume for the EDS was determined by building a layered borosilicate structure. The first layer was set to be 50nm thick with a composition of 6.1mol% B₂O₃ (remainder SiO₂) from averaging the XPS results for the surface and 50nm into the borosilicate. This composition has a density of 2.21g/cm³. The next 100 nm was assumed to have a composition of 8.8% B₂O₃ (remainder SiO₂) from averaging XPS results acquired at 50nm and 150nm depth, with a corresponding density 2.18g/cm³. The next three layers were assumed to have a composition of 12.98mol%, 18.67mol%, and 30.96mol% B₂O₃ (remainder SiO₂) respectively. These compositions were determined from mol% B and Si measured by EDS using acceleration voltages of 5kV, 10kV and 20kV. The last three layer thicknesses were determined and adjusted using an iterative process to determine the average sampling depth for each accelerating voltage. Table 15 provides the layer information used to generate the Casino simulations. The three Casino simulations of the sampling volume at 5kV, 10kV, and 20kV based on final iterations of the layered structures are shown in Figure 69 through Figure 71. The final depth for each acceleration voltage was determined using plots of depth versus hits, as given in Figure 72.

Layer	Thickness (nm)	Total depth (nm)	Measured B concentration (at%)	Composition (mol% B ₂ O ₃)	Assumed density (g/cm ³)	Source
1	50	50	0.1, 3.8	6.10	2.21	XPS at surface and 50nm
2	100	150	3.8, 5.43	8.80	2.18	XPS at 50nm and 150nm
3	70	220	7.6	12.98	2.15	EDS, 5kV
4	550	770	11	18.67	2.12	EDS, 10kV
5	2130	2900	18.5	30.96	2.06	EDS, 20kV

Table 15 Layer information used in Casino simulations for EDS penetration depth determinations of borosilicate glass formation on ZrB₂-30 vol% SiC after oxidation at 1500°C for 100 minutes in stagnant air in standard box furnace.

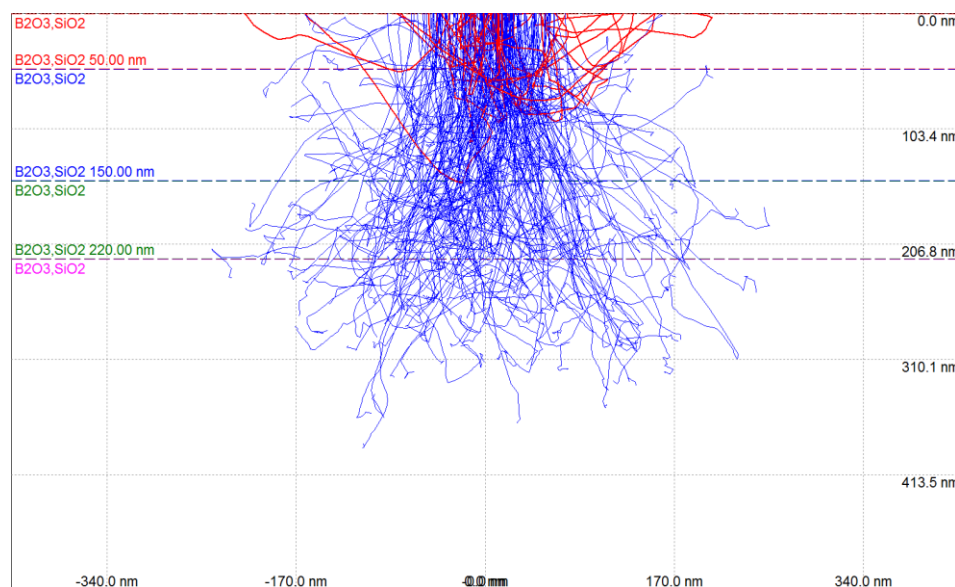


Figure 69. Casino simulation showing sampling volume in borosilicate glass formed on on ZrB₂-30 vol% SiC after oxidation at 1500°C for 100 minutes in stagnant air in standard box furnace for an accelerating voltage of 5kV.

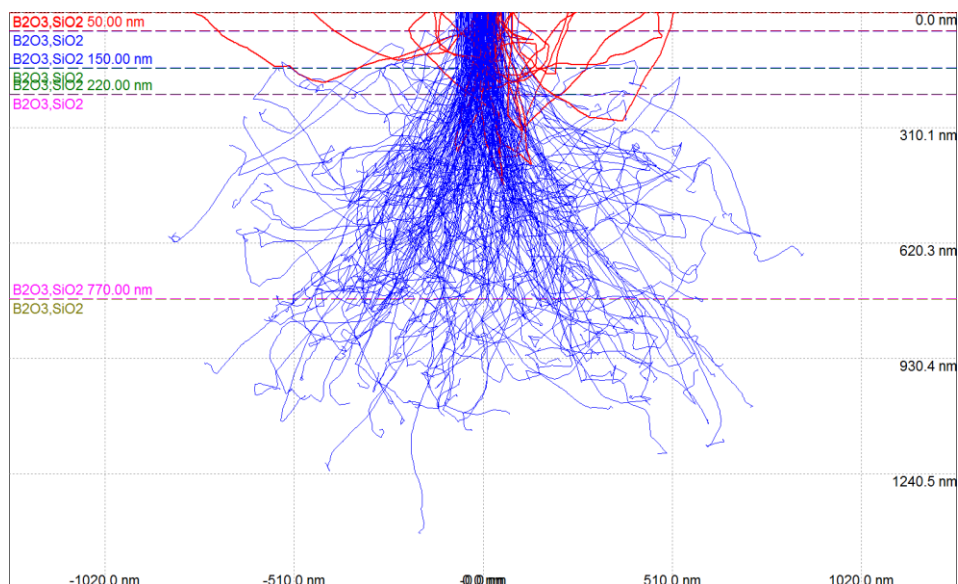


Figure 70. Casino simulation showing sampling volume in borosilicate glass formed on ZrB_2 -30 vol% SiC after oxidation at 1500°C for 100 minutes in stagnant air in standard box furnace for an accelerating voltage of 10kV.

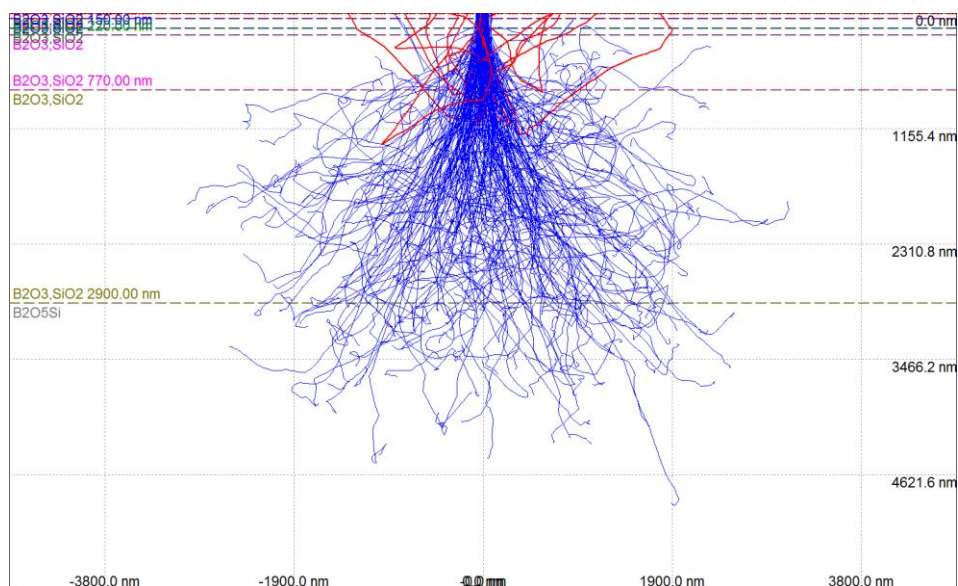


Figure 71. Casino simulation showing sampling volume in borosilicate glass formed on ZrB_2 -30 vol% SiC after oxidation at 1500°C for 100 minutes in stagnant air in standard box furnace for an accelerating voltage of 20kV.

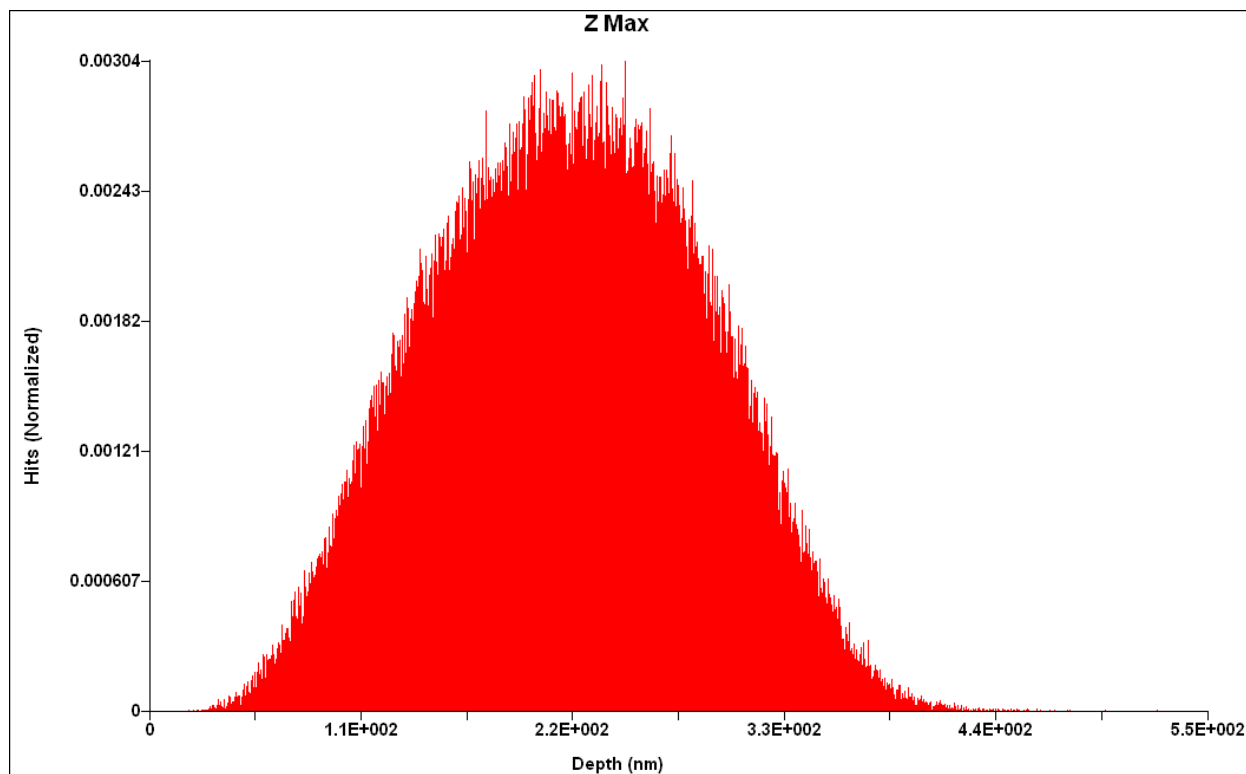


Figure 72. Casino simulation of depth versus normalized hits generated for 5kV in the simulated borosilicate glass.

Appendix 4: Inductively Couple Plasma Optical Emission Spectrometry (Performed by Forrest Craven, Siying Liu, Bohuslava McFarland)

Experimental

A baseline oxidation test was conducted at 1500°C for 100 minutes. Parabolic oxidation kinetics were assumed, in which mass change follows the relationship:

$$t = \frac{(\Delta wt/SA)^2}{k} \quad [A4.1]$$

where t is the exposure time, Δm is the oxidation mass change, SA is the measured surface area, and k_p is the measured parabolic oxidation rate constant. The exposure times necessary to create the same mass gain as the 1500°C 100 minute specimen were determined for temperatures of 1300°C and 1400°C by calculating the numerator of Equation [A4.1] and using k_p values of 5.19mg²cm⁴/h and 4.05mg²cm⁴/h, respectively. Exposure times of 221 minutes and 128 minutes were calculated for 1300°C and 1400°C, respectively. Specimens were exposed at these time and temperature conditions to provide three specimens with approximately the same mass gain (and approximately the same oxide thickness), but different oxidation temperatures. Specimens were also exposed for 221 minutes at 1400°C and 1500°C to provide a series of specimens exposed for the same *time* at 1300°, 1400°, and 1500°C. Three trials of each of these tests were conducted to evaluate variability of the results. One bar of material was used for each of the three trials for consistency within each trial.

Following mass change measurements, each specimen was placed in a test tube filled with 15mL DI H₂O maintained at 35°C for 24 hours to remove water soluble B₂O₃. The specimen was then removed, dried via evaporation at room temperature and weighed. The DI H₂O solution was retained for analysis. The specimen was then placed in another test tube also filled with 15mL DI H₂O maintained at 35°C for 24 hours. The second leaching was conducted

to confirm that the bulk of the water-soluble B_2O_3 was removed during the first H_2O soak⁷⁰.

Again, the specimens were removed and dried and the DI H_2O solution was retained for analysis. After the second leaching bath, each specimen was placed in an HF acid solution (48%-51% HF in H_2O) at 35°C for 24 hours to dissolve remaining SiO_2 . In the first trial, the specimens were placed in 3ml of HF solution for 24 hours and then diluted with 12mL of DI H_2O . In the second and third trials, the specimens were soaked in a solution of 12mL of DI H_2O plus 3ml of HF solution at 35°C for 24 hours. The specimens were removed and dried and the HF solutions were retained for analysis. A very minimal, ~0.05 mL, amount of solution was lost at each removal of the specimen and was unavoidable.

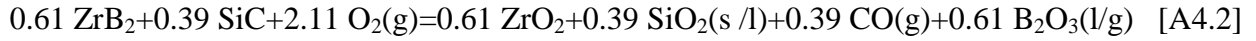
The three solutions for all specimens were analyzed for B and/or Si using Inductively Coupled Plasma Optical Emission Spectrometry (ICP-OES, Thermo-Scientific, Waltham, MA), which has a detection limit on the order of 1ppb for most elements. The purity of the DI H_2O gives an experimental detection limit of 3ppb for Si. Precise composition measurements were made by comparison of the emission spectra from each solution to prepared standards of known concentrations and normalization with an internal yttrium standard. The standards were prepared using solutions of B and Si with concentration of 1 ppm, 10 ppm, and 100 ppm. B and Si quantities were determined in the H_2O solutions, but only Si quantities were determined in the HF solutions, since ZrB_2 dissolves in HF solutions, as observed by Scanning Electron Microscope (SEM, 6700F, JEOL, Tokyo, Japan) and described later. The total mass of all oxidation products ($ZrO_2(s)$, $B_2O_3(l,g)$, $SiO_2(s,l)$ and $CO(g)$) was calculated by adding the observed mass gained from oxidation and the calculated vaporized mass of both $B_2O_3(g)$ and $CO(g)$ together. The vaporized mass was calculated using the stoichiometric relation from:

$$0.61 ZrB_2 + 0.39 SiC + 2.11 O_2(g) = 0.61 ZrO_2 + 0.39 SiO_2(s/l) + 0.39 CO(g) + 0.61 B_2O_3(l/g) \quad [A4.2]$$

(where 39 mol% corresponds to the 30 vol% used in this study) and the total amount of Si measured from ICP-OES, as described in the results section of Chapter 6. Finally, each specimen was carbon coated with the Precision Etching and Coating System (PECS), then examined in the SEM and characterized with Energy Dispersive Spectroscopy (EDS, Princeton Gamma-Tech Inc., Princeton, NJ) to ensure complete removal of the borosilicate glass layer.

Example Calculation

Oxidation reaction:



Example calculation for: 1500° C, 100 minutes, trial 1

Molar mass for B₂O₃ = 69.622 g/mole

Molar mass for CO = 28 g/mole

Si to B ratio in starting borosilicate glass:

$$\frac{B}{Si} = \frac{0.61 \text{ mol} \times 2}{0.39 \text{ mol}} = 3.128 \quad [\text{A4.3}]$$

Total Si measured via ICP-OES:

$$2.97 \text{ mg/L} + 0.95 \text{ mg/L} + 86.05 \text{ mg/L} \cong 89.97 \text{ mg/L} \quad [\text{A4.4}]$$

$$(\text{H}_2\text{O soak 1} + \text{H}_2\text{O soak 2} + \text{HF soak} = \text{total Si})$$

Measured Si (mol):

$$89.97 \frac{\text{mg}}{\text{L}} * \frac{0.015 \text{ L}}{28.0855 \frac{\text{g}}{\text{mol}}} * \frac{1 \text{ g}}{1000 \text{ mg}} = 4.8 * 10^{-5} \text{ mol} \quad [\text{A4.5}]$$

Total B (mol) consumed during oxidation, predicted from [A4.3] and [A4.5]:

$$4.8 * 10^{-5} \text{ mol} * 3.128 = 1.5 * 10^{-4} \text{ mol} \quad [\text{A4.6}]$$

Total B measured via ICP-OES:

$$22.03 \text{ mg/L} + 3.91 \text{ mg/L} = 25.94 \frac{\text{mg}}{\text{L}} \quad [\text{A4.7}]$$

$$(\text{H}_2\text{O soak 1} + \text{H}_2\text{O soak 2} = \text{total B})$$

Measured B (mol):

$$25.94 \frac{mg}{L} * \frac{0.015L}{10.811 \frac{g}{mol}} * \frac{1g}{1000mg} = 3.6 * 10^{-5} mol \quad [A4.8]$$

Percentage of B retained ([A4.8]/[A4.6]):

$$\frac{3.6 * 10^{-5} mol}{1.5 * 10^{-4} mol} = 0.24 = 24\% \quad [A4.9]$$

Vaporized B (mol):

$$1.5 * 10^{-4} mol - 3.6 * 10^{-5} mol = 1.14 * 10^{-4} mol \quad [A4.10]$$

Total B₂O₃(g) and CO(g) vaporized:

$$\left(\frac{1.14 * 10^{-4} mol}{2} * \frac{69.622g}{mol} + 4.8 * 10^{-5} mol * \frac{28g}{mol} \right) * \frac{1000mg}{1g} = 5.312 mg \quad [A4.11]$$

Surface area of specimen:

$$(6.17mm * 3.99mm) * 2 + (6.17mm * 2.97mm) * 2 + (2.97mm * 3.99mm) * 2 \\ = 109.587mm^2 \quad [A4.12]$$

Measured mass after oxidation minus measured mass before oxidation:

$$384.95mg - 381.87mg = 3.08mg \quad [A4.13]$$

Total mass of generated oxides (ZrO₂+SiO₂+B₂O₃+CO) per area:

$$\frac{(3.08mg + 5.312mg)}{109.587mm^2} * 100 \frac{mm^2}{cm^2} = 7.669 mg/cm^2 \quad [A4.14]$$

Appendix 5: Collaborators

A number of collaborators assisted with the work in this thesis. They are listed in chronological order.

Dr. William Fahrenholtz and Eric Neuman (graduate, MS&T) – prepared ZrB₂-30 vol% SiC material

Brandon Patterson (undergraduate, UVA) – ran 1550°C box furnace oxidations and performed statistical analysis on same

David Lichtman (undergraduate, UVA) – assisted with sample preparation and statistical analysis

Forrest Craven (undergraduate, UVA) – ran trial 1 oxidation tests for ICP-OES

Suiying Lui (undergraduate, UVA) – ran trial 2 and 3 oxidation tests for ICP-OES and performed Casino simulations on EDS data for sampling volume

Bohuslava McFarland (graduate, UVA) – ran ICP-OES

Dr. Wayne Jennings (CWRU) – ran XPS and assisted in XPS data analysis

Annette Marsolais (CWRU) – assisted in running of ToF-SIMS and ToF-SIMS data analysis

Dr. David Marshall (Teledyne Scientific) – ion polished samples for ToF-SIMS

Dr. William Johnson (UVA) – assisted with diffusion coefficient and composition gradient calculations

Appendix 6: Publications

1. K. N. Shugart and E. Opila, “Initial Stages of ZrB₂-30 vol% SiC Oxidation”, Journal of the American Ceramic Society, DOI: 10.1111/jace.12843.
2. K. N. Shugart, B. Patterson, D. Lichtman, S. Liu, and E. Opila, “Mechanisms for Variability of ZrB₂-30 vol% SiC Oxidation Kinetics”, Journal of the American Ceramic Society, DOI: 10.1111/jace.12911.
3. K. N. Shugart, S. Liu, and E. Opila, “Determination of Retained Boria Content in ZrB₂-30 vol% SiC Oxide Scales”, in preparation for the Journal of the American Ceramic Society.
4. K. N. Shugart and E. Opila, “SiC-Depletion in ZrB₂-30 vol% SiC at Ultra-High Temperatures” , in preparation for the Journal of the American Ceramic Society.
5. K. N. Shugart and E. Opila, “Oxygen Diffusion Pathways in ZrB₂-30 vol% SiC at Ultra-High Temperatures” , in preparation for the Journal of the American Ceramic Society.

References

1. A. Paul, D.D. Jayaseelan, S. Venugopal, et al. "UHTC Composites for Hypersonic Applications," *J. Am. Ceram. Soc.*, **91**, 22-28 (2012).
2. D.M. Van Wie, D.G. Drewry Jr, D.E. King and C.M. Hudson. "The Hypersonic Environment: Required Operating Conditions and Design Challenges," *J. Mater. Sci.*, **39**, 5915-24 (2004).
3. R. Savino, M. De Stefano Fumo, D. Paterna and M. Serpico. "Aerothermodynamic Study of UHTC-Based Thermal Protection Systems," *Aerospace Science and Technology*, **9**, 151-60 (2005).
4. A. Chamberlain, W. Fahrenholtz, G. Hilmas and D. Ellerby. "Oxidation of ZrB_2 -SiC Ceramics Under Atmospheric and Reentry Conditions," *Refractories Applications Trans.*, **1**, 1-7 (2005).
5. P. Hu, X. Zhang, J. Han, X. Luo and S. Du. "Effect of Various Additives on the Oxidation Behavior of ZrB_2 -Based Ultra-High-Temperature Ceramics at 1800°C ," *J. Am. Ceram. Soc.*, **93**, 345-9 (2010).
6. X. Zhang, P. Hu, J. Han and S. Meng. "Ablation Behavior of ZrB_2 -SiC Ultra High Temperature Ceramics Under Simulated Atmospheric Re-entry Conditions," *Composites Sci. Technol.*, **68**, 1718-26 (2008).
7. J.D. Bull, D.J. Rasky and J.C. Karika. "Stability Characterization of Diboride Composites Under High Velocity Atmospheric Flight Conditions," *Advanced Materials: Meeting the Economic Challenge*; Toronto; Canada,
8. W.G. Fahrenholtz, G.E. Hilmas, I.G. Talmy and J.A. Zaykoski. "Refractory Diborides of Zirconium and Hafnium," *J. Am. Ceram. Soc.*, **90**, 1347-64 (2007).
9. L. Kaufman, E.V. Clougherty and J. Berkowitz-Mattuck. "Oxidation Characteristics of Hafnium and Zirconium Diboride," *Trans. Met. Soc. AIME*, **239**, 458-66 (1967).
10. E.V. Clougherty, R.L. Pober and L. Kaufman. "Synthesis of Oxidation Resistant Metal Diboride Composites," *Trans. Met. Soc. AIME*, **242**, 1077-82 (1968).
11. W.G. Fahrenholtz and G.E. Hilmas. "Oxidation of Ultra-High Temperature Transition Metal Diboride Ceramics," *Int. Mat. Rev.*, **57**, 61-72 (2012).
12. H.C. Graham, H.H. Davis, I.A. Kvernes and W.C. Tripp. "Microstructural Features of Oxide Scales Formed on Zirconium Diboride Materials," *Materials Science Research: Ceramics in Severe Environment*, **5**, 35-48 (1971).
13. W.G. Fahrenholtz, "Thermodynamic Analysis of ZrB_2 -SiC Oxidation: Formation of a SiC-Depleted Region," *J. Am. Ceram. Soc.*, **90**, 143-8 (2007).

14. M.M. Opeka, I.G. Talmy, E.J. Wuchina, J.A. Zaykoski and S.J. Causey. "Mechanical, Thermal, and Oxidation Properties of Refractory Hafnium and Zirconium Compounds," J. Eur. Ceram. Soc, **19**, 2405-14 (1999).
15. E. Opila and S. Levine. "Oxidation of ZrB₂- and HfB₂-Based Ultra-High Temperature Ceramics: Effect of Ta Additions," J. Mater. Sci., **39**, 5969-77 (2004).
16. P.A. Williams, R. Sakidja, J.H. Perepezko and P. Ritt. "Oxidation of ZrB₂-SiC Ultra-High Temperature Composites Over a Wide Range of SiC Content," J. Eur. Ceram. Soc, **32**, 3875-83 (2012).
17. I.G. Talmy, J.A. Zaykoski, M.M. Opeka and S. Dallek. "Oxidation of ZrB₂ Ceramics Modified with SiC and Group IV-VI Transition Metal Diborides," Elec. Soc. Proc., **12**, 144-58 (2001).
18. W.G. Fahrenholtz, G.E. Hilmas, A.L. Chamberlain and J.W. Zimmermann. "Processing and Characterization of ZrB₂-Based Ultra-High Temperature Monolithic and Fibrous Monolithic Ceramics," J. Mater. Sci., **39**, 5951-7 (2004).
19. W.C. Tripp, H.H. Davis and H.C. Graham. "Effect of an SiC Addition on the Oxidation of ZrB₂," Am. Ceram. Soc. Bull., **52**, 612-6 (1973).
20. E.J. Opila and M.C. Halbig. "Oxidation of ZrB₂-SiC," Ceram. Eng. Sci. Proc., **22**, 221-8 (2001).
21. A. Rezaie, W.G. Fahrenholtz and G.E. Hilmas. "Oxidation of Zirconium Diboride-Silicon Carbide at 1500°C at a Low Partial Pressure of Oxygen," J. Am. Ceram. Soc., **89**, 3240-5 (2006).
22. J. Li, T.J. Lenosky, C.J. Först and S. Yip. "Thermochemical and Mechanical Stabilities of the Oxide Scale of ZrB₂+SiC and Oxygen Transport Mechanisms," J. Am. Ceram. Soc., **91**, 1475-80 (2008).
23. X. Zhang, P. Hu and J. Han. "Structure Evolution of ZrB₂-SiC During the Oxidation in Air," J. Mater. Res., **23**, 1961-72 (2008).
24. S.R. Levine, E.J. Opila, M.C. Halbig, J.D. Kiser, M. Singh and J.A. Salem. "Evaluation of Ultra-High Temperature Ceramics for Aeropropulsion Use," J. Eur. Ceram. Soc, **22**, 2757-67 (2002).
25. A. Rezaie, W.G. Fahrenholtz and G.E. Hilmas. "Evolution of Structure During the Oxidation of Zirconium Diboride-Silicon Carbide in Air up to 1500 °C," J. Eur. Ceram. Soc, **27**, 2495-501 (2007).
26. T.A. Parthasarathy, R.A. Rapp, M. Opeka and M.K. Cinibulk. "Modeling Oxidation Kinetics of SiC-Containing Refractory Diborides," J. Am. Ceram. Soc., **95**, 338-49 (2012).

27. E. Eakins, D.D. Jayaseelan and W.E. Lee. "Toward Oxidation-Resistant ZrB₂-SiC Ultra High Temperature Ceramics," *Metall. Mat. Trans. A Phys. Metall. Mat. Sci.*, **42**, 878-87 (2011).
28. J. Han, P. Hu, X. Zhang and S. Meng. "Oxidation Behavior of Zirconium Diboride-Silicon Carbide at 1800°C", *Scr. Mater.*, **57**, 825-8 (2007).
29. M.M. Opeka, I.G. Talmy and J.A. Zaykoski. "Oxidation-Based Materials Selection for 2000°C + Hypersonic Aerosurfaces: Theoretical Considerations and Historical Experience," *J. Mater. Sci.*, **39**, 5887-904 (2004).
30. J. Schlichting, "Oxygen-Transport Through Glass Layers Formed by a Gel Process," *J. Non Cryst. Solids*, **63**, 173-81 (1984).
31. S.N. Karlsdottir and J.W. Halloran. "Rapid Oxidation Characterization of Ultra-High Temperature Ceramics," *J. Am. Ceram. Soc.*, **90**, 3233-8 (2007).
32. C.M. Carney, P. Mogilvesky and T.A. Parthasarathy. "Oxidation Behavior of Zirconium Diboride Silicon Carbide Produced by the Spark Plasma Sintering Method," *J. Am. Ceram. Soc.*, **92**, 2046-52 (2009).
33. J. Han, P. Hu, X. Zhang, S. Meng and W. Han. "Oxidation-Resistant ZrB₂-SiC Composites at 2200°C," *Composites Sci. Technol.*, **68**, 799-806 (2008).
34. T.A. Parthasarathy, R.A. Rapp, M. Opeka and R.J. Kerans. "A Model for the Oxidation of ZrB₂, HfB₂ and TiB₂," *Acta Mater.*, **55**, 5999-6010 (2007).
35. W. Han, P. Hu, X. Zhang, J. Han and S. Meng. "High-Temperature Oxidation at 1900°C of ZrB₂-xSiC Ultra High-Temperature Ceramic Composites", *J. Am. Ceram. Soc.*, **91**, 3328-34 (2008).
36. S. Gangireddy, S.N. Karlsdottir, S.J. Norton, J.C. Tucker and J.W. Halloran. "In Situ Microscopy Observation of Liquid Flow, Zirconia Growth, and CO Bubble Formation During High Temperature Oxidation of Zirconium Diboride–Silicon Carbide," *J. Eur. Ceram. Soc.*, **30**, 2365-74 (2010).
37. W. Yongjun, W. Zhenqing, L. Yang and L. Hongqing. "Mechanical Investigations on High Temperature Oxidation of ZrB₂-SiC UHTCs," 2008 2nd International Symposium on Systems and Control in Aerospace and Astronautics, ISSCAA 2008, (2008).
38. W.G. Fahrenholtz, "The ZrB₂ Volatility Diagram," *J. Am. Ceram. Soc.*, **88**, 3509-12 (2005).
39. K.N. Shugart, B. Patterson, D. Lichtman, S. Liu and E.J. Opila. "Mechanisms for Variability of ZrB₂-30 vol% SiC Oxidation Kinetics," submitted to *J. Am. Ceram. Soc.*,

40. B. Oberländer, P. Kofstad and I. Kvernes. "On Oxygen Diffusion in Tetragonal Zirconia," *Materialwissenschaft und Werkstofftechnik*, **19**, 190-3 (1988).
41. A.K. Kuriakose and J.L. Margrave. "The Oxidation Kinetics of Zirconium Diboride and Zirconium Carbide at High Temperatures," *J. Electrochem. Soc.*, **111**, 827-31 (1964).
42. F.H. Brown, "Stability of Titanium Diboride and Zirconium Diboride in Air, Oxygen, and Nitrogen," *California Inst. of Tech. , Pasadena Jet Propulsion Lab*, **No.JPL-PR-20-252**, (1955).
43. S.N. Karlsdottir and J.W. Halloran. "Formation of Oxide Films on ZrB₂-15 vol% SiC Composites During Oxidation: Evolution with Time and Temperature," *J. Am. Ceram. Soc.*, **92**, 1328-32 (2009).
44. S.N. Karlsdottir, J.W. Halloran and C.E. Henderson. "Convection Patterns in Liquid Oxide Films on ZrB₂-SiC Composites Oxidized at a High Temperature," *J. Am. Ceram. Soc.*, **90**, 2863-7 (2007).
45. S.N. Karlsdottir and J.W. Halloran. "Formation of Oxide Scales on Zirconium Diboride-Silicon Carbide Composites During Oxidation: Relation of Subscale Recession to Liquid Oxide Flow," *J. Am. Ceram. Soc.*, **91**, 3652-8 (2008).
46. K. Kawagishi, M. Susa, T. Maruyama and K. Nagata. "Boron Diffusion in Amorphous Silica Films," *J. Electrochem. Soc.*, **144**, 3270-3275 (1997).
47. D.M. Brown and P.R. Kennicott. "Glass Source B Diffusion in Si and SiO₂," *J. Electrochem. Soc.*, **118**, 293-300 (1971).
48. M.L. Barry and P. Olofsen. "Doped Oxides as Diffusion Sources," *J. Electrochem. Soc. Solid State Sci.*, **116**, 856-860 (1969).
49. S. Horiuchi and J. Yamaguchi. "Diffusion of Boron in Silicon through Oxide Layer," *Jpn. J. Appl. Phys.*, **1**, 314-323 (1962).
50. M.A. Lamkin, F.L. Riley and R.J. Fordham. "Oxygen Mobility in Silicon Dioxide and Silicate Glasses: a Review," *Journal of the European Ceramic Society*, **10**, 347-67 (1992).
51. J. Jedlinski, "Comments on the Use of the Two-Stage-Oxidation Method and Surface-Analytical Techniques in Studying Growth Processes of Oxide Scales," *Oxidation of Metals (USA)*, **39**, 61-8 (1993).
52. J.D. Cawley and R.S. Boyce. "A Solution of the Diffusion Equation for Double Oxidation in Dry Oxygen Including Lazy Exchange Between Network and Interstitial Oxygen," *Phil. Mag. A*, **58**, 589-601 (1988).
53. B.A. Pint, J.R. Martin and L.W. Hobbs. "¹⁸O/SIMS characterization of the growth mechanism of doped and undoped *a*-Al₂O₃," *Oxidation Metals*, **39**, 167-95 (1993).

54. N. Appannagaari and S.N. Basu. "Modeling of O-18 Tracer Distribution During Double Oxidation Experiments For Inward Growing Scales," J. Appl. Phys., **78**, 2060-9 (1995).
55. B.E. Deal and A.S. Grove. "General Relationship for the Thermal Oxidation of Silicon," J. Appl. Phys., **36**, 3770-8 (1965).
56. L.U.J.T. Ogbuji and E.J. Opila. "Comparison of the Oxidation Kinetics of SiC and Si₃N₄," J. Electrochem. Soc., **142**, 925-30 (1995).
57. J.D. Cawley, J.W. Halloran and A.R. Cooper. "Oxygen-18 Tracer Study of the Passive Thermal Oxidation of Silicon," Oxidation Metals, **28**, 1-16 (1987).
58. J.A. Costello and R.E. Tressler. "Isotope Labeling Studies of the Oxidation of Silicon at 1000°C and 1300°C," J. Electrochem. Soc. Solid State Sci., **131**, 1944-1947 (1984).
59. Z. Zheng, R.E. Tressler and K.E. Spear. "Oxidation of single-crystal silicon carbide: I, Experimental studies," J. Electrochem. Soc., **137**, 854-8 (1990).
60. Z. Zheng, R.E. Tressler and K.E. Spear. "Oxidation of single-crystal silicon carbide. Part II. Kinetic model," J. Electrochem. Soc., **137**, 2812-6 (1990).
61. J.D. Kalen, R.S. Boyce and J.D. Cawley. "Oxygen Tracer Diffusion in Vitreous Silica," J Am Ceram Soc, **74**, 203-9 (1991).
62. U. Brossmann, R. Wurschum, U. Sodervall and H. Schaefer. "Oxygen Diffusion in Ultrafine Grained Monoclinic ZrO₂," J. Appl. Phys., **85**, 7646-54 (1999).
63. U. Brossmann, U. Sodervall, R. Wurschum and H.-. Schaefer. "¹⁸O Diffusion in Nanocrystalline ZrO₂," NanoStructured Materials, **12**, 871-874 (1999).
64. G. Bakradze, L. Jeurgens, T. Acartuerk, U. Starke and E.J. Mittemeijer. "Atomic transport mechanisms in thin oxide films grown on zirconium by thermal oxidation, as-derived from 18O-tracer experiments," Acta Mater., **59**, 7498-507 (2011).
65. C.J. Geankoplis, *Mass Transport Phenomena*; Ohio State Univ Bookstore, Ohio, 1984.
66. A.L. Chamberlain, W.G. Fahrenholtz, G.E. Hilmas and D.T. Ellerby. "High-Strength Zirconium Diboride-Based Ceramics," J. Am. Ceram. Soc., **87**, 1170-2 (2004).
67. F. Monteverde, S. Guicciardi and A. Bellosi. "Advances in Microstructure and Mechanical Properties of Zirconium Diboride Based Ceramics," Mat. Sci. and Engin. A, **346**, 310-9 (2003).
68. D.A. Shirley, "High-Resolution X-Ray Photoemission Spectrum of the Valence Bands of Gold," Phys. Rev. B, **5**, 4709-4714 (1972).

69. C.J. Powell and J.M. Conny. "Evaluation of Uncertainties in X-ray Photoelectron Spectroscopy Intensities Associated with Different Methods and Procedures for Background Subtraction. I. Spectra for Monochromatic Al X-ray," *Surf. Interface Anal.*, **41**, 269-94 (2009).
70. V.R. Bruckner, Wurzburg and J.F. Navarro. "Physikalisch-chemische Untersuchungen im System B_2O_3 - SiO_2 ," *Glastechn. Ber.*, **39**, 283-93 (1966).
71. C.W. Bale, P. Chartrand, S.A. Degterov, et al. "FactSage Thermochemical Software and Databases," *Calphad*, **26**, 189,189-228 (2002).
72. B. Pieraggi, "Calculations of Parabolic Reaction Rate Constants," *Oxi. Met.*, **27**, 177-85 (1987).
73. J.F. Moulder, W.F. Stickle, P.E. Sobol and K.D. Bomben. *Handbook of X-ray Photoelectron Spectroscopy*; Perkin-Elmer Corporation, Eden Prairie, Minnesota, 1992.
74. National Institute of Standards and Technology, Gaithersburg, "NIST X-ray Photoelectron Spectroscopy Database, Version 4.1,"
75. C.E. Ramberg, G. Cruciani, K.E. Spear, R.E. Tressler and C.F. Ramberg. "Passive-Oxidation Kinetics of High-Purity Silicon Carbide from 800° to 1100°C," *J. Am. Ceram. Soc.*, **79**, 2897-911 (1996).
76. S.N. Karlsdottir, J.W. Halloran and A.N. Grundy. "Zirconia Transport by Liquid Convection During Oxidation of Zirconium Diboride-Silicon Carbide," *J. Am. Ceram. Soc.*, **91**, 272-7 (2008).
77. L. Kaufman, "Personal Communication with E. Opila," (28 January 2008).
78. E.J. Opila, "Oxidation Kinetics of Chemically Vapor-Deposited Silicon Carbide in Wet Oxygen," *J. Am. Ceram. Soc.*, **77**, 730-736 (1994).
79. E.J. Opila, "Variation of the Oxidation Rate of Silicon Carbide with Water-Vapor Pressure," *J. Am. Ceram. Soc.*, **82**, 625-636 (1999).
80. Q.N. Nguyen, E.J. Opila and R.C. Robinson. "Oxidation of Ultrahigh Temperature Ceramics in Water Vapor," *J. Electrochem. Soc.*, **151**, B558-62 (2004).
81. E.J. Opila, N.S. Jacobson, D.L. Myers and E.H. Copland. "Predicting Oxide Stability in High-Temperature Water Vapor," *J. O. M.*, **58**, 22-8 (2006).
82. B. Roebuck, G. Edwards and M.G. Gee. "Characterisation of Oxidising Metal Surfaces with a Two Colour Pyrometer," *Mat. Sci. and Tech.*, **21**, 831-40 (2005).
83. T. Beck and K. Rau. "Temperature Measurement and Control Methods in TMF Testing- a Comparison and Evaluation," *Int. J. Fatigue*, **30**, 226-33 (2008).

84. D.D. Jayaseelan, E. Zapata-Solvas, P. Brown and W.E. Lee. "In situ Formation of Oxidation Resistant Refractory Coatings on SiC-Reinforced ZrB₂ Ultra High Temperature Ceramics," J Am Ceram Soc, **95**, 1247-54 (2012).
85. R.F. Cooper and K. Chyung. "Structure and Chemistry of Fibre-Matrix Interfaces in Silicon Carbide Fibre-Reinforced Glass-Ceramic Composites: an Electron Microscopy Study," J. Mat. Sci., **22**, 3148-3160 (1987).
86. L.A. Bonney and R.F. Cooper. "Reaction-Layer Interfaces in SiC-Fibre-Reinforced Glass-Ceramics: A High-Resolution Scanning Transmission Electron Microscopy Analysis," J. Am. Ceram. Soc., **73**, 2916-2921 (1990).
87. B.W. Sheldon, E.Y. Sun, S.R. Nutt and J.J. Brennan. "Oxidation of BN-Coated SiC Fibers in Ceramic Matrix Composites," J. Am. Ceram. Soc., **79**, 539-543 (1996).
88. H. Katsui, M. Oguma and T. Goto. "Carbon Interlayer Between CVD SiC and SiO₂ in High-Temperature Passive Oxidation," J. Am. Ceram. Soc., (2014).
89. H.J.T. Ellingham, "Reducibility of Oxides and Sulphides in Metallurgical Processes," J. Soc. Chem. Ind., **63**, 125-133 (1944).
90. G.R. Holcomb and G.R. St. Pierre. "Application of a Counter-Current Gaseous Diffusion Model to the Oxidation of Hafnium Carbide at 1200 to 1530°C," Oxi. Met., **40**, 109-118 (1993).
91. J. Crank, *The Mathematics of Diffusion*; pp. 1-414. Oxford University Press, New York, 1975.
92. G.D. Bagratishvili, R.B. Dzhanelidze, D.A. Jishiashvili, L.V. Piskanovskii and Z.N. Shiolashvili. "Boron diffusion from a reactively sputtered glass source in Si and SiO₂," physica status solidi (a), **56**, 27-35 (1979).
93. P.B. Adams and D.L. Evans. "Chemical Durability of Borate Glasses," Mat. Sci. Research, **12**, 525-37 (1978).
94. T.J. Rockett and W.R. Foster. "Phase Relations in System Boron Oxide-Silica," J. Am. Ceram. Soc., **48**, 75-80 (1965).
95. T.A. Parthasarathy, R.A. Rapp, M. Opeka and R.J. Kerans. "Effects of Phase Change and Oxygen Permeability in Oxide Scales on Oxidation Kinetics of ZrB₂ and HfB₂," J. Am. Ceram. Soc., **92**, 1079-1086 (2009).
96. S.C. Zhang, W.G. Fahrenholtz and G.E. Hilmas. "Oxidation of ZrB₂ and ZrB₂-SiC Ceramics with Tungsten Additions," ECS. Trans., **16**, 137-145 (2009).